Measurements and modeling of cross-shore morphodynamics

J.P.C. Eekhout

September 30, 2008

Contents

Voorwoord

Tijdens de dramatische eerste seizoenshelft van NEC van vorig seizoen zei Mario Been, de trainer van NEC, meerdere malen:

'Alles komt goed!'

Dat is misschien ook wel van toepassing op mijn studieperiode. Na een valse start bij de studie Toegepaste Wiskunde heb ik na een half jaar besloten om Civiele Techniek te gaan studeren. Na een moeizaam begin heb ik dan toch echt (als het goed is...) mijn studie afgerond. Zo komt alles toch weer goed! Ik wil van de gelegenheid gebruik maken om een aantal mensen te bedanken.

Allereerst wil ik graag mijn dagelijkse begeleider Jolanthe bedanken voor alle moeite die ze in mijn afstudeerproject heeft gestoken. Het begon allemaal in Hannover waar we 5 weken samen de experimenten hebben uitgevoerd. Ik heb daar veel geleerd over het uitvoeren van grootschalige experimenten en wat er vooral allemaal fout kan gaan. Daarbij wil ik ook graag iedereen bedanken die tijdens die periode heeft meegeholpen aan de experimenten. Dat zijn Michel, Dominic, Lorna en Luca. Ook na afloop van de experimenten heeft Jolanthe me goed geholpen met de verdere afwikkeling van mijn afstudeeronderzoek.

Daarnaast wil ook graag de rest van mijn afstudeercommissie bedanken voor jullie bijdrage aan mijn afstudeeronderzoek. Bij de verwerking van de data heb ik veel hulp gehad van Jan, waar bij het model juist Gerben mij veel heeft geholpen. Omdat Jebbe in de tussentijd ook veel met Unibest-TC heeft gewerkt en daarnaast ook ervaring heeft met data verwerking, heeft Jebbe me op beide vlakken veel nuttige tips kunnen geven.

Ook wil graag iedereen die de afgelopen maanden in de afstudeerkamer heeft gezeten bedanken voor de gezelligheid, het op en neer lopen naar de koffie-automaat, het lunchen, het eten bij restaurant Roma (goeie pizza's hebben ze daar), enz. Dus Wout (ben ik toch 2 weken eerder klaar, ghehe), Bouke, Renske, Irene, Bregt, Robert, Pieter, Marcel, Sander en Bart, bedankt!

Pieter en Pieter, ik wil graag op de ouwehoermailingslist blijven staan om nog lekker over voetbal en andere onzinnige dingen te kunnen blijven ouwerhoeren. De rest van de vakgroep die me geholpen heeft bij al mijn LaTeXproblemen (kan ik dat ook een keer gebruiken...). Iedereen die lekker aan de koffietafel heeft gezeten op de afstudeerkamer. En natuurlijk alle voetballers van WNVNB.

Als laatste wil ik mijn ouders en m'n broer bedanken voor hun steun. En van m'n ouders natuurlijk de financiële steun.

Enschede, 29 september 2008.

Summary

A lot of processes within process-based models, like Unibest-TC, are still not well understood. Consequently, numerous experiments are carried out to get more insight in these processes. As part of the European HYDRALAB-III project, experiments were carried out in the Große Wellenkanal (GWK) of the *ForschungsZentrum Küste* in Hannover, Germany. Data was obtained from wave heights, flow velocities, sediment concentrations and bed level measurements.

Ruessink et al. (2007) stated that the calibration procedure of Unibest-TC focuses on net sediment transport rates only and free model parameters may compensate for missing or incompletely described processes. Therefore, they suggest to collect concentration and velocity profiles under a wide range of natural conditions, and use these data to validate the temporal and spatial variability of the bedload and suspended sediment transport formulations predicted by the present formulations.

This resulted in the following research objective:

> *The validation of the cross-shore profile model Unibest-TC using data collected in a full-scale wave flume. The model is validated step-by-step using wave height, velocity, sediment concentration and bed level data.*

Experimental data

Experiments were performed in the Große Wellenkanal (GWK) in Hannover, Germany. Under full scale wave conditions data was obtained from several instruments. A measurement frame was located at +111 m from the wave paddle. At this non-breaker location, velocity and sediment concentration data were obtained. Velocity measurement were performed using 4 EMF-probes and a Vecrino. The sediment concentration was measured with suction tubes (TSS). Over the whole length of the flume, wave height (wave gauges) and bed level measurements (bed level profiler) were performed. From a extensive data set, four conditions were selected, where one condition is used for model calibration purposes and the other three to validate Unibest-TC. The conditions varied in design wave height between, viz. 0.7, 1.2 and 1.5 m. All conditions consisted of regular wave experiments.

The wave height data showed that between wave gauge 1 and 17 (+50–180 m from wave paddle) there was no or little change in wave height. Shoaling occurred at wave gauge 18 (at +216 m from wave paddle) in three of four conditions. Wave breaking occurred between wave gauge 18 and 19 in all four conditions. The wave height data showed inconsistency between successive wave gauges. Differences between neighboring wave gauges up to 25 cm were found. No clear evidence was found for these differences.

The flow velocity at 5 different heights above the bed was measured with 4 EMF-probes and a Vectrino. Per instrument, the time-averaged velocity was determined, combined to a velocity profile. The mean current profiles showed that with increasing wave height, the time-averaged velocity becomes more offshore directed. This is in agreement with the depth-averaged velocity, based on linear wave theory. The EMF on the measurement frame deviated from this observation, even when correcting for an offset of approximately 1-2 cm/s. The data from this instrument is not taken into account in the remainder of the study.

Besides the time-averaged velocity, the Vectrino was used to measure the time-dependent flow velocity at approximately 10 cm above the bed. The ensemble-averaged signal over 50 waves gave a reasonable smooth signal. Flow velocity characteristics show that with increasing wave height the orbital flow velocity R also increases. And with increasing wave height, an increase of the wave mobility number Ψ_{max} was found, corresponding with existing regime limits (O'Donoghue et al., 2006).

The sediment concentration measurements show that the mean concentration profile of condition H07 is best compared with the exponential expression derived by (Bosman and Steetzel, 1986), which was modeled after measurements in rippled-bed conditions. Remarked that no measurements were performed close to the bed (< 9 cm above bed). Condition H12 and H15 show best comparison with the power law based expression according to (Smith, 1977). Consistent with (Dohmen-Janssen and Hanes, 2002), a variable concentration decay parameter α was found.

Net sediment transport rates were calculated from the bed level measurements obtained by the bed profiler, where the bed level was measured in the middle of the flume. The net sediment transport rates are not very reliable. This method is only suitable for a solely 2D situation. However, in the wave flume also 3D bed forms were found. This caused uncertainty in two regions of the flume, around +50 m and +150 m from the wave paddle. The measured net transport rates at +111 m from the wave paddle were compared with the third-order velocity moment, derived from the Vectrino measurements. A linear relationship was found, consistent with Dohmen-Janssen and Hanes (2002).

Unibest-TC

Unibest-TC is not suitable for solely regular wave conditions. Therefore, some adjustments have been made to the model formulations to account for some differences between irregular and regular wave conditions. In the case of irregular waves, the fraction of breaking waves is more than 0 over almost the entire profile. From observations it appeared that during the experiments waves were breaking at approximately the same cross-shore position during every condition. The breaker criterium is changed to account for regular waves. The formulation of the thickness of the wave boundary layer consists of a multiplication factor f_δ set to a value of 20, which corresponds to measurements from irregular wave conditions. For regular wave conditions a value of 1 is more suitable. An extra keyword is added to Unibest-TC to alter the value of this factor. The near-bed orbital velocity is modeled with a velocity field of 7 waves. In the original model formulations, the near-bed orbital velocity signal was the sum of two regular wave fields, which causes to be irregular afterwards. Only one regular velocity signal is used in the adjusted model to account for regular waves.

One condition was used to calibrate Unibest-TC. The condition consisted of a design wave height of 1.5 m. Unibest-TC was calibrated on the wave propagation module, the mean current profile module, the mean concentration module and the total sediment transport module. The wave propagation in the lower shoreface is calibrated using the friction factor f_w from the formulation of the dissipation due to bottom friction. A value of 0.010 gave the best comparison with the measured wave height. In the upper shoreface, the wave height is calibrated using two dissipation coefficients. The best results were found with $\gamma = 0.8$ and $\alpha = 1.2$. The mean current profile was calibrated using the roughness height k_s. This term was set to its maximum value (0.2). For better results, the multiplication factor f_δ was set to a value smaller than 1. From the literature a value between 1 and 20 is recommended (see (Walstra, 2000)). However, the corresponding thickness of the wave boundary layer agrees with values found in the literature. The grain size of the suspended sediment was set equal to the median grain size, this gives the best slope of the mean concentration profile. The maximum value of the current- and wave-related roughness, $k_{s,c}$ and $k_{s,w}$ respectively, was used to calibrate the concentration profile. The best results were obtained with a value of 0.015. The internal friction angle $\tan \phi$ was set to 0.3, in correspondence with earlier studies (Walstra, 2000).

The validation showed that all hydrodynamic modules show good comparison between Unibest-

TC and the experimental data, i.e. the wave propagation module, the mean current profile module and the near-bed orbital velocity module. The wave propagation on the lower shoreface shows good agreement with the measured wave height. The same applies for wave shoaling and wave breaking, although there were only two wave gauges situated in this region during the experiments. The mean current profile agrees well with the data for all three conditions. Although, all conditions show a little overestimation of the mean current for all measurement heights. All flow velocity characteristics from the near-bed orbital velocity show comparable results compared to the measured time-dependent velocities. The third-order velocity moment $\langle U^3 \rangle$ is overestimated by Unibest-TC. The model does not take acceleration skewness into account, this results in $\beta = 0.5$ (degree of acceleration skewness) for all conditions.

The mean concentration profile does not agree well with the data, this applies for all conditions. The reference concentration is underestimated for condition H07 and H12 and overestimated for condition H15. The concentration decay length from the mean concentration profile shows good agreement with the measurements. Although the measured net transport rates are not very reliable, the net sediment transport rates are still compared with the modeled transport rates from Unibest-TC. Condition H07 shows the best results, both on the lower and the upper shoreface. The other two conditions show high transport rates at the nearshore bar. These high transport rates result from high values of the current-related suspended sediment transport.

Some suggestions have been made for model improvement. In the mean concentration profile formulations a new expression for a variable diameter of the suspended sediment is proposed, according to Van Rijn (2007). A phase function for the wave-related suspended sediment transport is suggested, also according to Van Rijn (2007). And a suggestion is made for a different formulation of the peak near-bed orbital velocity in the current-related suspended sediment transport module. It is recommended to test these improvements with existing data sets which are already in the Unibest-TC testbank.

Chapter 1

Introduction

1.1 Context

To most people, the principle landform of wave-dominated coasts is the beach. However, the beach is just one component of wave-dominated coasts. The shoreface, which is the underwater slope that lies seaward of the beach, is also dominated by wave-processes. Additionally, the coastal dunes behind beaches can also be considered as an element of wave-dominated coastal environments. The coastal dune, beach and shoreface are strongly linked by sediment transport pathways and morphodynamic feedbacks. Collectively, they make up coastal barriers and can be considered the basic elements of wave-dominated coasts (Roy et al., 1994).

Coastal zones generally are densely-populated areas. Besides that, a lot of important economic activities are also situated in these regions. The safety of the inhabitants against inundation has to be ensured and economic activities in the coastal zone has to be maintained. Therefore, it is of great importance to understand the morphological behaviour of the coastal zone to predict future changes. For these purposes morphodynamic models have been developed, Unibest-TC is an example of such a model. These models describe the morphological behaviour using a morphodynamic loop, see Figure 1.1.
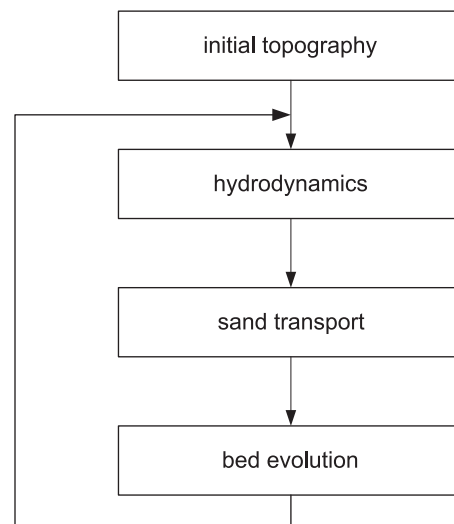

Figure 1.1: The morphodynamic loop.

The morphodynamic loop starts with an initial topography, which consists of the upper and the lower shoreface. In the upper shoreface nearshore bars can be found. Nearshore bars are highly

dynamic and tend to move in response to changing wave conditions. Besides nearshore bars, bed forms of smaller scale are found over the whole length of the shoreface. With hardly any wave action, the bed could be considered flat. In calm wave conditions ripples are formed, the so-called ripple-regime. With increasing wave heights, and consequently increasing flow velocities, the bed becomes flat again, which is denoted by the sheet-flow regime.

The second step in the morphodynamic loop are the hydrodynamics, which starts with wave propagation. When waves approach the shore an increase of wave height is observed close to the shore. This increase in wave height is known as wave shoaling and is particularly pronounced just before wave breaking at the seaward edge of the surf zone. Close to the shore, waves also tend to become more asymmetric in shape. As the waves enter intermediate water, they become increasingly asymmetrical and develop peaked crests and flat troughs, denoted by velocity skewness. With decreasing water depths, the waves transform into pitched-forward sawtooth profiles, indicated by acceleration skewness. At some point during shoaling, the water depth becomes too shallow for a stable wave form to exist and the wave will break. Breaking waves in the surf zone results in a seaward return flow, the undertow, which consists of a bottom current flowing in the seaward direction and is fed by the water carried toward the shore by the breakers and bores. The undertow is not only present near the point of breaking, but also further offshore in the lower shoreface region. Within a few centimeters from the bed, the flow could either be positive or negative due to near bottom streaming.

Waves produce bed shear stress which drives sediment transport, the third step in the morphodynamic loop. If the bed shear stress exceeds a threshold value, the grains will be lifted from the bed and carried by the flow. Sediment is transported either in suspension (suspended sediment transport) or close to the bed (bedload transport). Suspended sediment transport is subdivided into current-related and wave-related suspended sediment transport. The current-related suspended sediment transport results from the integration of the sum of the time-averaged current vertical and the sediment concentration vertical. Due to the seaward directed undertow, the current-related suspended sediment transport is also seaward directed. Wave-related suspended sediment transport derives from the instantaneous response of the suspended sediment concentration to the near-bed orbital velocity. Bedload transport is the transport of sediment close to the bed. Especially in the sheet-flow regime, the bedload transport contributes for a large part to the total sediment transport. The sum of both suspended and bedload transport results in the total sediment transport, which determines where sedimentation or erosion will take place, which is the final step in the morphodynamic loop.

1.2   Research objective

A lot of processes within process-based models, like Unibest-TC, are still not well understood. Consequently, numerous experiments are carried out to get more insight in these processes. As part of the European HYDRALAB-III project, experiments were carried out in the Große WellenkKanal (GWK) of the *ForschungsZentrum Küste* in Hannover, Germany. Data was obtained from wave heights, flow velocities, sediment concentrations and bed level measurements.

Ruessink et al. (2007) stated that the calibration procedure of Unibest-TC focuses on net sediment transport rates only and free model parameters may compensate for missing or incompletely described processes. Therefore, they suggest to collect concentration and velocity profiles under a wide range of natural conditions, and use these data to validate the temporal and spatial variability of the bedload and suspended sediment transport formulations predicted by the present formulations.

This results in the following research objective:

> *The validation of the cross-shore profile model Unibest-TC using data collected in a full-scale wave flume. The model is validated step-by-step using wave height, velocity, sediment concentration and bed level data.*

The validation of Unibest-TC will take place on two spatial scales. Over the whole length of the flume wave height and bed level data is obtained. These data are used to validate the model over the whole length of the bed profile. Locally, at a measurement location under non-breaking conditions, data is obtained from flow velocity and sediment concentration measurements on several heights above the bed. These data are used to validate time-averaged velocity and concentration verticals and time-dependent flow velocity close to the bed.

1.3 Research questions and outline of the thesis

In the following, four research questions are introduced along with the outline of the thesis.

Question 1.

What are the findings of the GWK-experiments and what specific aspects of the data are required to validate Unibest-TC?

First, Chapter 2 provides a description of the experimental facility, research conditions and used instruments. The second part of this chapter focuses on the results from the experiments. The data is subdivided into wave propagation, mean velocity profile, near-bed orbital velocity, mean concentration profile, total sediment transport and morphological changes. These six subjects return in Chapter 5. The description of the data focuses on the comparison with Unibest-TC. Specific characteristics will be extracted from the data to get a proper comparison with Unibest-TC. Some well-known theories are used to get more understanding of the data.

Question 2.

What are the main characteristics of Unibest-TC and what changes have to be made to the model formulations to deal with regular waves?

Since the model is used for solely irregular wave conditions some changes have to be made to the model formulations to deal with the regular wave conditions from the GWK-experiments. These changes are described in full detail in Chapter 3. The focus is also on the free model parameters. A description is provided of how the free model parameters influence the model formulations. At the end of Chapter 3, the initial conditions are listed, like grid size, numerical time step, grain size diameter, initial wave height and still water level.

Question 3.

What parameter settings are required to validate Unibest-TC?

Before the model is validated, Chapter 4 will describe the calibration of Unibest-TC. One of the four conditions is used for model calibration purposes. The wave propagation module, mean current profile module, mean concentration module and sediment transport module of Unibest-TC include free model parameters. The processed data is used to find values for these parameters for best data comparison. The procedure will be as follows. First the wave propagation module is calibrated over the whole length of the profile. Secondly, the mean current and concentration profiles are calibrated locally using the wave height at the measurement location as input for these two modules. And finally, the sediment transport is calibrated, also over the whole length of the profile. During the whole calibration procedure, the parameter settings from previous steps are maintained till the end of the calibration. So, after calibration of the wave propagation module, the obtained parameter values will not be change anymore during the rest of the calibration. The parameter settings are discussed on the values found in earlier calibration studies of Unibest-TC.

Question 4a.

What is the behaviour of Unibest-TC compared to the data?

Question 4b.

What are the strengths and weaknesses of Unibest-TC?

Three conditions are used to validate Unibest-TC. The obtained parameter settings are used to run the model, using different initial wave heights and initial bed profiles. All other settings are kept to the values obtained from Chapter 4. The comparison between the data and Unibest-TC will focus on the nature of the differences between the two. The analysis will focus on the model formulations and the roll of the free model parameters.

In the final chapter the answers to these research questions are presented. Besides that, Chapter 6 also contains the discussion and recommendations for further research.

Chapter 2

Experimental data

2.1 Experimental set-up

2.1.1 Experimental facility

The experiments were performed in the Large Wave Flume (Große Wellenkanal, GWK; Hannover, Germany), one of the largest wave flumes in the world. It is a joint research facility for coastal engineering studies of the University of Hannover and the Technical University of Braunschweig. It was constructed by the *Deuthsche Forschungsgemeinschaft* (German Research Association) and was inaugurated in 1983. Since 1997, the wave flume has been part of the *ForschungsZentrum Küste* (Coastal Research Center). The flume has a length of 307 m, a width of 5 m and a depth of 7 m. The flume has a horizontal concrete bottom and at the far end of the flume a permanent 1:6 asphalt slope is constructed over which the sediment was placed.

The installed power of the piston type wave generator combined with an upper flap is about 900 kW. The gearwheel driven carrier gives a maximum stroke of $\pm$ 2.10 m to the wave paddle. The stroke can be superimposed by upper flap movements of $\pm$ 10 degree in order to simulate natural water wave kinematics most accurately. The wave paddle allows for the realization of prototype experiments, with wave spectra or regular waves with periods between 1 and 15 s and heights up to 2.5 m, without superimposed currents. Wave reflections from installed structures or a beach in the flume are compensated by a digital computer-based online control system.

Figure 2.1: Impression of the Large Wave Flume.

2.1.2   Research conditions

Geometry

The initial bed profile consisted of a 1:20 beach slope at the end of the flume, followed by a 1 meter thick horizontal sand bed (Figure 2.2). The still water level was 4.5 m above the horizontal flume bottom. The bed consisted of quartz sand with the following characteristics: $D_{10} = 95$ μm, $D_{50} = 226$ μm and $D_{90} = 469$ μm (see Figure 2.3). It should be remarked that the water contained a large portion of silt particles.

Figure 2.2: Schematization of the wave flume.

Figure 2.3: Grain size distribution.

Test conditions

The initial aim of the experiments was to measure detailed flow velocities and sediment concentration close to the bed under non-breaking sheet-flow conditions. Afterwards, some experiments were performed in the ripple-regime as well. A measurement frame was positioned at +111 m from the wave paddle (the vertical dashed line in Figure 2.2), where no wave breaking occurred and a flat bed could be maintained during a large part of the experiments.

During the entire measurement period both regular waves and wave spectra (JONSWAP) were generated. Data were collected for 18 different conditions, with wave heights from 0.7 to 1.5 m and wave periods from 4.0 to 9.1 s. For the present study, the data needs some specific demands. These demands are listed below:

- a time-dependent flow velocity signal at approximately 10 cm above the bed for near-bed orbital velocity comparison

- time-averaged sediment concentration measurements at at least 8 heights above the bed

- at least 2 hours of experiments, where each experiment exists of at least 2 individual runs

Unfortunately, the JONSWAP tests did not meet these demands. Only regular wave tests are used in this study. Four conditions were selected, based on the availability of data and observed morphological changes. The test conditions are presented in Table 2.1. The table includes the date of the experiments, the designed wave height at the wave paddle H, the wave period T, the number of tests per condition and the duration of the experiment. The main difference between the four conditions is the designed wave height, where H07 is in the ripple regime, H12 in the intermediate regime and both H15 conditions are in the sheet-flow regime. Consequently, Unibest-TC is validated for several transport regimes. One condition is chosen for calibration purposes. Since there are 2 tests with a designed wave height of 1.5 m, one is selected to calibrate Unibest-TC.

Table 2.1: Overview of the test conditions.

Test condition	date	H [m]	T [s]	no. tests	duration [hr]
H07	18-7-'07	0.7	6.5	2	4
H12	5/6-7-'07	1.2	6.5	4	2
H15	2/3-7-'07	1.5	6.5	2	2
H15 (calibration)	16-7-'07	1.5	6.5	4	2

2.1.3 Instruments

Several instruments were used during the experiments. Instruments were attached to a measurement frame and mounted to the flume wall. A measurement tank was buried under the sand bed. Bed profile measurements were done using a movable carriage. The characteristics of all instruments are described here. The most important characteristics of all instruments are listed in Table 2.2.

Instruments on measurement frame

The measurement frame was situated at +111 m from the wave paddle, above the horizontal bed, far away from the nearshore bar. The frame consisted of two parts, the main-frame (attached to the flume wall) and a sub-frame, which could be vertically adjusted during the experiments. The measurement frame is shown in Figure 2.4(a).

Instruments on the main-frame The instruments on the main-frame include an Acoustic Backscatter (ABS), a ripple profiler, a pressure sensor and an electromagnetic flowmeter (EMF) (see Figure 2.4(a)). A description of the EMF and the ripple profiler is provided here.

EMF (frame) An S-type EMF probe, developed by WL | Delft Hydraulics, was mounted on the main-frame (see Figure 2.4(a)). The EMF, electromagnetic flowmeter, is used to measure flow velocities simultaneously in two perpendicularly oriented directions, only the horizontal component, in cross-shore direction, is used in this study. Time-averaged data from the EMF is used to validate the mean velocity profile.

The measuring technique is based on the principle that any moving conductor, in this case water, in a magnetic field induces a voltage across the conductor. The active element in an EMF consists of an electric coil with electrodes surrounding it. When the coil is energized, a magnetic

Table 2.2: Instrument characteristics.

Instrument	measured variable	x-pos [m]	z-pos [m from initial bed level]	accuracy	range	sample rate [Hz]
EMF (frame)	flow velocity (mean velocity profile)	111	1.14	± 10 mm/s ±3% of measured value[1]	±5 m/s[1]	50
Vectrino	flow velocity (mean velocity profile & near-bed orbital velocity)	111	0.07 − 0.15	±1 mm/s ±0.5 % of measured value[2]	±2.5 m/s[2]	200
TSS	sediment concentration (mean concentration profile)	111	0.02 − 0.45	±0.1 g/l[3]	n/a	n/a
Wave gauges	water elevation (wave propagation)	see Table 2.3	n/a	± 10 mm[3]	2.2 − 7.0 m	40
EMF (flume wall)	flow velocity (mean velocity profile)	106.4	0.70, 1.80, 2.50	± 50 mm/s ±3% of measured value	±5 m/s	40
CCM	bed level	111	-0.05 − 0.05	±1 mm[1]	0 − 0.28 m	50
Bed profiler	bed level (total sediment transport)	55 − 273	0 − 7	horizontal: ±250 mm vertical: ±50 mm[4]	0 − 6 m	n/a
Ripple profiler	bed level	111	0.80	vertical: ±5 mm[5]	± 1 m	every 5 minutes

[1] http://www.wldelft.nl, [2] Nortek (2004), [3] Dette et al. (2002), [4] Dursthoff et al. (1997), [5] Bell et al. (1998)

(a) Measurement frame

(b) EMF (flume wall) & wave gauge

(c) Subframe

(d) Bed level profiler

Figure 2.4: Photography

field is produced through the surrounding water. The electrodes receive the detailed electrical voltage, which is proportional to the velocity.

The raw EMF-data, in volts, is calibrated to the flow velocity in m/s. The following calibration formula is used:

$$u[\text{m/s}] = \frac{u[\text{V}] + 0.0013403}{1.1442} \tag{2.1}$$

Ripple Profiler   Measurements of the bed morphology over time were made with a Sand Ripple Profiler Sonar (SRPS) (see Figure 2.4(a)). The ripple profiler was capable of measuring a two dimensional profile with a length of approximately 2 m in cross-shore direction. Every 5 minutes the bed profile was measured while the flow was active. A single scan took approximately 30 seconds to complete.

Instruments on the sub-frame   The lower part of the measurement frame consisted of the sub-frame. As stated earlier, the sub-frame could be adjusted in vertical direction during the experiments, with sub-mm accuracy. This has the advantage that during the same condition measurements were performed at different heights above the bed. Besides that, the position of the instrument relative to the bed can be determined. The instruments on the sub-frame are: the Ultra-sonic Velocity Profiler (UVP), the Ultra-High Concentration Meter (UHCM), the Vectrino and the Transverse Suction System (TSS) (see Figure 2.4(c)). For this study, only the data from the Vectrino and the TSS are used.

Vectrino   The Vectrino is a high-resolution acoustic velocimeter used to measure the water velocity in three directions, only the horizontal component in cross-shore direction is used. The Vectrino (see Figure 2.4(c)) uses the Doppler effect to measure current velocity by transmitting a short pulse of sound, recording its echo and measuring the change in pitch or frequency of the echo. The Vectrino actually measures the velocity of (sand) particles moved by the water, instead of the velocity of the water flow like the EMF. The signal is calibrated during the data acquisition, no post-processing calibration is needed.

The data from the Vectrino is used in two ways. Like the EMF on the main-frame, the Vectrino is used as part of the time-averaged velocity profile, i.e. the lowest point in the profile. Besides that, the Vectrino signal is used to validate the near-bed orbital velocity module in Unibest-TC. In Unibest-TC near-bed orbital velocity is calculated at a point just above the wave boundary layer. The main purpose of the Vectrino was to measure the flow velocity within the boundary layer, to compare the results with the detailed UVP measurements. However, during some experiments the Vectrino was raised and measured outside the boundary layer, at approximately 10 cm above the bed. These measurements are used to validate the time-dependent near-bed orbital velocity.

TSS   The TSS, transverse suction system, is used to determine the time-averaged sediment concentration simultaneously at several heights above the bed (see Figure 2.4(c)). Samples are sucked in a direction normal to the ambient water motion. Five intake nozzles, positioned at different heights above the bed, were used to measure the sediment concentration. Initially the nozzles were positioned at 0.05, 0.08, 0.12, 0.18 and 0.28 m above the mean bed level, but during the experiments, the vertical position was varied between ∼2 cm and ∼42 cm above the bed. For a period of approximately 20 minutes samples were collected into 10 liter buckets. The samples consisted of water and sediment. Afterwards the volume of the water and the sediment were determined, where the volume of the sediment was determined using a graduated cylinder. The volume of the sediment is converted into the dry weight using a calibration table. The time-averaged concentration is determined by dividing the weight of the sediment through the volume of the water.

In the case of currents, the intake velocity must exceed the ambient flow velocity more than three times (Bosman et al., 1987). With waves, larger peak velocities may occur in the ambient flow. Bosman et al. (1987) stated that this will only lead to a small systematic error of approximately 5%.

Bosman et al. (1987) also discusses a multiplication factor. This factor is used to correct for the fact that the nozzles are placed in a direction normal to the flow instead of in line with the flow. The dimensionless multiplication factor β is related to the median grain size D_{50}:

$$\beta = 1 + \frac{1}{3} \arctan \frac{D_{50}}{D_{\mathrm{r}}} \tag{2.2}$$

with $D_{\mathrm{r}} = 0.090$ mm the reference sand diameter. This equation estimates the multiplication factor accurately within 3%. The multiplication factor was already implemented in the tables to convert the volume of the sediment into the weight. The grain diameter used in the calibration table was 192 μm instead of 226 μm during the GWK-experiments. This results in a higher value of the multiplication factor. With a median grain size of $D_{50} = 0.226$ mm, the multiplication factor for these experiments is:

$$\beta = 1 + \frac{1}{3} \arctan \frac{0.226}{0.090} = 1.40 \tag{2.3}$$

Where $\beta = 1.38$ with a median grain size of 192 μm. The difference between the two factors is only 1.5%, nevertheless, the data is corrected for the difference between the two multiplication factors.

Instruments on flume wall

Two sets of instruments were mounted on the flume wall: the wave gauges and three EMF-probes. The data acquisition was performed using a different computer (GWK), compared to the data acquisition of the EMF on the frame and the Vectrino. The main difference is the sample rate, the GWK-computer sampled at 40 Hz instead of 50 Hz.

Wave gauges   A total of 19 capacitance wire wave gauges were attached to the flume wall to record the water surface elevation (see Figure 2.4(b)). The position of all 19 wave gauges is given in Table 2.3. The calibration of the wave gauges was performed during filling the wave flume in 11 steps. The calibration curve is linear, with coefficients determined separately for each gauge. The accuracy of the wave height measurements is ± 1 cm (Dette et al., 2002).

Table 2.3: Wave gauge position along the flume.

WG number	x-pos [m]	WG number	x-pos [m]
1	50.1	11	106.64
2	52.2	12	111
3	55.9	13	118
4	61.3	14	126.22
5	79.05	15	140
6	81.15	16	162.4
7	84.85	17	180
8	90.25	18	216
9	97.3	19	236
10	102.09		

EMF (flume wall)   Three EMF probes were mounted on the flume wall at +106.4 m from the wave paddle (see Figure 2.4(b)). Like the EMF on the main-frame, these three EMF probes are used to measure flow velocities simultaneously in two perpendicularly oriented directions, only the horizontal component is used in this study. The data is used for three time-averaged points in the mean velocity profile, at 0.70 m, 1.80 m and 2.50 m above the initial bed level.

Instruments under the sand bed

The CCM, conductivity concentration meter, is used to measure time depended sediment concentrations. The CCM is capable of measuring high sand concentrations ($\approx 100 - 1600$ g/l). Three CCM-probes were installed in a waterproof tank buried under the sand bed. The three probes could be moved up and down using a remotely controlled vertical positioning system. For this study, the instrument is used to determine the position of the bed. Before and after each experiment, the bed level was determined. Because the position of the sub-frame relative to the CCM was known, the height of the instruments on the sub-frame relative to the bed can be determined.

Movable carriage

Bed level measurements were carried out with a mobile carriage, which allows profiling without draining the flume along a large part of the wave flume (see Figure 2.4(d)). The profiler consists of a 7.5 m long beam equipped with three parallel mounted plastic rollers. The angular position of the beam is recorded and converted into position and elevation information. Before and after each test, the bed profile was measured in the middle of the flume. The measurement error in the vertical is estimated to be ±50 mm and in the horizontal ±250 mm (Dursthoff et al., 1997).

2.2   Results

2.2.1   Wave propagation

The wave height is measured using 19 wave gauges mounted on the flume wall. For the validation of Unibest-TC, the root-mean-square wave height H_{rms} has to be determined. The root-mean-square of a variable x is the square root of the mean squared value of x:

$$x_{\mathrm{rms}} = \sqrt{\frac{\sum_{i=1}^{n} x_i^2}{n}} \tag{2.4}$$

The root-mean-square wave height from all individual waves within a condition is determined, indicated by a black dot for each wave gauge in Figure 2.5. The error bars represent the standard deviation per wave gauge, also determined over all individual waves. In the figures, the initial bed profile is also shown.

From all four figures it becomes clear that the wave height is more or less constant until wave gauge 17 (+180 m from the wave paddle). Figure (d), and to a smaller extent Figures (a) and (c), show large differences in wave height between neighboring wave gauges, up to 25 cm. No clear explanation is found in the unprocessed data for these differences. No systematic error was found, neither per wave gauge, nor per test condition.

From Figures (a), (b) and (d) it appears that the wave height increases around wave gauge 18 (+216 m). This increase in wave height is known as wave shoaling and is particularly pronounced just before wave breaking. At wave gauge 19 (+236 m), a decrease in wave height is noticeable. This indicates that the waves were breaking between wave gauge 18 and 19. It turns out that the waves break close to the nearshore bar. The exact point of breaking can not be determined accurately from the data from the wave gauges. Near the point of breaking, the position of the wave gauges was not optimal enough to give a clear point where the waves were breaking during the experiments. However, from observations during the experiments, it appeared that the waves were breaking at approximately the same cross-shore position during each measurement. Figure (d) does not show an increase in wave height at wave gauge 18 like in the other three figures. From the location of the bar, further offshore compared with the other three figures (see also Figure 2.15), the point of shoaling and breaking should also be further offshore, probably between wave gauge 17 and 18. But clear proof for this can not be deduced from the data.
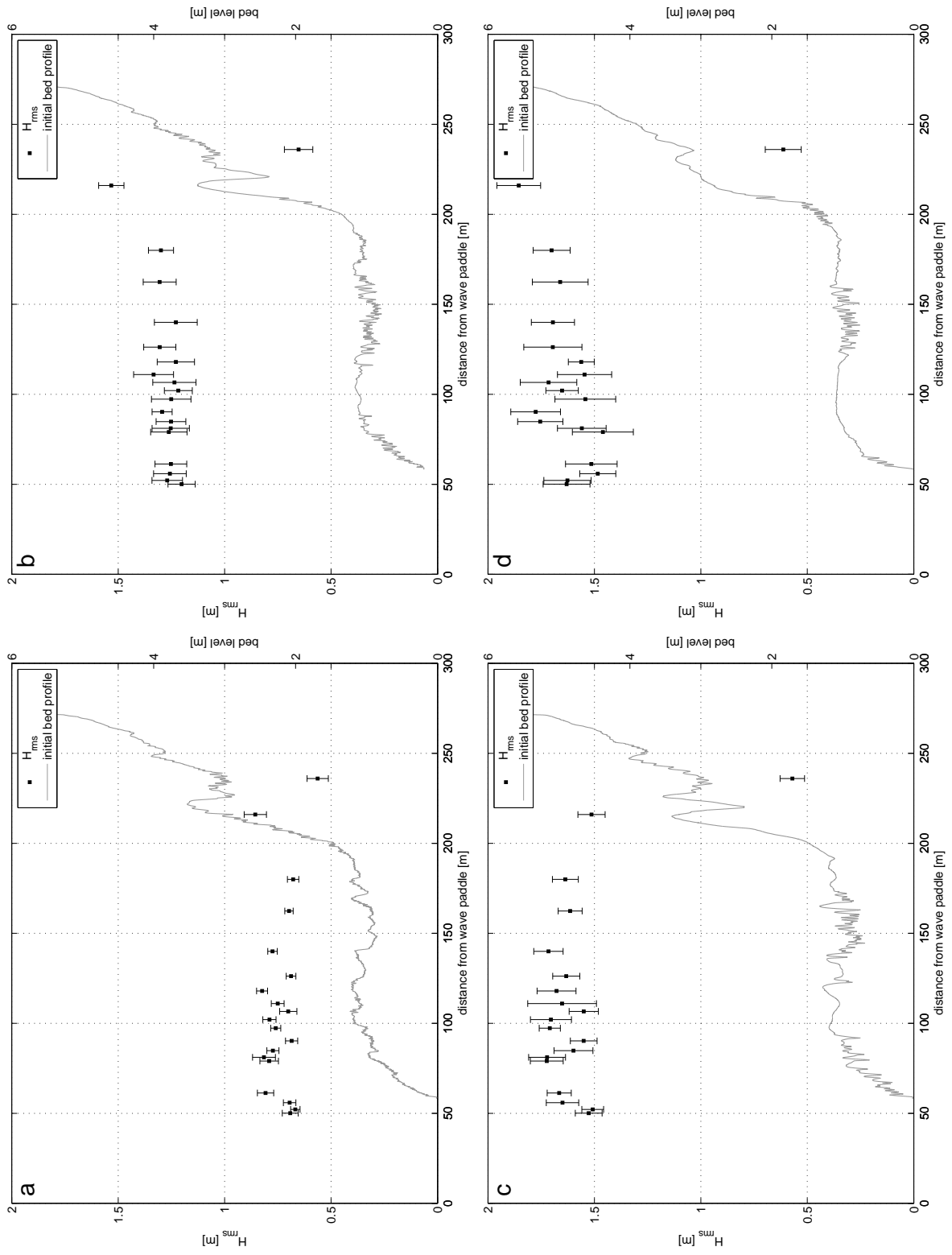
Figure 2.5: Measured root-mean-square wave height: (a) condition H07, (b) condition H12, (c) condition H15 and (d) condition H15 (calibration).

2.2.2   Mean velocity profile

The mean velocity profile is constructed from 5 flow velocity instruments on different heights above the bed. The data from the three EMF-probes mounted on the flume wall, the EMF on the measurement frame and the Vectrino are used to construct the mean velocity profile. Within each condition, the mean velocity per instrument is calculated over a period of 50 waves. This is done several times within each condition, to account for differences in mean velocity during a condition. This results in a set of at least six mean velocities per instrument per condition. The average and the standard deviation of these mean velocities are determined. The results are shown in Figure 2.6. The points represent the time-averaged velocities per instrument and the errorbars denote the standard deviation of the mean velocity.

Figure 2.6 shows only offshore-directed time-averaged velocities. This results from the fact that during a wave cycle, the time-averaged velocities between a wave crest and a wave trough are always positive. During the experiments, no net transport of water was present in the flume. Based on continuity, the zero net transport of water results in a time-averaged negative velocity underneath the wave trough.

The theoretical depth averaged velocity below the trough of the wave can be calculated using the following formula, which is based on linear wave theory and ignores the contribution of the wave roller:

$$\overline{u} = -\frac{gH^2}{8ch} \tag{2.5}$$

with g the acceleration due to gravity, H the wave height, c the wave celerity ($= \sqrt{gh}$ for shallow water conditions) and h the water depth. For all four conditions, the calculated depth averaged velocities are shown in Table 2.4, with the wave height based on the root-mean-square wave height at wave gauge 12 (+111 m):

Table 2.4: Depth averaged velocity.

Test condition	$\overline{u}$ [m/s]	H_{rms} [m]
H07	-0.034	0.75
H12	-0.106	1.33
H15	-0.163	1.65
H15 (calibration)	-0.143	1.55

In all four graphs the calculated depth averaged velocity is indicated by the dashed line. For all four conditions the measured time-averaged flow velocities lie around the dashed line. This suggests that the measured velocities are of the right order of magnitude, and direction.

From both the depth averaged velocities from Table 2.4 and the measured mean velocities it turns out that with increasing wave height, the time-averaged velocity also increases. Both Figures (c) and (d) have the same design wave height of 1.5 m. But at the measurement frame, the wave height differs between these conditions. This could be caused, for instance, by differences in bed level. The difference in wave height at the measurement frame causes also a difference in the time-averaged velocities. At almost all heights above the bed the velocities in Figure (c) are higher compared with Figure (d).

In the following, the shape of the measured velocity profile is discussed. From figures (b) to (d) it turns out that with increasing height from the bed, the time-averaged velocity becomes increasingly negative. The velocity at 1.14 m above the bed (EMF-frame) deviates from this suggestion. Besides the difference in height above the bed between the instruments, there are also differences in the horizontal position. The EMF-probes mounted on the wall are positioned closer to the wall compared to the EMF on the frame. The flow velocity closer to the wall should be lower compared with the velocity in the middle of the flume, because of more wall boundary effects. However, Figure 2.6 shows the contrary. There is also a difference in the cross-shore

position of the instruments. The EMF on the frame is positioned approximately 4 meters in offshore direction compared to the EMF-probes on the wall. Differences in wave height and shape of the waves could result in differences in flow velocity. Figure A.1 shows the ensemble-averaged water elevation signal over 50 waves of the wave gauges near the EMF-probes mounted on the wall (wave gauge 11) and in front of the measurement frame (wave gauge 12), for both condition H12 and H15. Figure (a) shows hardly any differences between the two signals. On the other hand, Figure (b) shows a lower top for wave gauge 11. This should result in a lower time-averaged value. However, the contrary appears from the Figure 2.6.

The time-dependent signal from this EMF (frame) showed an offset when no waves were present in the flume. A detail of the time-dependent EMF signal is shown in Figure A.2. An offset of approximately 1-2 cm/s before each experiment was found. In Figure 2.6 the values for this EMF are corrected for this offset. But still it turns out that the value of this EMF deviates from the shape of the velocity profile suggested by the other instruments. With this correction made to the data and considering the suggestions above, it has been chosen to exclude the EMF on the frame any further for the remainder of the study.

2.2.3 Near-bed orbital velocity

The near-bed flow velocity was measured with the Vectrino. For each test condition, the Vectrino was raised to approximately 10 cm above the bed, which is outside the wave boundary layer. This gives a good comparison with the near-bed orbital velocity predicted by Unibest-TC. Figure 2.7 (a) shows the time-dependent Vectrino signal. Over a period of 50 waves, the Vectrino signal has been ensemble-averaged. Positive values represent onshore-directed velocities, negative values represent offshore-directed velocities.

Figure 2.7 (a) shows that both H15 conditions do not show the same results. A difference exist in the height above the bed, where condition H15 was positioned approximately 5 cm lower than H15 (calibration). Another thing that plays a roll here is the bed level during the experiments. Figure A.5 shows that during the whole length of the experiments, the bed was flat for condition H15. On the other hand, Figure A.6 shows that at the end of condition H15 (calibration) a bed form with a height of approximately 20 cm was situated near the measurement frame. The only time-dependent Vectrino measurement at a height of about 10 cm above the bed was obtained at the end of this condition, so this might be a explanation for the difference between the two signals.

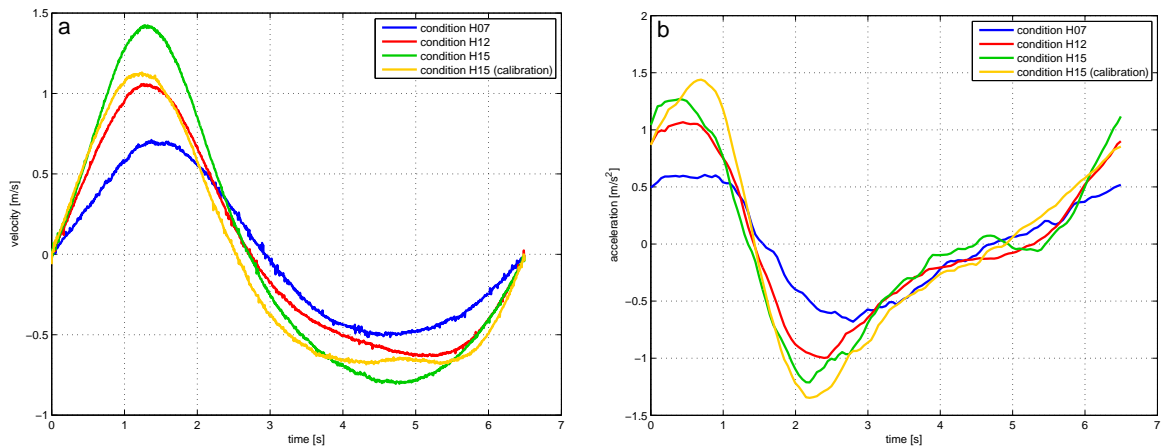**Figure 2.7:** Near-bed orbital velocity: (a) ensemble-averaged velocity and (b) acceleration.

In Table 2.5 some characteristic values are listed for all four wave conditions. The table includes the height of the Vectrino above the bed, the maximum onshore and offshore velocity, U_{max} and U_{min}, the time-averaged velocity $\langle U \rangle$, the root-mean-square velocity U_{rms}, the third order velocity
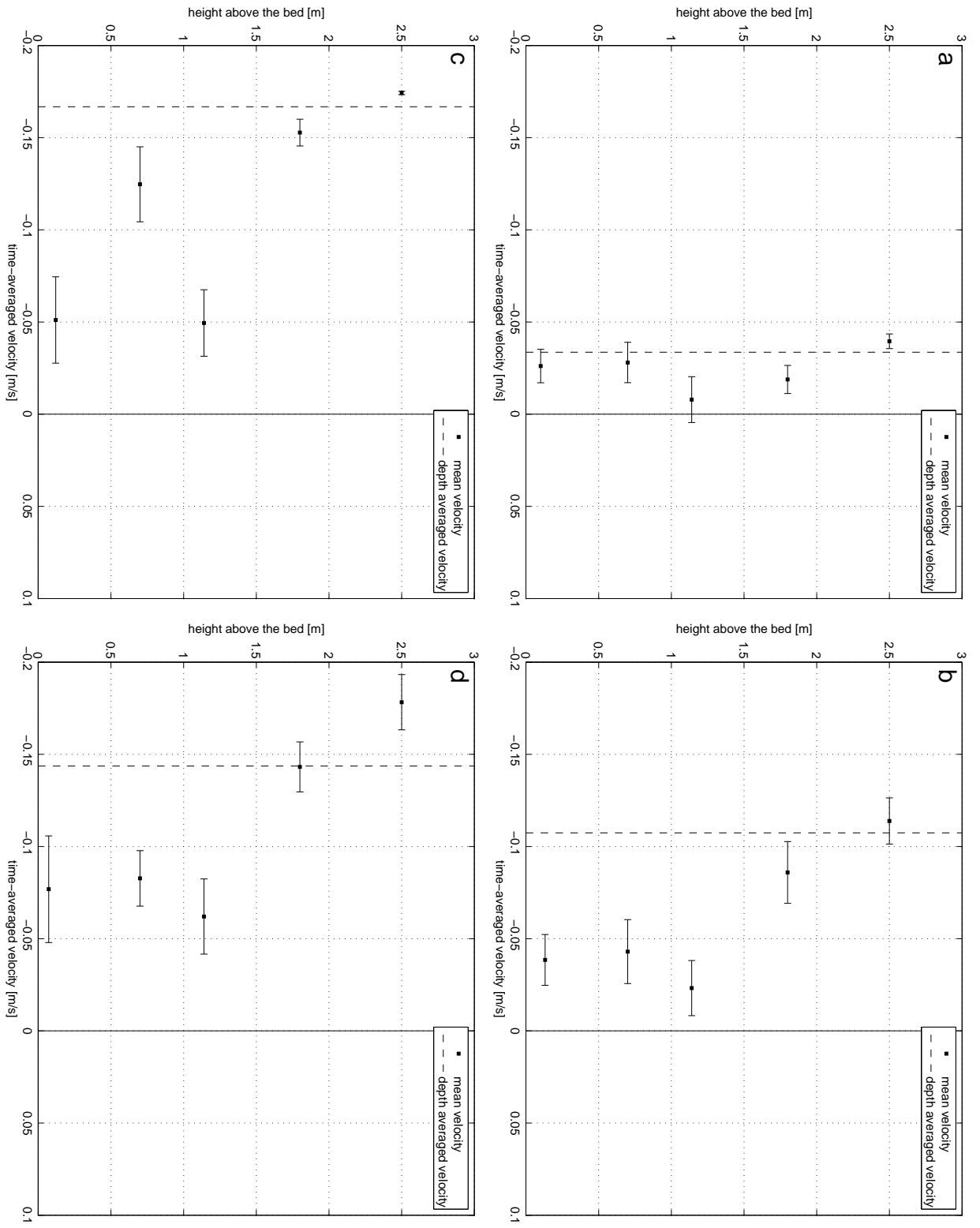
Figure 2.6: Measured mean velocity profile: (a) condition H07, (b) condition H12, (c) condition H15 and (d) condition H15 (calibration).

Table 2.5: Measured flow velocity characteristics.

Test condition	height [mm]	U_{max} [m/s]	U_{min} [m/s]	$\langle U \rangle$ [m/s]	U_{rms} [m/s]	$\langle U^3 \rangle$ [m³/s³]	R [-]	β [-]	Ψ_{max} [-]
H07	100	0.69	-0.54	-0.026	0.42	0.013	0.56	0.47	128
H12	130–140	1.02	-0.67	-0.039	0.58	0.070	0.60	0.52	284
H15	70	1.39	-0.84	-0.051	0.75	0.21	0.62	0.52	526
H15 (calibration)	120	1.11	-0.70	-0.077	0.65	0.076	0.58	0.51	304

moment $\langle U^3 \rangle$, the degree of orbital flow skewness R, the degree of acceleration skewness β and the wave mobility number Ψ_{max}.

The root-mean-square velocity U_{rms} is determined by applying Equation 2.4 on the 50 wave long velocity signal, from where the ensemble-averaged velocity is constructed. The root-mean-square velocity is often determined for studies like this. Therefore, it is a good comparison to other hydrological/morphological studies. The third order velocity moment $\langle U^3 \rangle$ is determined by taken the mean of all measured velocities to the power 3. It is assumed that a linear relation exists between the third order velocity moment $\langle U^3 \rangle$ and the net transport rates (Dohmen-Janssen and Hanes, 2002).

The degree of orbital flow skewness is a function of the maximum onshore and offshore velocity, defined by:

$$R = \frac{U_{\mathrm{max}}}{U_{\mathrm{max}} - U_{\mathrm{min}}} \tag{2.6}$$

The value of R is a measure for the degree of velocity skewness of the orbital velocity. A value of 0.5 denotes a perfect horizontal symmetric shape. In the case of trochoidal waves, as used here, the value of R should be larger than 0.5.

The degree of acceleration skewness is defined as follows:

$$\beta = \frac{\dot{U}_{\mathrm{max}}}{\dot{U}_{\mathrm{max}} - \dot{U}_{\mathrm{min}}} \tag{2.7}$$

with $\dot{U}_{\mathrm{max}}$ and $\dot{U}_{\mathrm{min}}$ the maximum and minimum acceleration respectively. With $\beta < 0.5$ the wave is "forward-leaning", with $\beta > 0.5$ the wave is "backward-leaning". For $\beta = 0.5$ the wave has no acceleration skewness.

The wave mobility number is defined by:

$$\Psi_{\mathrm{max}} = \frac{U_{\mathrm{max}}^2}{\Delta g D_{50}} \tag{2.8}$$

where $\Delta = (\rho_s - \rho_w)/\rho_s = 1.65$ is the relative sediment density, with ρ_s the sediment density and ρ_w the water density and g the acceleration due to gravity. The wave mobility number is a parameter for the prediction of the transport regime. O'Donoghue et al. (2006) showed that the riple regime corresponds to $\Psi_{\mathrm{max}} < 190$, a transition regime corresponds to $190 < \Psi_{\mathrm{max}} < 300$ and a flat bed sheet-flow regime corresponds to $\Psi_{\mathrm{max}} < 300$.

Table 2.5 clearly shows that with increasing wave height, the flow velocity becomes higher, both for the on- and offshore directed velocities. Besides that, an increase in wave height results in a more pronounced velocity skewness R of the near-bottom velocity signal, i.e. a peaked crest and a flattened trough. This does not hold for condition H15 (calibration). From Figure 2.7 it turns out that there is a little hump in the trough. It was already mentioned, that with increasing wave height, the velocity skewness also increases. The calculated R confirms that suggestion. Also, the point of flow reversal between on- and offshore velocity shifts to the left with increasing wave height. This is also an indication that with increasing wave height the waves become more velocity skewed.

The acceleration skewness is determined with the degree of acceleration skewness β. Figure 2.7 (b) shows the time-dependent acceleration, determined from the time-dependent velocity signal

of the Vectrino. Condition H07 shows a value of $\beta < 0.5$, this means that the wave is "forward-leaning". Where condition H12, H15 and H15 (calibration) are "backward-leaning". For all conditions it applies that the value of β is close to 0.5, so the differences in acceleration skewness between the four conditions are not that pronounced.

The values of the mobility numbers Ψ_{max} in Table 2.5 shows that condition H07 is in the ripple regime. Figure A.3 confirms this suggestion, the sonar scans show clearly the presence of ripples during these tests. Condition H12 is in the intermediate regime, although the mobility number is very close to the lower limit of the sheet-flow regime. Figure A.4 clearly shows the appearance of some smaller scale ripples during these measurements. Condition H15 and H15 (calibration) are in the sheet-flow regime. Especially condition H15 shows a flat bed during all tests, see Figure A.5. Condition H15 (calibration) however, shows some larger bed forms to the end of the last test (Figures A.5 (c) and (d)).

2.2.4   Mean concentration profile

The time-averaged concentration profile is constructed from the measured sediment samples from the transverse suction system (TSS). The TSS was mounted on the sub-frame, the sediment samples were taken from heights between $\sim$2 to $\sim$43 cm above the bed. The heights above the bed are obtained from the bed level measurements performed by the CCM-probes. For almost all bed level measurements, the before and after measurements are within a 1 cm. This means that during the individual tests, the bed varied only within 1 cm. The heights of the suction tubes above the bed are therefor quite reliable. It should be remarked that this is not the case for all test. The second test of condition H07 showed a difference of approximately 4 cm between the begin and end bed level. Figure A.3 shows pronounced ripples throughout the whole length of the experiments. With ripple heights between 5 and 15 cm, the difference between the initial and final bed level of 4 cm is not unusual. Condition H15 (calibration) showed a lot of uncertainty at the end of the last test, already mentioned in Section 2.2.3.

Figure 2.8 shows the time-averaged sediment concentration for condition H15. The errorbars denote the 5% random error, as described in Section 2.1.3. The figure clearly shows that with increasing height from the bed, the time-averaged concentration decreases. Close to the bed, the sediment concentration increases rapidly. From this figure, it appears that the vertical distribution is not linear, emphasized by both trendlines, which are based on a power law-based (dashed line, Equation (2.9)) and an exponential-based expression (dashed-dotted line, Equation (2.10)).
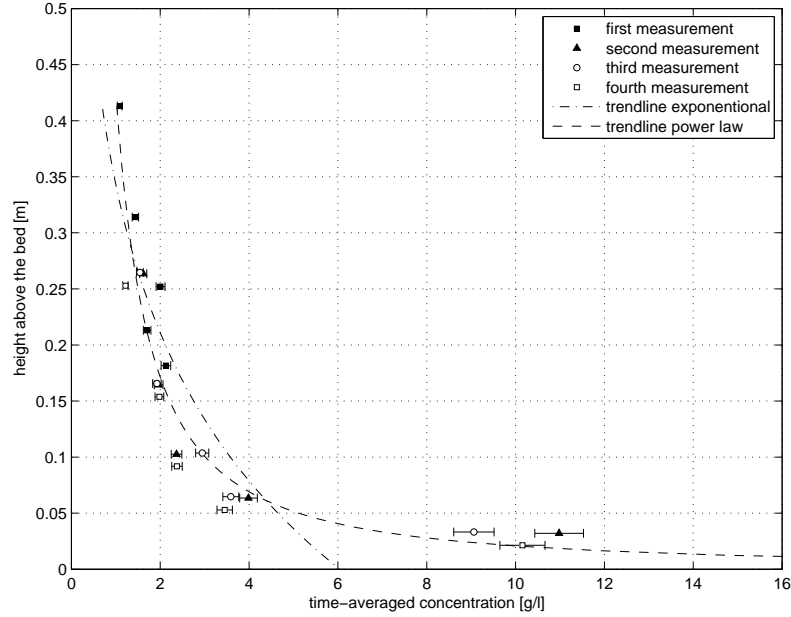
Figure 2.8: Mean concentration profile (condition H12).

Ribberink and Al-Salem (1994) conducted tunnel experiments in the rippled bed and sheet flow regime. The time-averaged concentration profiles were tested against two expressions for the vertical distribution of the concentration.

Smith (1977) derived an expression for the time-averaged suspended sediment concentration over a plane bed. He assumes that the turbulent eddy viscosity is equal to the sediment mixing coefficient ε_s, is constant in time and is linearly increasing with distance z above the bed. This resulted in a power law distribution of the time-averaged concentration (also used in Figure 2.8):

$$\langle c(z) \rangle = c_a \left(\frac{z_a}{z} \right)^{\alpha} \tag{2.9}$$

with c_a the reference concentration at $z = z_a$, z_a the reference level near the bed and $\alpha = W_s z / \varepsilon_s$ the concentration decay parameter, with W_s the settling velocity of sediment. According to this formula, the time-averaged concentration corresponds to a straight line on log-log scale. The time-averaged concentration data from all four conditions are shown in Figure 2.9. The straight lines, using linear regression, in this figure are fitted to the data, with the following values for c_a and α:

Table 2.6: Values for c_a and α.

Test condition	c_a [g/l]	α [-]	R^2 [-]
H07	134.5	1.53	0.93
H12	17.4	0.76	0.91
H15	10.6	1.00	0.98
H15 (calibration)	6.97	0.65	0.80

In Table 2.6 the reference height z_a is 1 cm above the bed. The coefficient of determination R^2 shows how well the straight lines fit the data, where $R^2 = 1$ denotes perfect agreement. With R^2 close to 1, it appears that condition H12, H15 and H15 (calibration) show good comparison with the power law based expression.

Ribberink and Al-Salem (1994) found a constant concentration decay parameter α of 2.1 in all test conditions (with $T = 6.5$ s, $u_{\rm rms} = 0.3 - 0.9$ m/s and $D_{50} = 210$ μm). Dohmen-Janssen and

Hanes (2002) showed that under full scale waves α has a lower value of about 0.55 (with $T = 6.5$ s, $u_{rms} = 0.6$ m/s and $D_{50} = 240$ μm). The results of the present experiments show also a lower value for α. So the suggestion proposed by Dohmen-Janssen and Hanes (2002) applies also for these experiments.

Bosman and Steetzel (1986) derived an logarithmic based expression for the time-averaged suspended sediment concentration over a rippled bed, based on an extensive set of measurements in rippled-bed conditions. They showed that the vertical distribution of time- and bed-averaged suspended sediment concentration can be described with a constant sediment mixing coefficient ε_s above a bed, with the following analytical solution:

$$\langle c(z) \rangle = c_0 \exp \left(\frac{-z w_s}{\varepsilon_s} \right) \tag{2.10}$$

with z the vertical coordinate with respect to the average bed level, w_s the settling velocity of sediment, ε_s the mixing coefficient for vertical sediment mixing and c_0 the (extrapolated) concentration at $z = 0$. Figure 2.10 shows the time-averaged concentration data on a log-linear scale with an exponential trendline fitted to the data, using linear regression.

Table 2.7: Values for c_0 and r_c.

Test condition	c_0 [g/l]	r_c [m]	R^2 [-]
H07	6.90	0.128	0.96
H12	6.04	0.191	0.71
H15	2.17	0.142	0.96
H15 (calibration)	2.66	0.223	0.69

Table 2.7 shows the reference concentration c_0 at $z = 0$ and the concentration decay length r_c derived from (2.10):

$$r_c = \frac{\varepsilon_s}{w_s} \tag{2.11}$$

Condition H07 shows better agreement with this expression for the current profile than the power law based expression, where R^2 is in this case closer to 1. Ribberink and Al-Salem (1994) and Van der Werf (2006) showed that there is a simple linear relationship between the concentration decay length and the ripple height:

$$r_c \sim \eta \tag{2.12}$$

The ripple profiler images from condition H07 (Figure A.3) show ripple heights between 5 and 15 cm. The concentration decay length of condition H07 is approximately 13 cm, which is similar to the ripple heights from Figure A.3.

Both Table 2.6 and Table 2.7 show that condition H07 is best represented by the logarithmic based expression for the concentration profile. All other conditions show a better R^2 with the power law based expression. This is in agreement with Ribberink and Al-Salem (1994), confirmed by Van der Werf (2006), where it is stated that the logarithmic based expression is best suitable for rippled bed conditions. On the other hand, the power law based expression is best suitable for sheet flow conditions.

2.2.5   Total sediment transport

The net transport rates are obtained by solving the sediment mass balance. This mass balance is solved between two successive data points, starting at a grid point at the start of the bed profile at approximately +55 m from the wave paddle. It is assumed that no sediment is transported past this point. Figure 2.11 visualizes the principle of the sediment mass balance. No sediment passes x_1 either from the left or from the right. A change in bed level will result in a net sediment
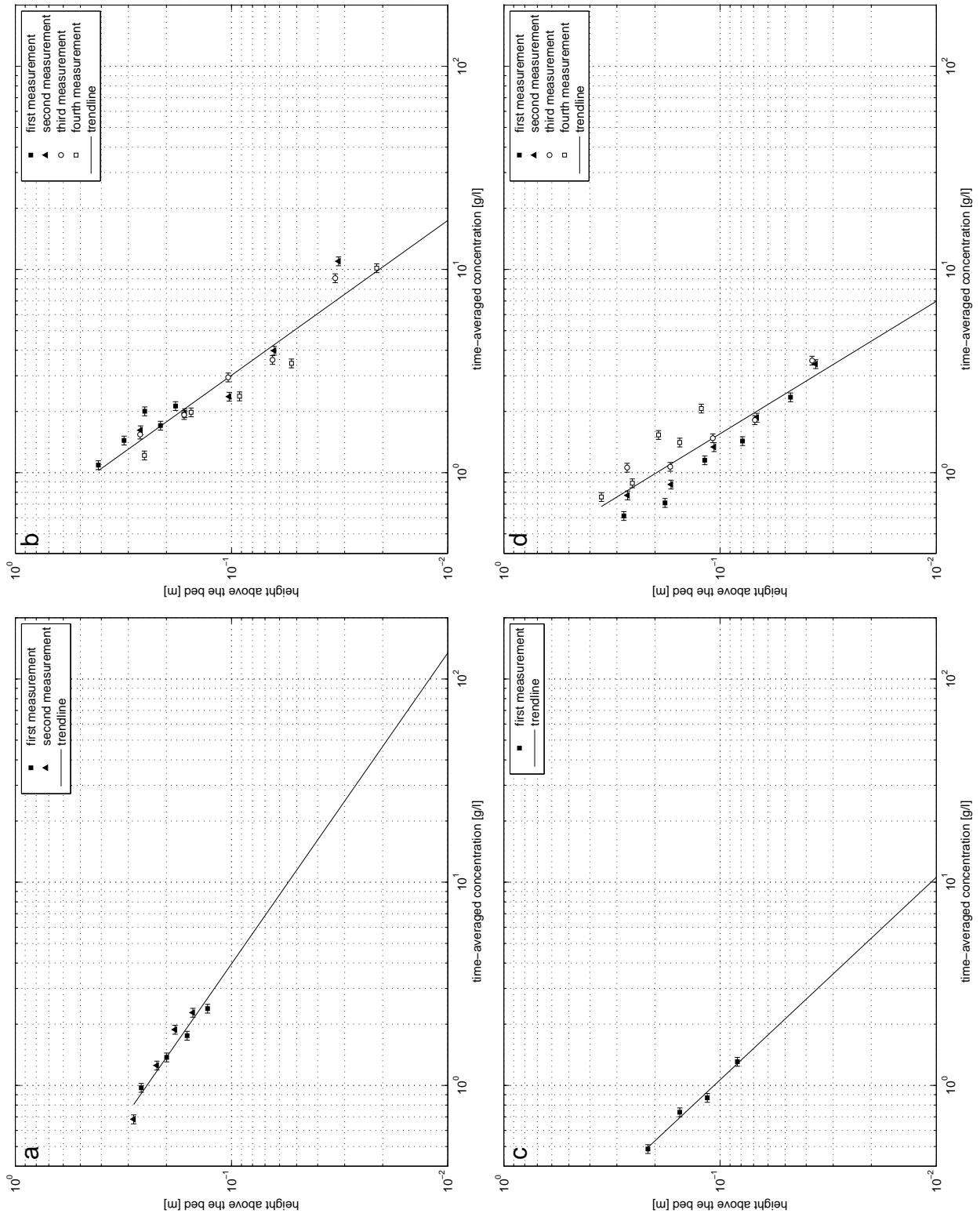
Figure 2.9: Measured mean concentration profile on log-log scale: (a) condition H07, (b) condition H12, (c) condition H15 and (d) condition H15 (calibration).
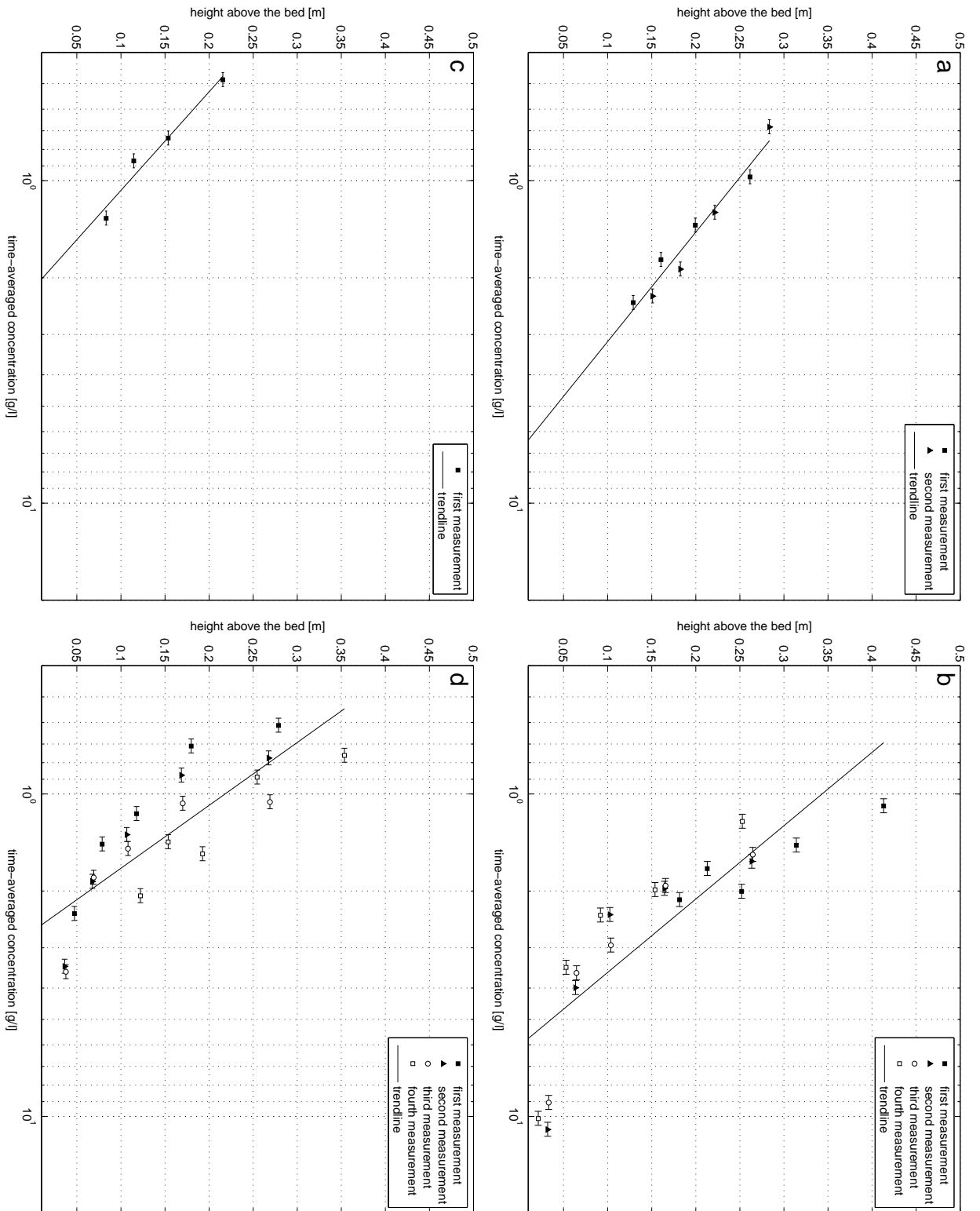
Figure 2.10: Measured mean concentration profile on log-linear scale: (a) condition H07, (b) condition H12, (c) condition H15 and (d) condition H15 (calibration).

transport. In Figure 2.11 erosion has occurred. With the assumption $\langle q(x_1) \rangle = 0$, the net sediment transport is directed to the right, or in onshore direction.
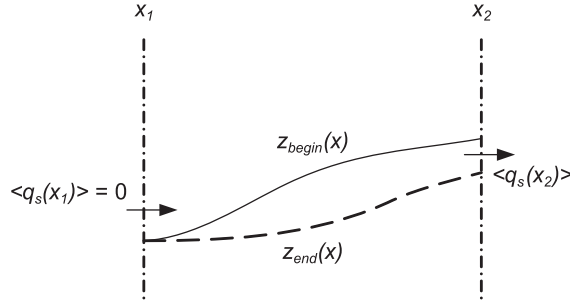

Figure 2.11: Mass balance sediment.

The amount of sediment transported is determined using the following formula:

$$[\langle q_s(x_1) \rangle - \langle q_s(x_2) \rangle] \Delta t = (|x_2 - x_1|)[z_{end}(x) - z_{begin}(x)](1 - \varepsilon) \tag{2.13}$$

with Δt the duration of the experiment and $\varepsilon = 0.4$ the porosity of the sediment (assumption). With the assumption $\langle q(x_1) \rangle = 0$, this results in:

$$\langle q_s(x_2) \rangle = \frac{(|x_2 - x_1|)[z_{end}(x) - z_{begin}(x)]}{\Delta t}(1 - \varepsilon) \tag{2.14}$$

In the case of erosion, like in Figure 2.11, $[z_{end}(x) - z_{begin}(x)]$ is negative, consequently $\langle q_s(x_2) \rangle$ is positive. For every other grid point the net sediment transport is determined as follows:

$$\langle q_s(x_i) \rangle = \frac{(|x_i - x_{i-1}|)[z_{end}(x) - z_{begin}(x)]}{\Delta t}(1 - \varepsilon) + \langle q_s(x_{i-1}) \rangle \tag{2.15}$$

The results for all four wave conditions are shown in Figure 2.12. The thick black line represents the net sediment transport for the whole duration of the condition, the thin colored lines show the net transport for the individual tests. Positive values suggest onshore sediment transport and negative values suggest offshore transport. Figures (a) to (c) show that the results are not consistent. Two successive experiments show on the one hand only landward transport and on the other hand only seaward transport. This inconsistency may be caused by the cumulative way the net transport rates are determined. Small errors could cause a shift in net transport over the whole profile.

The same applies for the large jumps at the end of the profile, on the right side of the figures. In theory, no sediment should pass the righthand side of the profile, but from the data, this could not be proven. It is possible that the large jumps are caused by three dimensional bed forms. From observations it appeared that three dimensional bed forms were found between +55 and +80 m from the wave paddle and at an area around +150 m from the wave paddle. Only morphological changes in the middle of the flume are recorded by the bed profiler. When bed forms move from one side of the flume to the other (perpendicular to the wave propagation), it appears that a large amount of sediment disappeared. With Equation 2.15 in mind, this could result in an over- or underestimation of the net transport. For example, when a triangular bed form with a base of 2 m and a height of 0.25 shifts from the middle of the flume to the side of the flume during a half hour experiment. This results in a difference in net sediment transport of $\frac{\frac{1}{2}20.25}{1800} = 138.9$ m^2/s, which is in the order of magnitude of the deviations in Figure 2.12. The fact that the net transport calculations show these large deviations at the right hand side of the figures, no attention is paid to the transport rates beyond the measurement location at +111 m from the wave paddle.

Measurements of net transport rates under full surface waves are not often documented. Dohmen-Janssen and Hanes (2002) measured net transport rates in the Large Wave Flume (GWK)
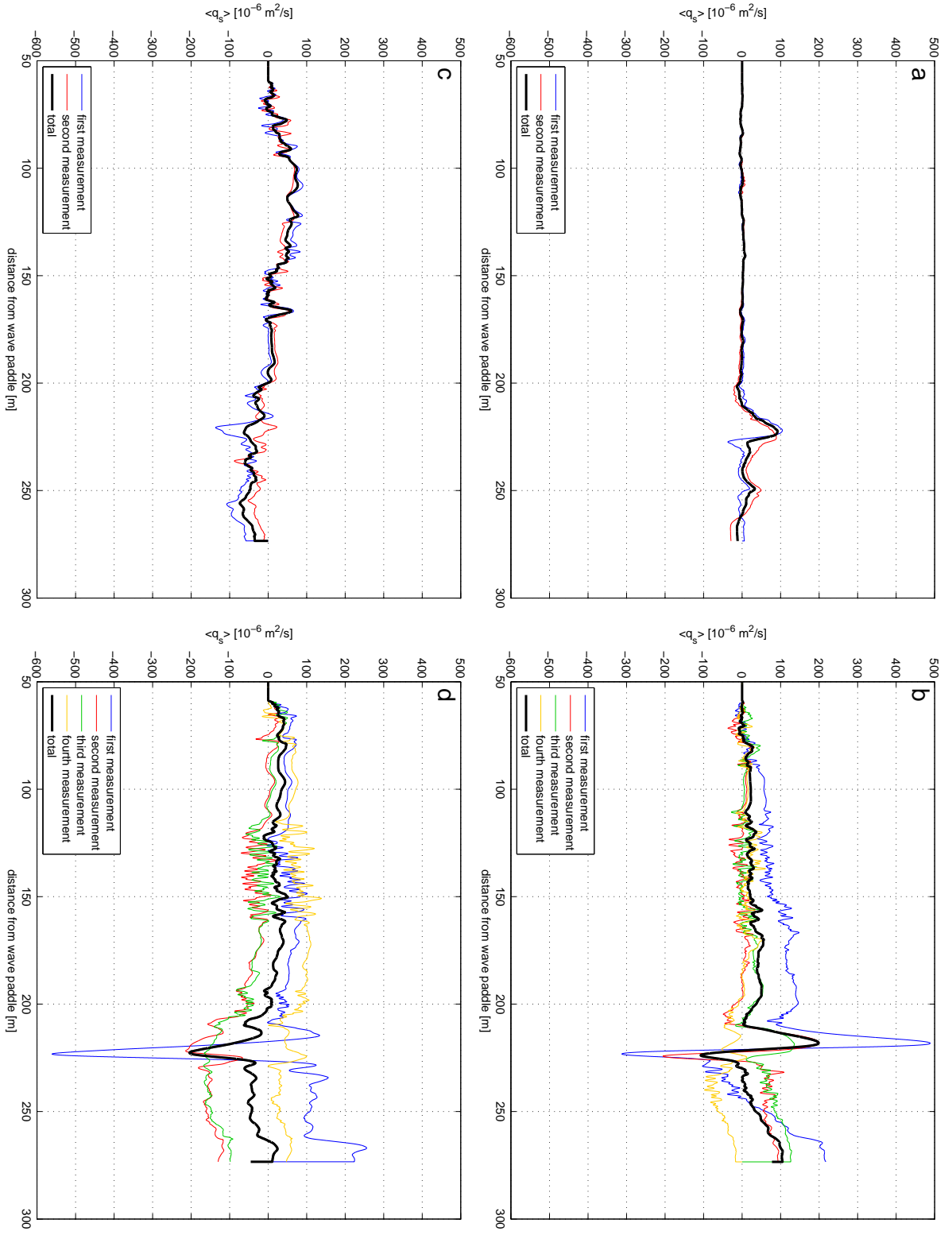
Figure 2.12: Measured net transport rates: (a) condition H07, (b) condition H12, (c) condition H15 and (d) condition H15 (calibration).

in Hannover and compared these measurements with tunnel experiments. From tunnel experiments it appeared that a relationship exists between the net transport rate and the third-order velocity moment, already mentioned in Section 2.2.3. Table 2.8 shows the net transport rates (and their standard deviations) and the third-order velocity moments for all four conditions. Figure 2.13 shows the same data including the data presented by Dohmen-Janssen and Hanes (2002) (full surface waves), Ribberink and Al-Salem (1994) and Hassan and Ribberink (2005) (both tunnel experiments). Both full surface wave experiments and tunnel experiments show that there is a linear relationship between the net transport rates and the third-order velocity moment, indicated by the linear trendlines. Dohmen-Janssen and Hanes (2002) concluded that the measured transport rates from the full surface wave experiments are higher compared to the tunnel experiments. The two sheet-flow conditions from the present study confirm this suggestion. Condition H12 shows a lot of uncertainty, the relative standard deviation is 5 times the average net transport. The ripple condition (H07) shows negative net transport rates. But overall, the dashed trendline confirms the suggestion proposed by Dohmen-Janssen and Hanes (2002).

Table 2.8: Measured third-power velocity moments, net transport rates and the standard deviation of the net transport rates.

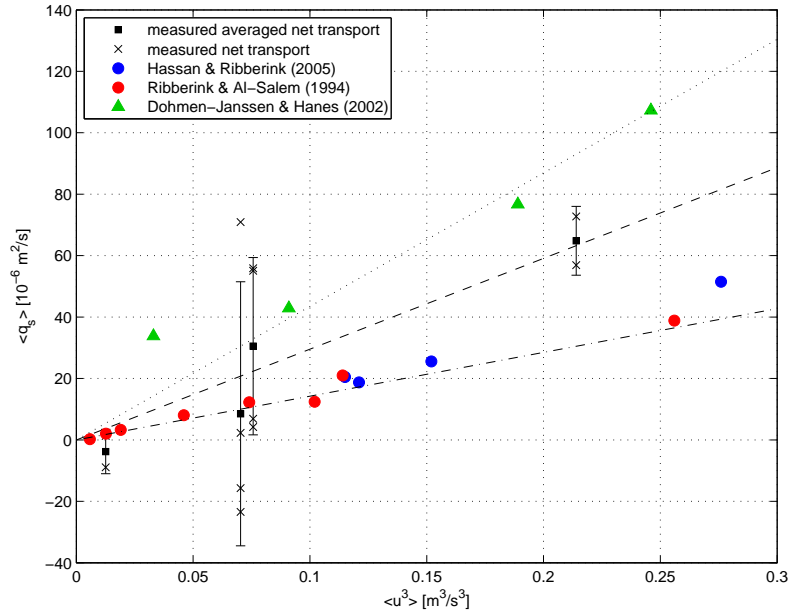| Test condition	$\langle U^3 \rangle$ [m³/s³]	$\langle q_s \rangle$ [m²/s]	σ_{qs} [m²/s]	$\sigma_{qs}/\langle q_s \rangle$ [%]
H07	0.013	-3.81	7.22	189.7
H12	0.070	8.52	42.98	504.5
H15	0.21	64.83	11.21	17.3
H15 (calibration)	0.076	30.51	28.85	94.6

Figure 2.13: Net transport rate as a function of the third-power velocity moment.

2.2.6 Morphological changes

Before and after each experiment, the bed level changes were measured using the bed profiler (see Section 2.1.3). Figure 2.14 show two bed profiles. During each test every 5 minutes a sonar scan was made with the ripple profiler, see Figures A.3 to A.6.

Figure 2.14 (a) shows the final bed profile after condition H07 and Figure (b) after condition H15. Both profiles show a nearshore bar at approximately +220 m from the wave paddle. Figure (b) shows mega ripples between +120 m and +170 m from the wave paddle, with ripple lengths of 1 to 4 m and ripple heights of 0.1 to 0.4 m. The absence of mega ripples between +80 m and +120 m from the wave paddle is probably due to a better preparation of the initial bed in this area. During the experiments, the mega ripples extended offshore towards the measurement location at +111 m. These mega ripples were not observed during condition H07, but smaller bed forms were found. The ripple profiler scans (Figure A.3) show ripple lengths of 0.2 - 0.8 m and ripple heights of 0.05 - 0.15 m. The ripple profiler images of the other conditions do not show ripples with these dimensions. During condition H12 small bed forms appeared (heights up to 0.1 m), but these bed forms were not very mobile. A flat bed was observed during condition H15 throughout all the experiment. Condition H15 (calibration) showed some larger bed forms at the end of the experiment, already mentioned in Section 2.2.3.
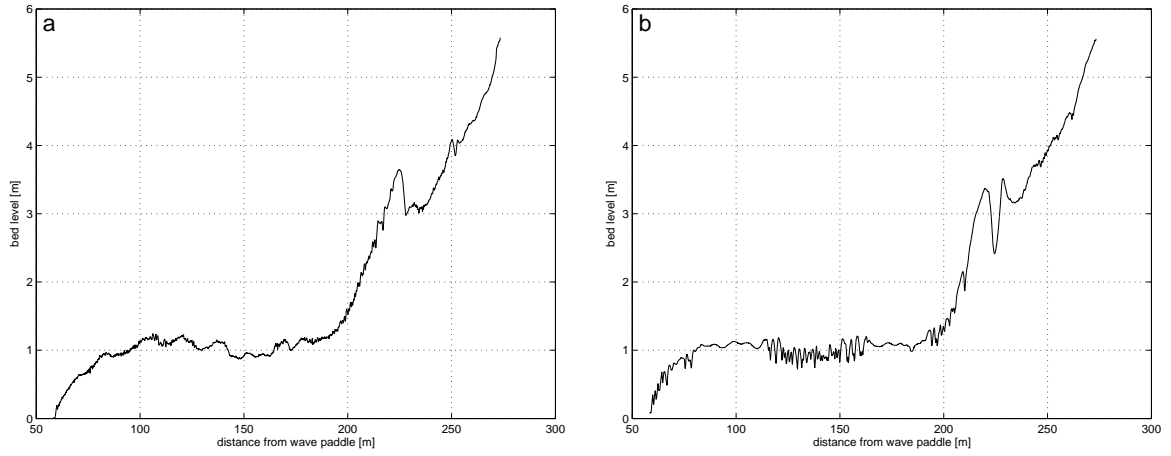

Figure 2.14: Measured final bed profiles: (a) condition H07 and (b) condition H15.

In Figure 2.15 details of the bed level measurements at the nearshore bar from all four conditions are shown. Figures (a) and (b), both with small or intermediate wave heights, show onshore bar movement. The initial profile of condition H15 (calibration) in Figure (d) shows hardly any bar shape. After the first experiment a double bar system is formed and shows small offshore movement of the inner bar. The outer bar hardly moves between the second and fourth measurement. Figure (c) also shows a double bar system. Both inner and outer bar do not show any movement at all. From the literature (e.g. Hoefel and Elgar, 2003) it appears that onshore bar movement occurs in the case of small wave heights, like in Figure (a) and (b). Offshore bar movement occurs in the case of large waves. Small offshore movement occurred during condition H15 (calibration), but hardly any movement appears in condition H15.
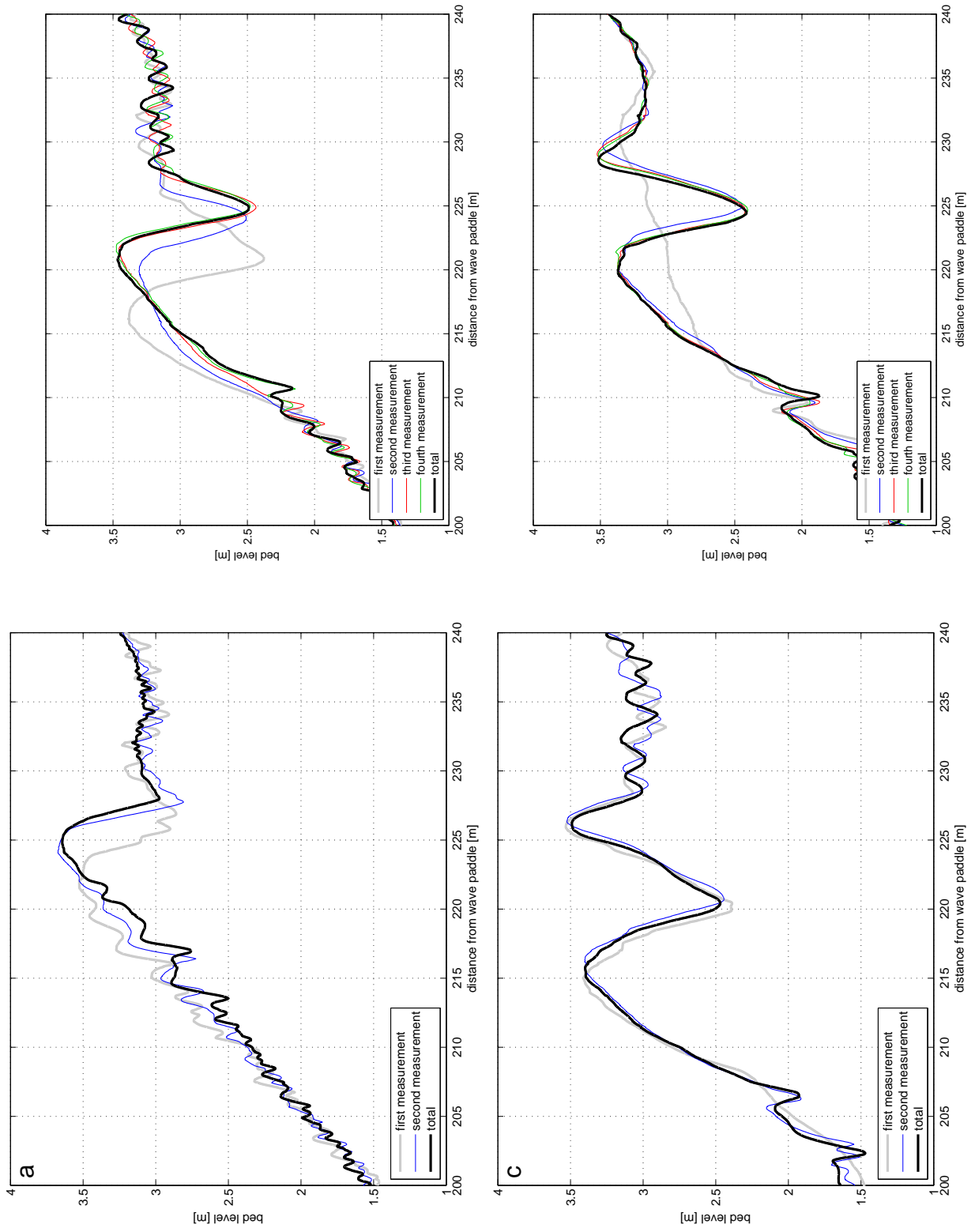
Figure 2.15: Measured bar migration: (a) condition H07, (b) condition H12, (c) condition H15 and (d) condition H15 (calibration).

Chapter 3

Model description

3.1 Model overview

Unibest-TC is a module of the program package Unibest, which stands for UNIform BEach Sediment Transport. All modules of this package consider sediment transports along a sandy coast which locally may be considered uniform in alongshore direction.

Unibest-TC (TC: Time-dependent Cross-shore) is the cross-shore sediment transport module of the Unibest Coastal Software Package. It is designed to compute cross-shore sediment transports and the resulting profile changes along any coastal profile of arbitrary shape under the combined action of waves, longshore tidal currents and wind. The model allows for constant, periodic and time series of the hydrodynamic boundary conditions to be prescribed.

3.1.1 Applicability

The Unibest-TC model can be applied on several coastal problems, e.g.:

- Dynamics of cross-shore profiles;

- Cross-shore development due to seasonal variations of the incident wave field;

- Bar generation & migration;

- To check the stability of beach nourishments;

- To estimate the impact of sand extraction on the cross-shore bottom profile development.

3.1.2 Coordinate system

The x-axis is perpendicular to the shoreline, positive landwards (see also Figure 3.1). The y-axis is rotated 90 degrees counter-clockwise, relative to the x-axis. The z-axis is perpendicular to the x- and y-axis, positive in upward direction. Wave angles are defined between the x-axis and the direction of wave propagation, positive angles counting counterclockwise.
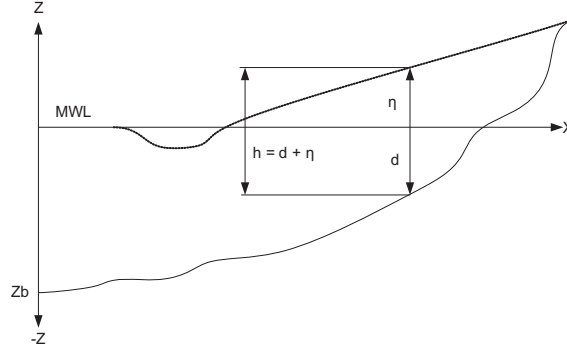
Figure 3.1: Definition of coordinate system and domain (Walstra, 2004).

3.2   Overview of sub-modules

The Unibest-TC model consists of five sub-modules:

- wave propagation module

- mean current profile module

- wave orbital velocity module

- bed load and suspended load transport module

- bed level change module

A schematic representation of the various sub-modules is given in Figure 3.2. Some adjustments have been made to make the model more suitable for the case of regular waves. These adjustments are made in the wave propagation, mean current profile and wave orbital velocity modules. A description of all modules is provided here. For all model formulations a reference can be made to Bosboom et al. (2000) and Walstra and Steetzel (2003).

3.3   Wave propagation

The wave propagation model consists of three first-order differential equations, i.e. the time-averaged wave energy balance, the balance equation for the energy contained in surface rollers in breaking waves and the horizontal momentum balance from which the mean water level set-up is computed. The refraction of the waves is computed using Snell's law, but does not play a roll in this research, since the waves only propagate in cross-shore direction.

The energy balance equation for the organised wave energy E reads:

$$\frac{\partial}{\partial x}\left(Ec_g cos\theta\right) = -D_w - D_f \tag{3.1}$$

where c_g is the wave group velocity, θ the angle of incidence of the wave field (which was 0 during the GWK-experiments), D_w the dissipation of wave energy due to breaking and D_f the dissipation due to bottom friction. The organised wave energy E is defined according to linear wave theory

$$E = \frac{1}{8}\rho_w g H_{\mathrm{rms}}^2 \tag{3.2}$$

where ρ_w is the density of water, g the gravitational acceleration and H_{rms} the root-mean-square wave height.
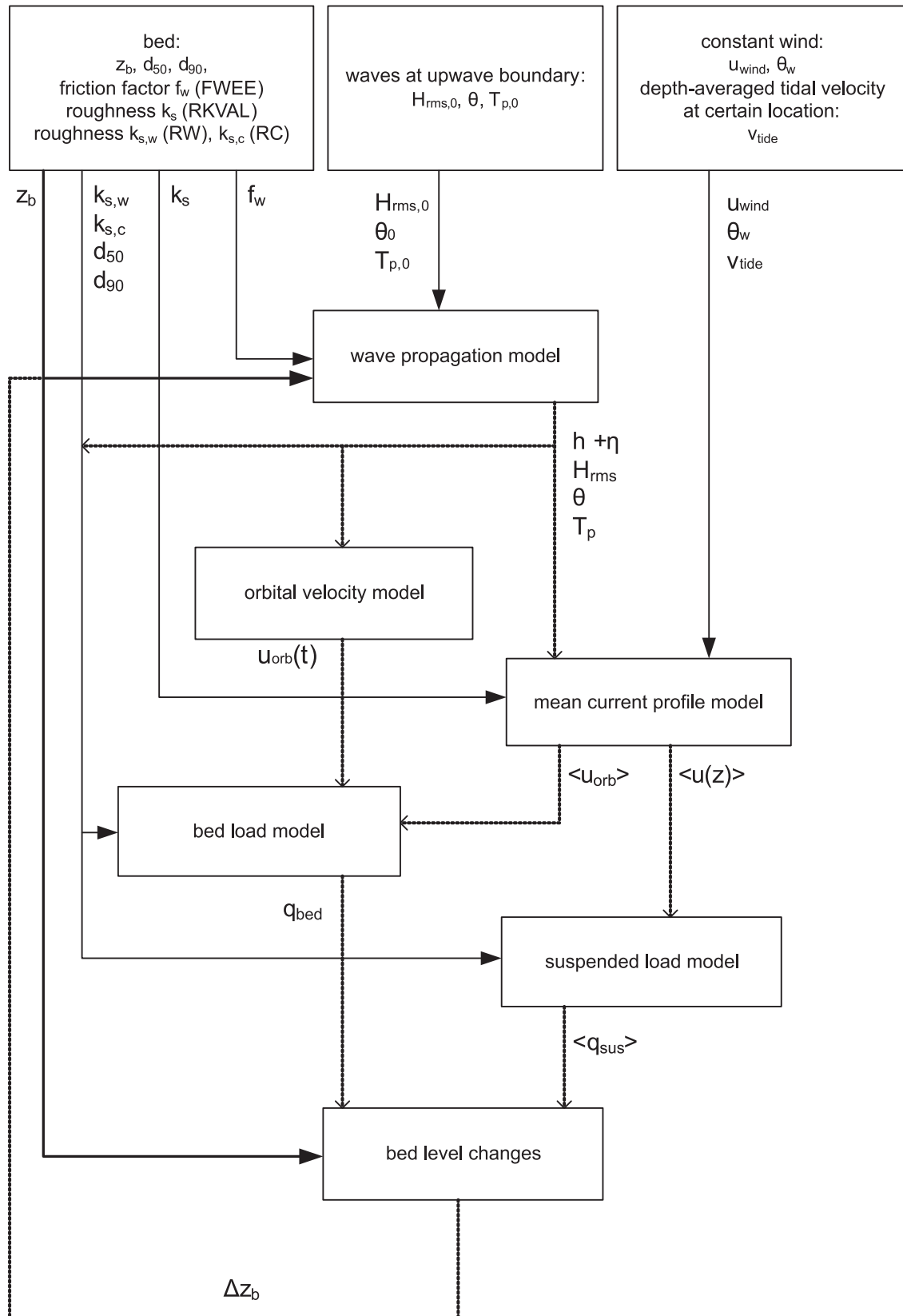
Figure 3.2: Overview of Unibest-TC sub-modules (text in small capitals corresponds to the names in the input file) (Bosboom et al., 2000).

The breaking-wave dissipation is modeled according to the deterministic approach as proposed by Battjes and Janssen (1978), modified by Roelvink et al. (1995), and reads:

$$D_w = \frac{1}{4}\rho g \alpha f_p H_{\max}^2 Q_b \tag{3.3}$$

where $f_p = 1/T_p$ is the peak frequency, $H_{\max}$ the maximum wave height, Q_b the fraction of breaking waves and α a dissipation coefficient. The maximum wave height $H_{\max}$ is defined as a function of the local water depth, according to:

$$H_{\max} = \frac{0.88}{k} \tanh\left(\frac{\gamma k h_r}{0.88}\right) \tag{3.4}$$

with k the local wave number, h_r the local water depth and γ the wave height-to-depth ratio. The local water depth h_r at a particular grid point is obtained from the weighted water depths seaward of this computational grid point. Battjes and Stive (1985) assumed γ to be cross-shore constant, but variable in time. However, Ruessink et al. (2003) showed that γ is a locally varying parameter that increases linearly with the product of the local wave-number and water depth kh

$$\gamma = 0.29 + 0.76 kh \tag{3.5}$$

In the original formulations valid for irregular waves, the model showed a fraction of breaking waves along the whole cross-shore profile. But in the case of regular waves, all waves break almost at the same spot near the breaker bar close to the shore. In the model, this is formulated as follows:

$$Q_b = \begin{cases} 0 & \text{for} \quad \frac{H_{\text{rms}}}{h} < \gamma \\ 1 & \text{for} \quad \frac{H_{\text{rms}}}{h} \geq \gamma \end{cases} \tag{3.6}$$

After wave breaking, waves may begin shoaling again. Therefore, this criterium is implemented with the following restriction: if $Q_b(x-1) = 1$ and $\frac{H_{\text{rms}}(x)}{h(x)} \leq 0.4$ then $Q_b(x) = 0$. In Figure 3.3 the difference between the original model formulations and the adjusted formulations is shown. In the original model (red), the fraction of breaking waves is more than zero over the whole profile. Resulting in a contribution of the breaking-wave dissipation (3.3) to the energy balance (3.1) over the whole profile. And consequently in a wave height decay over the whole profile, which is not in correspondence with the measurements, see Figure 2.5. In the adjusted model (blue), waves do not break until +210 m from the wave paddle. The wave height is not affected by the breaking-wave dissipation like in the original model. So, the wave height is only affected by the dissipation due to bottom friction. This has consequences for the calibration of the model, see Chapter 4. The waves start breaking at +210 m from the wave paddle. Because of the abrupt change of Q_b from 0 to 1, the wave height should also show a sudden change. After some time, $\frac{H_{\text{rms}}(x)}{h(x)} \leq 0.4$ and wave breaking stops, until $\frac{H_{\text{rms}}}{h} \geq \gamma$, and so on.

Both the dissipation coefficient α and the wave height-to-depth ratio γ are used to calibrate the root-mean-square wave height. An increase in γ will lead to an increase in $H_{\max}$ and eventually an increase in H_{rms}.

The wave dissipation D_f due to bottom friction, which is the second dissipation term in Equation (3.1), is defined as

$$D_f = \frac{f_w \rho}{\sqrt{\pi}} u_{\text{orb}}^3 \tag{3.7}$$

where f_w is a user defined friction factor and u_{orb} the amplitude of the wave orbital velocity based on linear wave theory and the root-mean-square wave height. The friction factor f_w influences the amount of wave dissipation due to bottom friction and is used to calibrate the root-mean-square wave height. A decrease of f_w will lead to an increase in the root-mean-square wave height.

The breaking-wave dissipation feeds into the second differential equation, the roller balance equation (according to Nairn et al. (1990)):

$$\frac{\partial}{\partial x}\left(2E_r c \cos\theta\right) = D_w - D_r \tag{3.8}$$
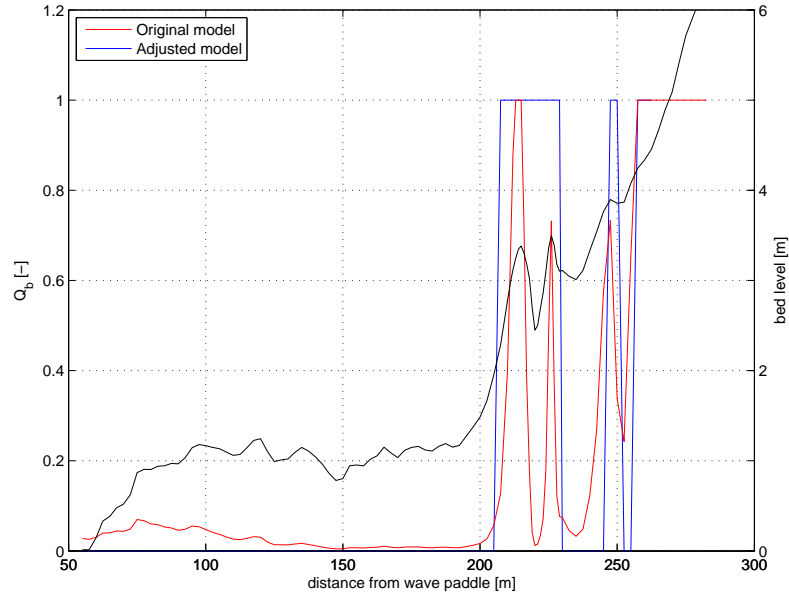
Figure 3.3: Fraction of breaking waves for the original and adjusted model.

where E_r is the roller energy, c is the wave propagation speed and D_r the dissipation of the roller energy. The factor '2' originates from additional dissipation of roller energy due to a net transfer of water from the wave to the roller (Stive and Vriend, 1994). The roller energy E_r represents the amount of kinetic energy in a roller with area A and length L, and is defined as:

$$E_r = \frac{1}{2}\rho c^2 \frac{A}{L} \tag{3.9}$$

The roller energy balance is concluded by modeling the dissipation of roller energy D_r as the power unit length performed by the shear stress between roller and water surface:

$$D_r = \frac{2gE_r \sin\beta}{c} \tag{3.10}$$

where β is the slope of the face of the wave (normally in the range of 0.05 - 0.10) and A is written in terms of E_r from Equation (3.9).

The third differential equation is the cross-shore momentum equation or set-up equation:

$$\frac{\partial\overline{\eta}}{\partial x} = -\frac{1}{\rho g h}\frac{\partial S_{xx}}{\partial x} \tag{3.11}$$

where $\overline{\eta}$ is the mean wave set-up, $h = \overline{\eta} - z_b$ the local water depth and S_{xx} the cross-shore radiation stress, defined as:

$$S_{xx} = \left(\left(n + n\cos^2\theta - 0.5\right)E + 2E_r\cos^2\theta\right) \tag{3.12}$$

with $n = c_g/c$ the ratio between wave propagation speed and the group velocity. With $\theta = 0$, in the case of the experiments, Equation (3.12) reduces to:

$$S_{xx} = \left(\left(2n - 0.5\right)E + 2E_r\right) \tag{3.13}$$

3.4 Mean current profile

The vertical distribution of the alongshore and cross-shore mean current is determined by solving the horizontal momentum balance. A quasi-3D model (Roelvink and Reniers, 1994) is used
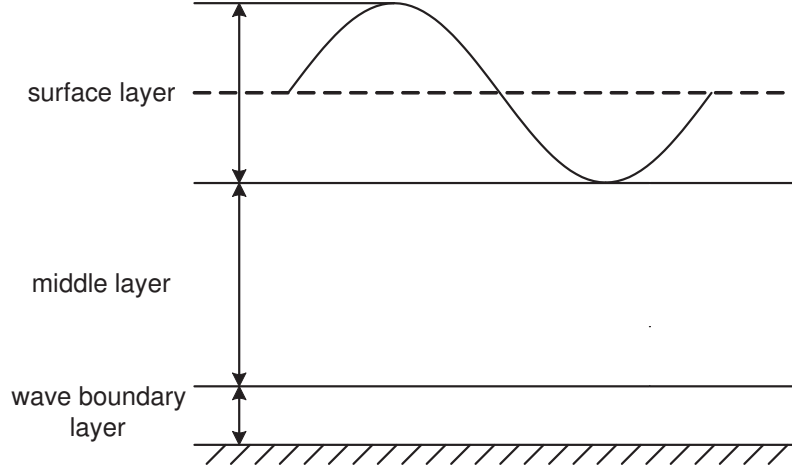
Figure 3.4: Three layers in the mean current profile module.

accounting for the effects of wind shear stress, wave breaking, bottom dissipation in the wave boundary layer and the slope of the free surface. The quasi-3D model identifies three layers (see Figure 3.4):

- a surface layer above the wave trough level;

- a middle layer between the wave trough level and the top of the wave boundary layer;

- and the wave boundary layer itself.

The mean current is calculated according to Reniers et al. (2004), described below. Only the area below the wave trough level is considered. The momentum decay above the trough level is compensated via the effective shear stress at trough level. The mass flux in the surface layer is compensated via the net mean flow below trough level. The modeling of the surface layer is reduced to the formulation of the effective shear stress and the mass flux. The mean current profile below the trough level is determined by the product of the wave-induced mass-flux and the velocity gradients.

3.4.1   Momentum balance

The vertical coordinate is scaled according to:

$$\sigma = \frac{z}{h} \tag{3.14}$$

such that $\sigma = 0$ at the bottom and 1 at the surface. With z the height above the bed and h the water depth. If the advective acceleration terms for the time mean flow are neglected, the momentum balance in x-direction reads:

$$\frac{\partial \tau_x}{\partial \sigma} = \begin{cases} R_x & \text{for} \quad \sigma > \delta \\ R_x + \frac{\partial}{\partial \sigma}\left(\rho \widetilde{u_x}\widetilde{w}\right) & \text{for} \quad \sigma < \delta \end{cases} \tag{3.15}$$

where R_x is the forcing, δ the non-dimensional thickness of the wave boundary layer made dimensionless according to Equation (3.14), and $\widetilde{u}_x$ and $\widetilde{w}$ are the oscillating velocity components in x-direction and vertical direction, respectively.

The non-dimensional thickness of the wave boundary layer is given by:

$$\delta = 0.09 f_\delta \left(\frac{A}{k_s}\right)^{0.82} \frac{k_s}{h} \tag{3.16}$$

with:

$$
\begin{aligned}
\delta_{\max} &= 0.5 \\
\delta_{\min} &= f_\delta \frac{e z_0}{h}
\end{aligned}
\tag{3.17}
$$

where A is the wave orbital excursion parameter near the bed based on the root-mean-square wave height and peak period, f_δ a multiplication factor and $z_0 = k_s/33$ with k_s the Nikuradse roughness which is a free model parameter. A higher value of k_s results in large bed shear stresses and consequently lower velocities, but also an increase in the thickness of the wave boundary layer. In the original model, the factor f_δ was set equal to 20, on the basis of a comparison with measurements of irregular waves. In the case of regular waves, f_δ is set to 1, resulting in the theoretical boundary layer thickness associated with regular waves (Bosboom et al., 2000).

An assumption is made that the forcing R_x is dominated by a pressure gradient and the depth-variation of R_x can be neglected:

$$
R_x = \rho g h \frac{\partial h}{\partial x}
\tag{3.18}
$$

The time-averaged shear stress $-\rho \widetilde{u}_x \widetilde{w}$ in Equation (3.15) results from the fact that in the wave boundary layer the horizontal and vertical velocities are not exactly 90 degrees out of phase. These stresses grow from zero at the bed to an asymptotic value $-\rho(\widetilde{u}_x \widetilde{w})_\delta$ in which, from geometrical considerations $\widetilde{w}(\delta) = -\Delta\tau/\rho c$. Here $\Delta\tau$ is the increase of the instantaneous shear stress through the boundary layer. With the dissipation due to bottom friction given by $D_f = \Delta\tau u(\delta)$ and assuming that the stress $-\rho(\widetilde{u}_x \widetilde{w})$ decreases linearly to zero across the wave boundary layer the last term in Equation (3.15) is given by:

$$
\frac{\partial}{\partial \sigma} \rho \widetilde{u}_x \widetilde{w} = -\frac{1}{\delta} \frac{D_f k_x}{\omega}
\tag{3.19}
$$

where k_x is the wave number in x-direction and ω the angular frequency.

The dissipation due to bottom friction differs from the formulation given by Equation (3.7) by a factor $1/2$, and is computed as follows:

$$
D_f = \frac{1}{2\sqrt{\pi}} \rho f_w u_{\text{orb}}^3
\tag{3.20}
$$

where the friction factor f_w given by the following relation (Soulsby, 1994):

$$
\begin{aligned}
f_w &= 1.39 \left(\frac{A}{z_0} \right)^{-0.52} \\
f_{w,\max} &= 0.3
\end{aligned}
\tag{3.21}
$$

Since the depth-variation of R_x is neglected, the integration of Equation (3.15) from the surface downwards yields:

$$
\tau_x = \tau_s - R_x(1-\sigma)
\tag{3.22}
$$

where $\tau_s = D_r \cos\theta/c$ is the breaking-wave stress at the top of the middle layer. In the bottom layer, boundary layer effects become important. Integrating Equation (3.15) results in:

$$
\tau_x = \tau_s - R_x(1-\sigma) + \frac{D_f \cos\theta}{\omega} \frac{\delta - \sigma}{\delta}
\tag{3.23}
$$

In the absence of breaking waves the third term on the right-hand-side of Equation (3.23) results in an onshore directed current in the bottom boundary layer, known as streaming. Once wave breaking becomes important, the resulting set-up gradient within the surf zone dominates the force balance in the bottom boundary layer, resulting in an offshore directed flow close to the bed.

The shear stress is related to the gradient of the mean horizontal velocity through the turbulent eddy viscosity ν_t:

$$
\tau_x = \frac{\rho \nu_t}{h} \frac{\partial u}{\partial \sigma}
\tag{3.24}
$$

where ν_t is equated to a product of a shape factor ϕ_s and a parabolic shape function (see below).

3.4.2 Vertical structure of eddy viscosity

For the computation of the mean current profile, an eddy viscosity model is used. The eddy viscosity is written as the product of a scale factor $\bar{\nu}_t$ and a shape function ϕ_s. In the middle layer the eddy viscosity is formulated as:

$$\nu_t = \phi_s \bar{\nu}_t \sigma(\sigma_s - \sigma) \quad \text{for} \quad \sigma > \delta \tag{3.25}$$

where $\bar{\nu}_t$ is the depth-averaged turbulent eddy viscosity and σ_s represents the upper limit at which the eddy viscosity is zero. The shape function ϕ_s is given by:

$$\phi_s = \frac{1}{\frac{1}{2}\rho_s - \frac{1}{3}} \tag{3.26}$$

In the wave boundary layer, the eddy viscosity is increased relative to Equation (3.25) to account for the increased turbulence in the boundary layer. This eddy viscosity increase is assumed to have a parabolic distribution throughout the boundary layer and is zero at $\sigma = 0$ and $\sigma = \delta$. This yields for the eddy viscosity distribution in the boundary layer:

$$\nu_t = \phi_s \bar{\nu}_t \sigma(\sigma_s - \sigma) + \phi_b \bar{\nu}_{tb} \sigma(\delta - \sigma) \quad \text{for} \quad \sigma < \delta \tag{3.27}$$

with $\bar{\nu}_{tb}$ the increased turbulence in the wave boundary layer. The shape function ϕ_b depends on the boundary layer thickness via:

$$\phi_b = \frac{6}{\delta^2} \tag{3.28}$$

The definition of the σ-parameters is illustrated in Figure 3.5. The shape of the eddy viscosity in Figure 3.5 strongly depends on the relative magnitudes of δ, σ_s, $\overline{\nu_{tb}}$ and $\overline{\nu_t}$.

Figure 3.5: Vertical structure of the eddy viscosity (Reniers et al., 2004).

3.4.3 Specification of eddy viscosity distribution

Three potential contributions to the turbulent eddy viscosity are considered, viz. wave-breaking-induced turbulence, wind-induced turbulence and flow-generated turbulence. At the measurement location, no breaking waves or wind were present. Only the contribution due to flow-generated turbulence plays a roll and is given by:

$$\bar{\nu}_t = \bar{\nu}_{t,\text{flow}} = \frac{1}{6}\kappa h_t \sqrt{g h_t \left|\frac{\partial \bar{\eta}}{\partial y}\right|} \tag{3.29}$$

where κ is the von Kármán constant, $h_t = h - H_{m0}/2$ the mean water depth minus half the significant wave height, $\overline{\eta}$ the mean water level and g the gravitational acceleration.

From Equation (3.27) it appears that there is a increased turbulence in the wave boundary layer. This turbulence is related to the wave orbital motion and the friction factor. The turbulence in the wave boundary layer is expressed as follows:

$$\overline{\nu}_{tb} = \frac{c_f^2 u_{\mathrm{orb}}^2}{\omega} \tag{3.30}$$

with

$$c_f = \frac{f_w}{2} \tag{3.31}$$

where f_w is determined by 3.21, u_{orb} the orbital velocity based on the root-mean-square wave height and ω the angular frequency corresponding to the peak wave period.

3.5 Near-bed orbital velocity

The model of the time-variation of the near-bed velocity due to non-linear short waves and long waves related to wave groups is based on the concept described in Roelvink and Stive (1989). In the original model, the orbital velocity consists of two parts:

- a contribution due to velocity skewness which is computed using the Rienecker and Fenton (1981) method for monochromatic waves, where the mean wave energy and peak period are used as input for the case of random waves;

- a contribution due to bound long waves based on Sand (1982), and an empirical relationship for the phase of the bound long wave relative to the short wave envelope.

In order to compute the bedload transport rates, a complete representative time-series of the near-bed orbital velocity is required. In the original model, a time-series is produced which has the same characteristics of asymmetry, long waves and amplitude modulation as a random wave field, see the red line in Figure 3.6. In the case of regular waves, the time-series only consists of the near-bed velocity of regular waves (including velocity skewness), based on the Rienecker and Fenton model (blue line in Figure 3.6):

$$U_1(t) = \sum_{j=1}^{n} B_j \cos(j\omega t) \tag{3.32}$$

The amplitudes B_j are determined numerically (Rienecker and Fenton, 1981), such that the difference between the maximum and minimum velocity of the asymmetric waves equals the difference in case of monochromatic waves. Finally the time-averaged velocity at the lowest computational point (at 1 cm above the bed) in the flow model is added to contribute for the mean flow in de wave boundary layer.

3.6 Bed load and suspended sediment transport

The total sediment flux q_{tot} is the sum of the bedload transport q_{bed} and the suspended load transport flux q_{sus}:

$$q_{\mathrm{tot}} = q_{\mathrm{bed}} + q_{\mathrm{sus}} \tag{3.33}$$

Separate transport formulations are used for bedload transport and suspended load transport. In this section both transport modes are described, starting with bedload transport.
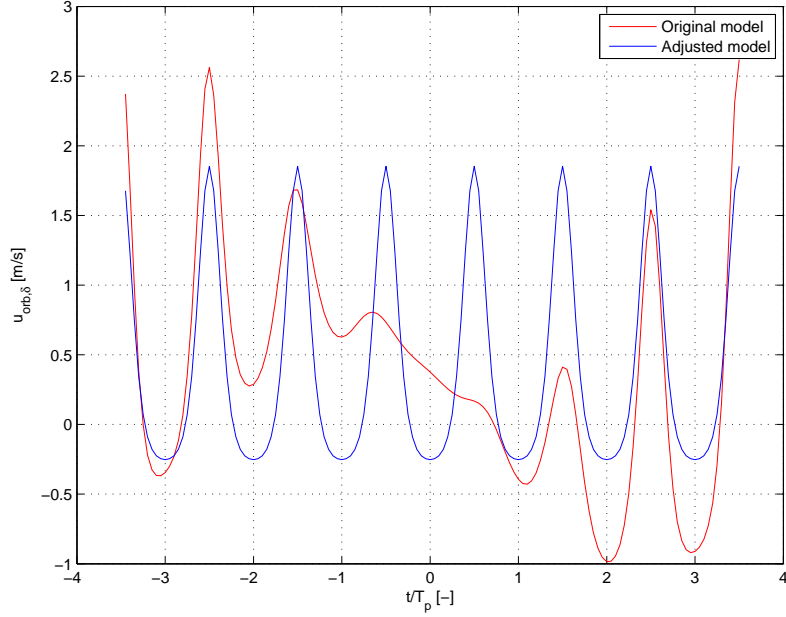
Figure 3.6: Near-bed orbital velocity for the original and adjusted model.

3.6.1   Bedload transport

The bedload transport is computed as a function of the instantaneous bed shear stress. The near-bed velocity signals, which determines the instantaneous bed shear stress, are composed of the generated time-series for the near-bed wave orbital velocity. The bedload transport is calculated according to Ribberink (1998),

$$q_{\text{bed}}(t) = 9.1\beta_s[|\theta'(t)| - \theta_{cr,s}]^{1.8}\frac{\theta'(t)}{|\theta'(t)|}\sqrt{\Delta g D_{50}^3} \tag{3.34}$$

with β_s is the Bagnold parameter, $\theta'(t)$ the instantaneous (intrawave) time series of the dimensionless effective shear stress, $\theta_{cr,s}$ the slope-corrected value of the non-dimensional critical shear stress θ_{cr}, $\Delta = (\rho_s - \rho)/\rho$ the relative density and D_{50} the median grain size.

Bed shear stress

The bedload transport $q_{\text{bed}}(t) = 0$ if $|\theta'(t)| \leq \theta_{cr,s}$. The calculation of $q_{\text{bed}}(t)$ requires the time-average of the instantaneous time series of the dimensionless Shields parameter $\theta'(t)$ due to currents and waves, which is described here as

$$\theta'(t) = \frac{\tau_b(t)}{(\rho_s - \rho)g D_{50}} \tag{3.35}$$

where $\tau_b(t)$ is the time-dependent bed shear stress, ρ_s the sediment density, ρ the density of water, g the gravitational acceleration and D_{50} the median grain size.

For the time-dependent bed shear stress, for the case of combined waves and current, an approach suggested by Grant and Madsen (1979) is used. The bed shear stress is expressed as a quadratic function of the combined wave/current velocity $u_{\text{orb}}(t)$ at some height above the bed (outside the boundary layer):

$$\tau_b(t) = \frac{1}{2}\rho f'_{cw}|u_{\text{orb}}(t)|u_{\text{orb}}(t) \tag{3.36}$$

with f'_{cw} a (skin) friction factor, $u_{\text{orb}}(t)$ the time series of the near-bed intrawave near-bottom horizontal velocity of the combined wave-current motion (see Section 3.5). The wave-current

friction factor f'_{cw} is computed from the (skin) friction factors for waves alone and currents in the presence of waves, weighted linearly with the relative strength of the near-bed net current and oscillatory velocity amplitude:

$$f'_{cw} = \alpha_{cw} f'_c + (1 - \alpha_{cw}) f'_w \tag{3.37}$$

with:

$$\alpha_{cw} = \frac{\langle u_{\text{orb}} \rangle}{\langle u_{\text{orb}} \rangle + \hat{U}} \tag{3.38}$$

in which $\langle u_{\text{orb}} \rangle$ is the time-averaged or mean current near-bed velocity at level z (above the wave boundary layer) and $\hat{U}$ the velocity amplitude of the wave-induced oscillatory flow near the bed (without mean current).

In Equation (3.37) f'_w and f'_c are the wave and current friction factors, respectively. The wave friction factor is assumed to be constant over the wave cycle and is modeled according to Swart (1974):

$$\begin{aligned} f'_w &= \exp\left[-6 + 5.2\left(\frac{\hat{A}_\delta}{k_{s,w}}\right)^{-0.19}\right] \\ f'_{w,\text{max}} &= 0.3 \end{aligned} \tag{3.39}$$

with $\hat{A}_\delta$ the peak value of near-bed orbital excursion according to linear wave theory and based on the significant wave height and peak wave period and $k_{s,w}$ the wave-related bed roughness height. The current friction factor is formulated as follows:

$$f'_c = 0.06 \left[\log \frac{12h}{k_{s,c}}\right]^{-2} \tag{3.40}$$

with $k_{s,c}$ the current-related bed roughness height and h the water depth. Both $k_{s,w}$ and $k_{s,c}$ from Equations (3.39) and (3.40) are formulated as follows:

$$k_s = \begin{cases} 3D_{90} & \text{for} \quad \theta' < 1 \\ 3\theta' D_{90} & \text{for} \quad \theta' > 1 \end{cases} \tag{3.41}$$

with θ' the time-averaged dimensionless effective shear stress, which is also used in the formulation for the time-averaged critical shear stress.

Slope correction to bed load transport rates

The Bagnold parameter from Equation (3.34) is used to account for the transport induced by gravity. The Bagnold parameter increases the transport rates in case of downslope transport and decreases the transport rates in case of upslope transport:

$$\beta_s = \frac{\tan\varphi}{\tan\varphi + \frac{\mathrm{d}z_b}{\mathrm{d}s}} \tag{3.42}$$

where $\tan\varphi$ is the tangent of the angle of repose, which is a free model parameter and is used to calibrate the model in Chapter 4. Upslope transport rates are stimulated by increasing values of $\tan\varphi$, downslope transport hindered. This formulation is only valid for:

$$\left|\frac{\mathrm{d}z_b}{\mathrm{d}s}\right| < \tan\varphi \tag{3.43}$$

Initiation of motion

The parameter θ_{cr} is the non-dimensional critical shear stress, representing the threshold of motion of sand grains. This threshold parameter is calculated according to the classical Shields curve as modeled by Van Rijn (1993) as a function of the non-dimensional grain size D_*.

To account for the effect of bed slope on the initiation of motion, the threshold criterion is corrected using the Schoklitsch factor:

$$\theta_{cr,s} = \frac{\sin\left[\varphi + \arctan\left(\frac{\mathrm{d}z_b}{\mathrm{d}s}\right)\right]}{\sin\varphi}\theta_{cr} \tag{3.44}$$

This formulation results in an increase of the critical shear stress for upslope movement and a decrease of the critical shear stress for downslope movement. The same validity criterion is used as for the slope correction for bed load transport rates (see Equation (3.43)).

3.6.2   Suspended load transport

The suspended sediment transport rate q_{sus} is computed from the vertical distribution of fluid velocities and sediment concentrations, as follows:

$$q_{\mathrm{sus}} = \frac{\int\limits_{a}^{h+\eta} VC\mathrm{d}z}{\rho_s} \tag{3.45}$$

with h the water depth, η the water surface elevation, a the maximum value of the user-defined roughness height, V and C, respectively, the local instantaneous fluid velocity and sediment concentration at height z above the bed. V and C both consist of a time-averaged component (v and c) and a oscillating component ($\tilde{v}$ and $\tilde{c}$). Substituting these components into Equation (3.45) and averaged over space and time yields:

$$\langle q_{\mathrm{sus}}\rangle = \int\limits_{a}^{h} vc\mathrm{d}z + \int\limits_{a}^{h} \overline{\tilde{v}\tilde{c}}\,\mathrm{d}z = \langle q_{\mathrm{sus},c}\rangle + \langle q_{\mathrm{sus},w}\rangle \tag{3.46}$$

with $\langle q_{\mathrm{sus},c}\rangle$ and $\langle q_{\mathrm{sus},w}\rangle$ the time-averaged current-related and wave-related suspended sediment transport rates, respectively. The current-related suspended sediment transport is defined as the transport of sediment particles by the time-averaged (mean) current velocities. The current velocities and the sediment concentrations are affected by the wave motion. It is known that the wave motion reduces the current velocities near the bed and strongly increases the near-bed concentrations due to its stirring action. The wave-related suspended sediment transport is defined as the transport of sediment particles by the oscillating fluid components.

Current-related suspended transport

The time-averaged concentration profile is computed with the time-averaged convection-diffusion equation. This equation reads:

$$w_{s,m}c + \varphi_d\varepsilon_{s,cw}\frac{\mathrm{d}c}{\mathrm{d}z} = 0 \tag{3.47}$$

in which $w_{s,m}$ is the fall velocity of suspended sediment in a fluid-sediment mixture, $\varepsilon_{s,cw}$ is the sediment mixing coefficient for combined current and waves, c is the time-averaged concentration at height z above the bed and φ_d is the damping factor dependent on the concentration. The fall velocity of a sediment particle, the sediment mixing coefficient and the damping factor are computed according to Van Rijn (1993).

In high concentration mixtures, the fall velocity of a single particle is reduced due to the presence of other particles. In order to account for this hindered settling effect, the fall velocity in a fluid-sediment mixture $w_{s,m}$ is determined as a function of the sediment concentration c and the particle fall velocity w_s:

$$w_{s,m} = \left(1 - \frac{c}{\rho_s}\right)^5 w_s \tag{3.48}$$

The particle fall velocity is defined as follows (for $100\mu\text{m} < D_{ss} \leq 1000\mu\text{m}$):

$$w_s = \frac{10\nu}{D_{ss}} \left[\left(1 + \frac{0.01\Delta g D_{ss}^3}{\nu^2} \right)^2 - 1 \right] \tag{3.49}$$

The damping factor φ_d represents the influence of the sediment particles on the turbulence structure of the fluid. This effect becomes increasingly important for high sediment concentrations which result in stratification and consequently damping of turbulence. The following relation is used:

$$\varphi_d = 1 + \left(\frac{c}{c_0} \right)^{0.8} - 2 \left(\frac{c}{c_0} \right)^{0.4} \tag{3.50}$$

with $c_0 = 0.65$ the maximum concentration, which amounts to a maximum concentration of 1.7 10^3 kg/m^3.

For the combined current and wave conditions the sediment mixing coefficient is modeled as follows:

$$\varepsilon_{s,cw} = \sqrt{(\varepsilon_{s,w})^2 + (\varepsilon_{s,c})^2} \tag{3.51}$$

with $\varepsilon_{s,w}$ the wave-related mixing coefficient and $\varepsilon_{s,c}$ the current-related mixing coefficient.

Wave-related mixing coefficient   The mathematical formulation for the wave-related mixing coefficient reads:

$$\varepsilon_{s,w} = \begin{cases} \varepsilon_{s,w,\text{bed}} & \text{for} \quad z \leq \delta_s \\ \varepsilon_{s,w,\text{max}} & \text{for} \quad z \geq 0.5h \\ \varepsilon_{s,w,\text{bed}} + [\varepsilon_{s,w,\text{max}} - \varepsilon_{s,w,\text{bed}}] \left[\frac{z - \delta_s}{0.5h - \delta_s} \right] & \text{for} \quad \delta_s < z < 0.5h \end{cases} \tag{3.52}$$

with δ_s the thickness of the near-bed sediment mixing layer, see Equation (3.16). The mixing coefficient in the near-bed layer is defined as follows:

$$\varepsilon_{s,w,\text{bed}} = \alpha_b \hat{U}_\delta \delta_s \tag{3.53}$$

where $\alpha_b = 0.004 D_*$ and $\hat{U}_\delta$ the peak value of the near-bed orbital velocity. The mixing coefficient in the upper layer reads:

$$\varepsilon_{s,w,\text{max}} = 0.035 \frac{H_s h}{T_p} \tag{3.54}$$

Current-related mixing coefficient   The current-related mixing coefficient is defined as follows:

$$\varepsilon_{s,c} = \begin{cases} \varepsilon_{s,c,\text{max}} - \varepsilon_{s,c,\text{max}} \left(1 - 2\frac{z}{h} \right)^2 & \text{for} \quad z < 0.5h \\ \varepsilon_{s,c,\text{max}} & \text{for} \quad z \geq 0.5h \end{cases} \tag{3.55}$$

with

$$\varepsilon_{s,c,\text{max}} = 0.25\beta\kappa u_{*,c} h \tag{3.56}$$

with β the ratio between sediment and fluid mixing, $\kappa = 0.4$ the constant of Von Karman and $u_{*,c}$ the bed shear velocity, given by:

$$u_{*,c} = \frac{\sqrt{g}}{C} \bar{v} \tag{3.57}$$

with $\bar{v}$ the depth-averaged velocity vector and C the Chézy coefficent.

Reference concentration near the bed

The convection-diffusion equation is solved by numerical integration from the near-bed reference level a to the water surface. At the reference level a a concentration-type boundary condition is used

$$c_a = 0.015 \rho_s \frac{D_{50}}{Z_a} \frac{T^{1.5}}{D_*^{0.5}} \tag{3.58}$$

in which $D_* = D_{50}[(\rho_s/\rho - 1)g/\nu^2]$ (ν is the kinematic viscosity $\approx 10^{-6}$ m/s^2), T is a non-dimensional bed-shear stress parameter and a is the thickness of the bed-load layer. The reference level a is given by the maximum value of the current-related roughness $k_{s,c}$ and the wave-related roughness $k_{s,w}$.

The non-dimensional bed-shear stress parameter T is defined as follows:

$$T = \frac{\tau'_{b,cw} - \tau_{b,cr}}{\tau_{b,cr}} \tag{3.59}$$

with $\tau'_{b,cw}$ the time-averaged effective bed-shear stress and $\tau_{b,cr}$ time-averaged critical bed-shear stress according to Shields, computed as:

$$\tau_{b,cr} = (\rho_s - \rho)g D_{50}\theta_{cr} \tag{3.60}$$

with θ_{cr} according to Equation (3.60).

3.6.3 Wave-related suspended sediment transport

The formulation according to Van Rijn (2000) is used to account for the wave-related suspended sediment transport. It is assumed that the suspended sand concentrations (c) and transport ($q_{s,w}$) response instantaneous to the near-bed orbital velocity. The method was introduced by Houwman and Ruessink (1996) and reads:

$$q_{\text{sus},w} = \gamma \left(\frac{U_{\text{on}}^4 - U_{\text{off}}^4}{U_{\text{on}}^3 + U_{\text{off}}^3} \right) \int_a^b c\,\mathrm{d}z \tag{3.61}$$

with $U_{\text{on}} = U_{\delta,f}$ is the near-bed peak orbital velocity in the wave direction, $U_{\text{off}} = U_{\delta,d}$ is the near-bed peak orbital velocity against the wave direction, $b = 0.5$ m the upper limit for the calculation of the wave-related suspended sediment transport, c the time-averaged concentration and γ a phase lag parameter, which is user defined. The default value is $\gamma = 0.2$, based on flume data from a large scale 2D wave tank.

3.7 Bed level change

After computation of the transport rates along the profile, the bed level changes are computed from the depth-integrated mass balance:

$$\frac{\partial z}{\partial t} + \frac{1}{1 - \varepsilon_p} \frac{\partial q_{\text{tot}}}{\partial x} = 0 \tag{3.62}$$

with q_{tot} the total net sediment transport and $\varepsilon_p = 0.4$ the porosity of the sediment.

3.8 Initial conditions

Before the free model parameters are calibrated some initial conditions are set. These conditions conclude two numerical parameters, the grain size, initial wave height and mean water level.
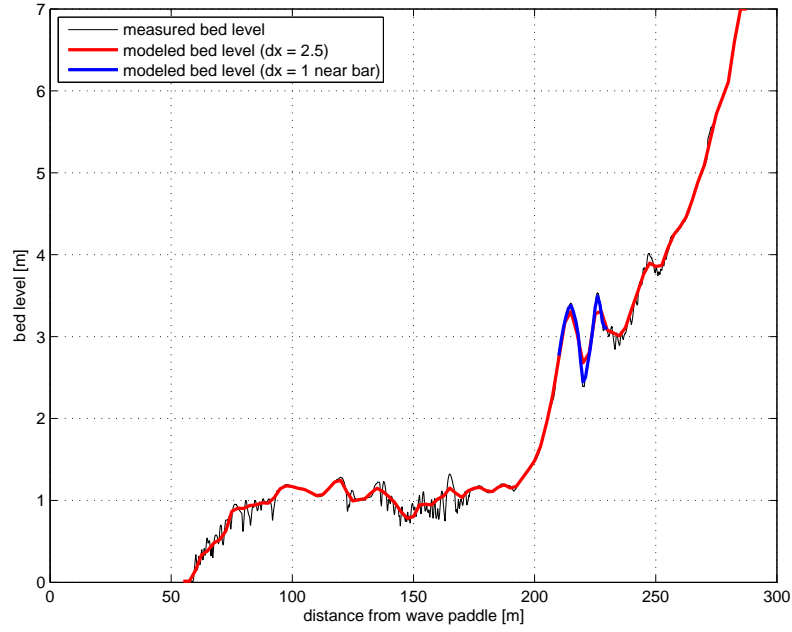
Figure 3.7: Measured and modeled initial bed profile.

3.8.1 Numerical parameters

Grid size The model uses interpolation of a predefined bed profile with a user-defined grid size to determine the initial bed profile. The initial measured bed profile is used as input for the model runs. Walstra (2000) imposes a lower limit for the grid size of $dx \geq 2.5$ m to guarantee numerical stability. The grid size of the complete profile is set to this lower limit. In Figure 3.7 the measured and modeled bed profiles are shown. The mega ripples at the begin of the profile and between +120 m and +170 m are not taken into account by the model. These bed forms are too small for the model to deal with.

The bar system is modeled very roughly with a grid size of $dx = 2.5$ m, indicated by the red line. Because the nearshore bar is one of the parts of great interest, the bar system (between +210 m and +240 m) is modeled with a grid size of $dx = 1.0$ m, indicated by the blue line in Figure 3.7. The model could show numerical instabilities with a grid size less than $dx = 2.5$ m, but after some model runs it appeared that this was not the case.

The range of the bed profiler on the beach was limited to approximately +273 m from the wave paddle. Therefore, the bed level measurements did not start on top of the beach, but a little further seaward. In the model, the bed level landward of this point is extended with an approximation of the average beach slope till +285 m.

Numerical time step The time step is specified in days. The time step is set to the minimum length of an individual experiment of half an hour (= 0.021 days). This does not result in instabilities in the model results.

3.8.2 Other initial conditions

Grain size The median grain size D_{50} during the experiments was measured to be 226 μm. The D_{90} was measured to be 469 μm. The suspended sediment particle size D_{ss} is set to 80% of the median grain size, $D_{ss} = 181$ μm.

Initial wave height   The computed root-mean-square wave height at wave gauge 3 (at +55 m from the wave paddle) is used as the deep water wave height.

Wave period   A constant wave period of 6.5 s is set for all four conditions.

Wave angle   The waves were only directed perpendicular to the coastal profile, so the wave angle is set to 0.

Still water level   During the experiments the still water level was 4.5 m above the horizontal flume bottom. In the model, this is implemented as a fixed tidal elevation (H0) of 4.5 m.

Chapter 4

Model calibration

All modules in UNIBEST-TC, except for the near-bed orbital velocity module, contain free model parameters. The data from the calibration condition (see Chapter 2) is used to find the optimal parameter values. The calibration condition consist of a design wave height of 1.5 m at the wave paddle and 4 individual half hour tests.

The calibration procedure will be as follows. First, the wave propagation module is calibrated. Than, locally at the measurement location, the mean current and concentration profiles are calibrated. The last step is the calibration of the transport module. To quantify the obtained model performance, some statistics are used to quantify the differences between model results and measurements. These statistics are listed in Appendix B. One of the statistics is the Brier Skill Score (BSS). A baseline run is required for this statistic. The baseline run is a model run using the default parameter settings from Unibest-TC. The default settings are listed in Table 4.4, at the end of this chapter.

4.1 Wave propagation

With the adjustments made to the breaking criterium a clear distinction can be made between the area of the flume with and without wave breaking. Therefore, the calibration of the parameters in the wave propagation module is divided into two parts, the part of the flume before and after wave breaking. In the first part, the focus is on the friction factor from the wave propagation module, which is not affected by wave breaking. In the second part, the parameters which influence the wave breaking process are calibrated.

The part of the flume without wave breaking is calibrated using a parameter from Equation (3.7) (see Section 3.3). In this equation f_w is a user defined friction factor, FWEE in the model input. The friction factor f_w influences the amount of wave dissipation due to bottom friction. Consequently, an increase of f_w will lead to a decrease in the (root-mean-square) wave height. Figure 4.1 (a) shows the results from four model runs. According to the applied statistics (see Table 4.1), $f_w = 0.010$ is the optimum value, which is the default value and therefor also used in the baseline run. All other model runs show negative Brill Skill Scores (BSS). The relative mean absolute error (RMAE) for all three model runs do not show large variations. Therefor, FWEE is set to 0, the default value.

Table 4.1: Overview of variation in f_w.

f_w [m]	RMAE [m]	BSS [-]
0.005	0.057	-0.26
0.010	0.058	0
0.020	0.063	-0.68

More model parameters influence the wave height in the breaker zone, mainly the point of breaking and the wave height decay after wave breaking. The statistics from above are not used here because only two wave gauges were situated in this area. A more descriptive analysis of the model performance is used to judge the model results. Therefore, a number of criteria are formulated. First, the wave height results from the experiments showed wave shoaling at wave gauge 18 (+216 m) in three of the four cases. The wave propagation should show wave shoaling at least till wave gauge 18. Wave gauge 19 (+236 m) showed a decrease of wave height for all four conditions. Therefor, wave height decay should be visible between wave gauge 18 and 19.

The point of wave breaking is defined by the dissipation coefficient γ (model input GAMMA). Where, according to Equation (3.6), waves break further onshore with increasing γ. The dissipation coefficient is either constant or varying over the length of the profile. A constant value can be obtained using Battjes and Stive (1985) or with a value manually imposed between 0.6 and 0.8. The varying dissipation coefficient is obtained using Ruessink et al. (2003). Figure 4.1 (b) clearly shows that with $\gamma = 0.8$ wave breaking starts closest to wave gauge 18. With a varying γ-function wave breaking starts further offshore. Shoaling until wave gauge 18 is best modeled with $\gamma = 0.8$, therefore, this value is used. With these parameter setting, the blue lines shows that wave breaking occurs beyond wave gauge 19. Therefore, another dissipation coefficient, α (model input ALFAC), is used for the calibration of the wave propagation. Parameter α from Equation (3.3), accounts for the wave-breaking dissipation in both the energy balance (3.1) and the roller balance equation (3.9). The best results are obtained with a value of 1.2.

The model contains a breaker delay switch. The idea behind the breaker delay is that waves need a distance in the order of one (or more) wave length to actually start or stop breaking. When the breaker delay is switched on, the number of wave lengths and a power in a weight function are parameters to calibrate the wave height in the breaker zone. In the present study, the breaker delay is not switched on. The reason for this is that when the fraction of breaking waves abrupt sets to 1 when $H_{\mathrm{rms}}/h \geq \gamma$, the breaker delay also suddenly switches on. This results in a sudden decay of the wave height at the beginning of the breaker zone, even without shoaling. Besides, Walstra et al. (2001) concludes that the breaker delay is not very robust and should be applied with care. With the absence of a substantial amount of wave gauges in this area, the breaker delay is not used for model calibration purposes.

4.2 Mean current profile

In comparison with the original model, the mean current profile module is changed with respect to the thickness of the boundary layer formulation. Parameter f_δ in Equation (3.16) is now a free model parameter (FACDEL) and is set to 1 for the case of regular waves. The mean current profile module is calibrated using the roughness height k_s, RKVAL in the model input. The roughness height affects both the thickness of the non-dimensional wave boundary layer, through Equation (3.16), and the dissipation due to bottom friction, through Equation (3.20). Equation (3.16) shows that the thickness of the wave boundary layer increases with increasing k_s. In the bottom friction dissipation term, the roughness height affects the friction factor f_w. With increasing k_s, both the friction factor and the dissipation term increases.

In the absence of breaking waves, as was the case near the measurement frame, increasing dissipation due to bottom friction results in less streaming near the bed. But on the other hand,
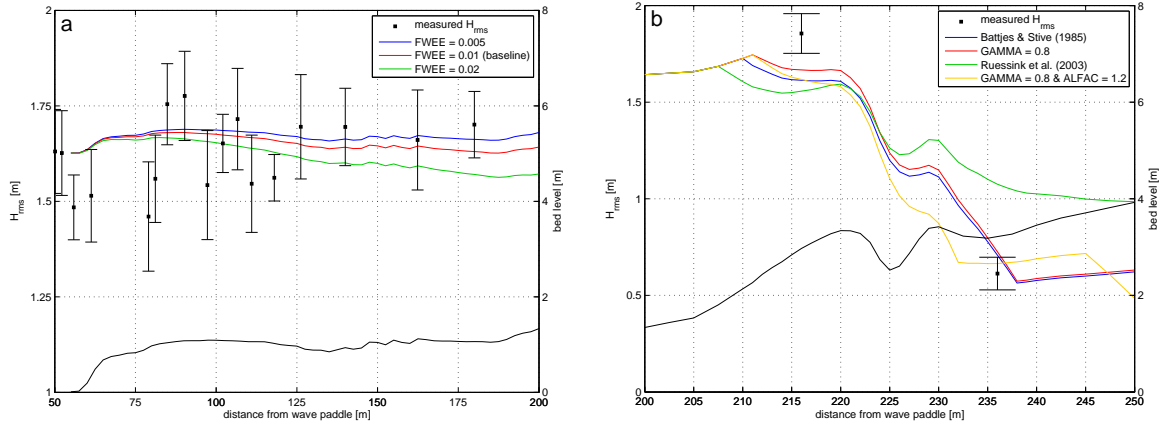
Figure 4.1: Optimization of model parameter: (a) friction factor f_w (FWEE) and (b) wave height-to-depth ratio γ (GAMMA).

the increased thickness of the wave boundary layer results in thicker layer where the streaming appears in the vertical. This could be compensated by a decrease of parameter f_δ, which results in a decrease of the thickness of the wave boundary layer. Although from the literature it appeared that there is a lower limit of 1 for f_δ (Walstra, 2000), the mean current profile is calibrated with lower values for parameter f_δ, to get the best model results. The corresponding thickness of the wave boundary layer is also calculated by multiplying the non-dimensional thickness with the modeled water depth at the measurement location.

Table 4.2: Overview of variation in k_s, f_δ and corresponding δ.

k_s [m]	f_δ [-]	δ [mm]	RMAE [m/s]	RMSE [m/s]
0.01	1	48.1	1.60	0.24
0.05	1	64.3	0.88	0.13
0.1	1	72.8	0.69	0.10
0.2	1	82.5	0.56	0.083
0.2	0.8	66.0	0.46	0.064
0.2	0.6	49.5	0.37	0.050
0.2	0.47	38.8	0.31	0.044

In Figure 4.2 both variations in k_s and f_δ are shown. Figure (a) shows that with increasing k_s, the onshore directed streaming near the bed decreases. Parameter k_s is set to the maximum value (0.2), the values for the RMAE and root-mean-square error (RMSE) are closest to 0 for this value (see Table 4.2). Figure (b) shows the effect of the decrease of parameter f_δ, which results in a decrease of the thickness of the boundary layer. In accordance with the description above, the decrease of the thickness of the wave boundary layer results in less streaming which agrees with the measurements. A low value of both the RMAE and RMSE is obtained with $f_\delta = 0.47$ (Table 4.2). The corresponding thickness of the wave boundary layer is 38.8 mm. Which is still of the right order of magnitude compared to findings by Schretlen et al. (accepted).

The depth-averaged turbulence viscosity generated by wave breaking contains a viscosity coefficient α_w (model input FCVISC). This coefficient does only affect the mean current profile in the breaker zone. Walstra et al. (2001) showed that a value of 0.15 gives the best results for both undertow and transport rates for LIP-11D experiments. On these findings, the value for α_w is set to 0.15 instead of 0.10.
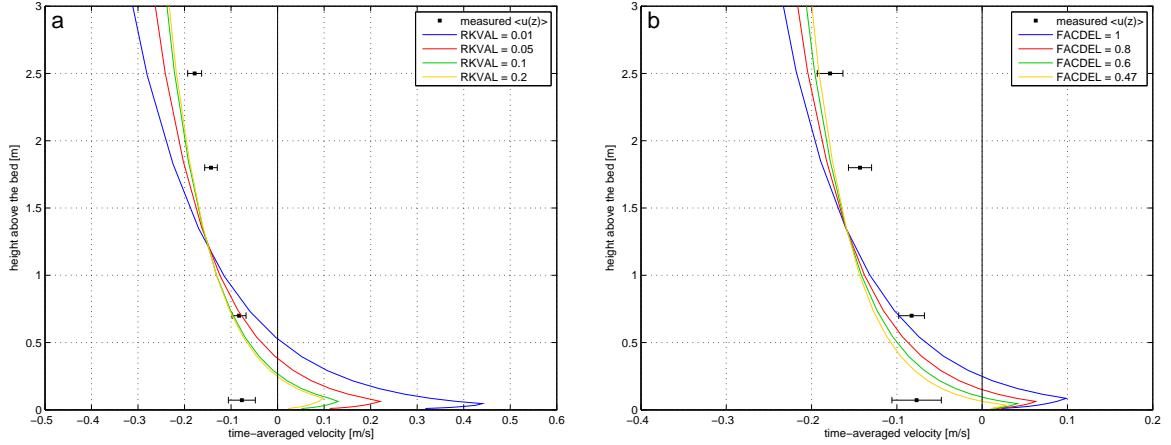
Figure 4.2: Optimization of model parameter: (a) roughness height k_s (RKVAL) and (b) multiplication factor f_δ (FACDEL).

4.3   Mean concentration profile

The mean concentration profile is calibrated using both the roughness height and the diameter of the suspended sediment. The diameter of the suspended sediment D_{ss} (model input DSS) affects the concentration profile through the particle fall velocity w_s, see Equation (3.49). The particle fall velocity decreases with increasing D_{ss}, this results in a larger concentration decay length r_c (see Equation (2.11)), and hence a less steeper concentration profile on log-linear scale. In Figure 4.3 the blue line is the mean concentration profile using $D_{ss} = 0.8D_{50}$, the red line is modeled with $D_{ss} = D_{50}$. The figure shows that the red line show better agreement with the data, which is confirmed by Table 4.3, with both lower values for RMAE and RMSE. Therefore, the mean concentration profile is further calibrated using $D_{ss} = D_{50}$.

The second part of the calibration of the mean concentration profile focusses on the formulation of the reference concentration c_a, see Equation (3.58). The reference level a (Equation (3.58)) is given by the maximum value of the current-related roughness $k_{s,c}$ and the wave-related roughness $k_{s,w}$, RC and RW in the model input. An increase in the reference level a leads to a decrease of the reference concentration c_a. This results in a decrease of sediment concentration over the whole vertical. In a graph, the profile shifts to the left. Only the wave-related roughness $k_{s,c}$ is varied during the calibration of the mean concentration profile. Ruessink (2005) concluded that the inclusion of both $k_{s,c}$ and $k_{s,w}$ in the calibration procedure resulted in a ill-posed optimization problem, because strong $k_{s,c}$-$k_{s,w}$ interaction. A value of 0.015 for $k_{s,c}$ gives the best results, with the lowest value for RMAE and RMSE, see Table 4.3 and Figure 4.3.

Table 4.3: Overview of variation in $\max(k_{s,c},k_{s,w})$ and D_{ss}.

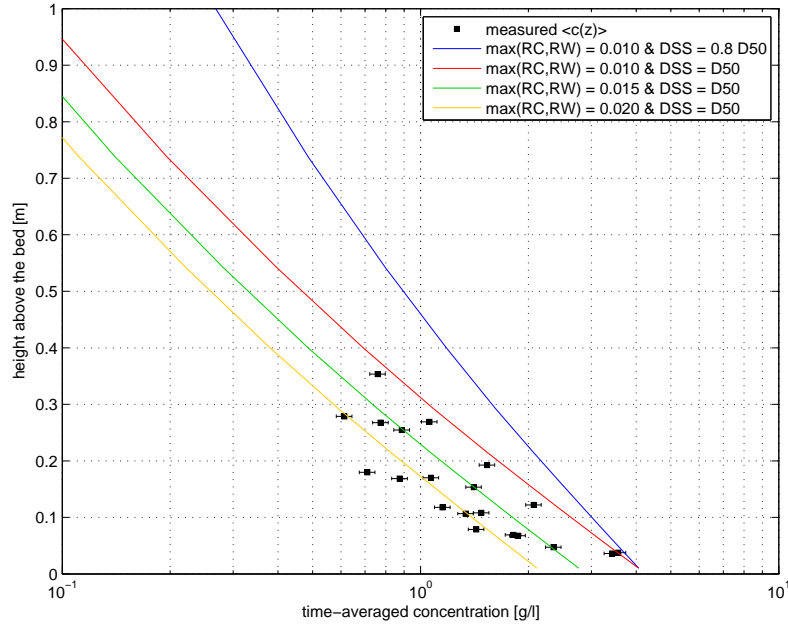| $\max(k_{s,c},k_{s,w})$ [m]	D_{ss} [μm]	RMAE [g/l]	RMSE [g/l]
0.010	181	0.75	1.2
0.010	226	0.48	0.89
0.015	226	0.24	0.46
0.020	226	0.26	0.60

Figure 4.3: Optimization of model parameter $\max(k_{s,c},k_{s,w})$.

4.4 Total sediment transport

The calibration of the sediment transport focusses mainly on the bed load transport module. The assumption is made that with the calibration of the mean current profile and the mean concentration profile the suspended sediment transport is calibrated as well. In the following, attention is paid to the calibration of the bed load transport module.

From the model formulations it appears that the current-related roughness height $k_{s,c}$ also affects the bed load transport rate. However, because the current-related roughness is already used to calibrate the concentration profile, the obtained value is used for the remainder of this study. Another parameter which affects the bedload transport is D_{90}. An increase of D_{90} results in an increase of the bedload transport. Nevertheless, D_{90} is not used to calibrate the bedload transport. There are two reasons for this. First, because of the unreliable measured transports rates. Secondly, D_{90} has to be set to a value far beyond reality to come close to the measured transport rates. Still, one free model parameter is used for calibration purposes here, but this focuses more on irregularities in the bedload transport.

The internal friction angle $\tan\varphi$ (model input TANPHI) affects the bed load transport rates in two ways. The threshold criterion for the initiation of motion is adapted, see Equation (3.44). With increasing $\tan\varphi$ the non-dimensional critical shear stress decreases in case of upslope transport and increases in the case of downslope transport. The bed load transport is also affected through the Bagnold multiplication parameter β_s, see Equation (3.42). In case of upslope transport, β_s increases with increasing $\tan\varphi$ and decreases in downslope transport conditions. Both formulations cause increase of upslope transport and decrease of downslope transport with increasing $\tan\varphi$.

Figure 4.4 shows variation of $\tan\varphi$ between 0.1 and 0.4. A high value of $\tan\varphi$ removes the slope effect from the transport computations. In Figure 4.4 this corresponds to the yellow line, which is much smoother than the other three lines. The blue line corresponds to a low value of $\tan\varphi$. The model seems sensitive for a low value of $\tan\varphi$, there are a lot of large peaked values visible. The largest peak at approximately +160 m from the wave paddle is not shown in the figure to get a better view of the other lines. The parameter is set to a value of 0.3, the green line. This line show the least irregularities compared to the other lines. From earlier calibration studies it appeared that a value between 0.2 and 0.3 is very common for Unibest-TC (Ruessink,
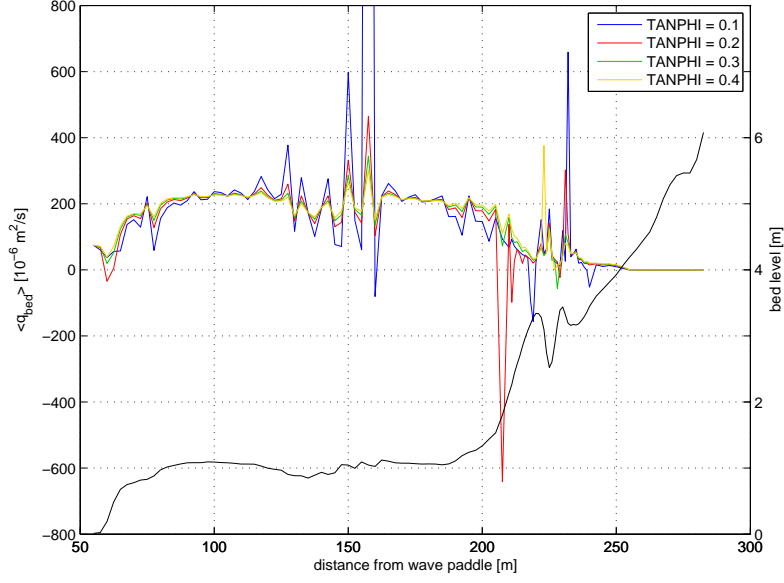
Figure 4.4: Optimization of model parameter $\tan\varphi$.

2005; Ruessink et al., 2007).

4.5 Overview parameter settings

The calibration results in the following parameter settings:

Table 4.4: Overview of parameter settings.

parameters	keyword	range	baseline (default)	parameter optimization
Bottom friction factor	FWEE	0.001–0.1	0.010	0.010
Wave breaking parameter	GAMMA	0.0–0.8	0.0	0.8
Variable γ	VARGAMM	0 or 1	1	0
Factor for wave dissipation	ALFAC	0.6–1.2	1.0	1.2
Breaker delay switch	K_IJL	0 or 1	1	0
Friction factor for mean current	RKVAL	0.0005–0.2	0.01	0.20
Multiplication factor for mean current	FACDEL	0–20	1.0	0.47
Viscosity coefficient	FCVISC	0.05–0.15	0.1	0.15
Grain size of suspended sediment	DSS	0–0.000226	0.000181	0.000226
Current-related roughness	RC	0.0005-0.1	0.01	0.015
Wave-related roughness	RW	0.0005-0.1	0.002	0.002
Internal friction angle	TANPHI	0.02–0.6	0.2	0.3

Chapter 5

Model validation

The optimized values for the free model parameters were determined in the previous chapter. The obtained parameter values are used as input for the validation of UNIBEST-TC. Only the initial wave height at wave gauge 3 (+56 m from the wave paddle) is changed to the measured value for each condition, all other parameters are set to the values of the last column of Table 4.4. The model is validated in the following order: wave propagation, mean current profile, near-bed orbital velocity, mean concentration profile, total sediment transport and morphological changes.

5.1   Wave propagation

To validate the wave height, the measured root-mean-square wave height, as shown in Figure 2.5 is compared with the modeled wave height. In Figure 5.1 the results from the validation of the wave height is shown. A distinction can be made between the wave propagation in the lower and the upper shoreface. In the lower shoreface, the wave height shows hardly any variation. On the other hand, two important phenomena occur in the upper shoreface, wave shoaling and wave breaking. The boundary between the lower and upper shoreface is set to +200 m from the wave paddle, since the wave height measurements showed that 'seaward' of this point no shoaling or wave breaking occurred.

Figure 5.1 shows the wave height along the flume for both the experiments and Unibest-TC. All three conditions show hardly any change in wave height in the lower shoreface, in accordance with the wave height measurements. This corresponds to low values of the relative mean absolute error (RMAE), see Table 5.1. Where a value of 0.068 (condition H07) corresponds to an average difference between modeled and measured wave height of 6.8% of the measured wave height. In the upper shoreface, the shoaling near wave gauge 18 (+216 m) agrees well with the wave height data from condition H07 and H12. The wave shoaling of condition H15 is less pronounced, the same was also concluded from the measured wave height if this condition. The wave height decay between wave gauge 18 and 19 (+236 m) is well modeled for all three conditions, although there were only 2 wave gauges in this area. There is not much information about the real wave height decay in this area. Overall, this results in RMAE values between 0.05 and 0.09 in the upper shoreface. It should be kept in mind that these values are only determined with the use of 2 wave gauges.

Table 5.1: RMAE of the modeled root-mean-square wave height.

Test condition	lower shoreface [-]	upper shoreface [-]	entire profile [-]
H07	0.068	0.055	0.067
H12	0.029	0.094	0.036
H15	0.027	0.057	0.029

From above, it appears that the modeled wave height along the whole length of the flume show good agreement with the wave height measurements. For 2 conditions, shoaling is modeled at the same location is it appeared from the wave height measurements. For condition H15, this point could not be determined from the measurements. Besides, condition H12 and H15 show re-shoaling between wave gauge 18 and 19. This could also not be determined from the measurements. Future measurements should include more wave gauges near the point of shoaling and wave breaking.

5.2 Mean current profile

The main input for the modeled mean current profile is the root-mean-square wave height. To get a reasonable comparison with the measured velocities, the mean current profile is locally validated using the measured wave height at +111 m from the wave paddle.

Figure 5.2 shows both the measured data and modeled results. The figure shows that, like the wave height, the mean current profile agrees well with the data, for all three conditions. The increase of time-averaged velocity with increasing height is well modeled. All conditions show a little overestimation of the mean current for all measurement heights, except for the time-averaged Vectrino signal. At this height, condition H12 shows the best results. The model shows a little underestimation of the mean current velocity at this height for condition H07 and H15.

Table 5.2 shows the relative mean absolute error (RMAE) and the root-mean-square error (RMSE) for the modeled mean current profile. The RMSE shows values between 0.013 and 0.037. This means, e.g. for condition H15, that Unibest-TC over- or underestimates the mean current on the average with 3.4 cm/s. The dimensionless RMAE shows the relative difference between the modeled and measured mean current. With a value of 0.24, a relative difference of 24% on the average measured velocity is modeled by Unibest-TC.

Table 5.2 shows also the thickness of the wave boundary layer, using Equation (3.16), with the multiplication factor from the second column and multiplied by the water depth to make δ dimensional. This results in values between 20 and 39 mm, this corresponds to values found by Schretlen et al. (accepted). Apparently, with $f_\delta < 1$ the modeled thickness of the wave boundary layer still agrees with experimental results.

Table 5.2: RMAE, RMSE and wave boundary layer thickness of the modeled mean current profile.

Test condition	RMAE [-]	RMSE [m/s]	f_δ [-]	δ [mm]
H07	0.38	0.013	0.47	20.4
H12	0.46	0.037	0.47	32.7
H15	0.24	0.034	0.47	38.8

5.3 Near-bed orbital velocity

The near-bed orbital velocity is validated against the time-dependent Vectrino signal at approximately 10 cm above the bed. Like the mean current profile, the orbital velocity is locally validated
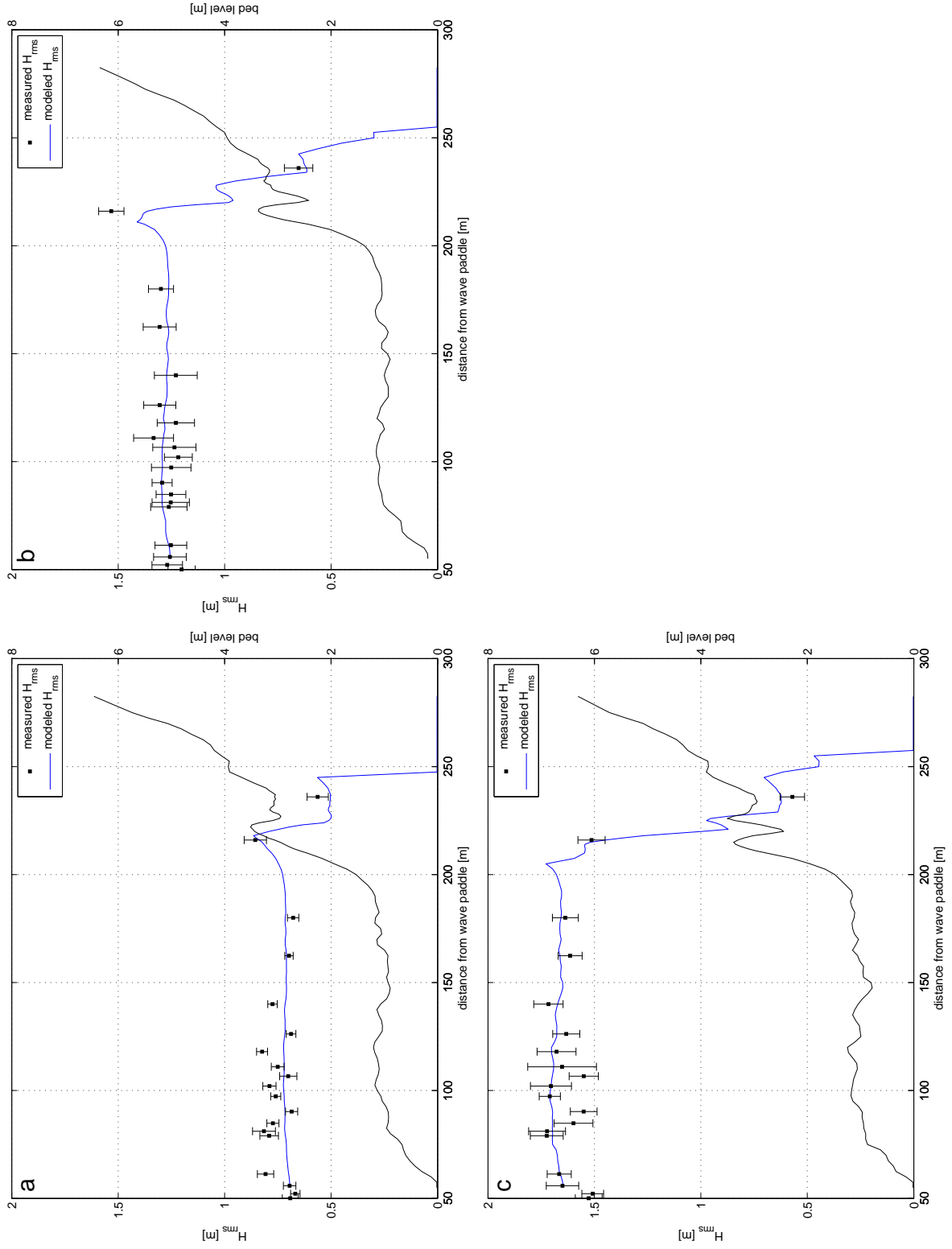
Figure 5.1: Measured and modeled root-mean-square wave height: (a) condition H07, (b) condition H12 and (c) condition H15.
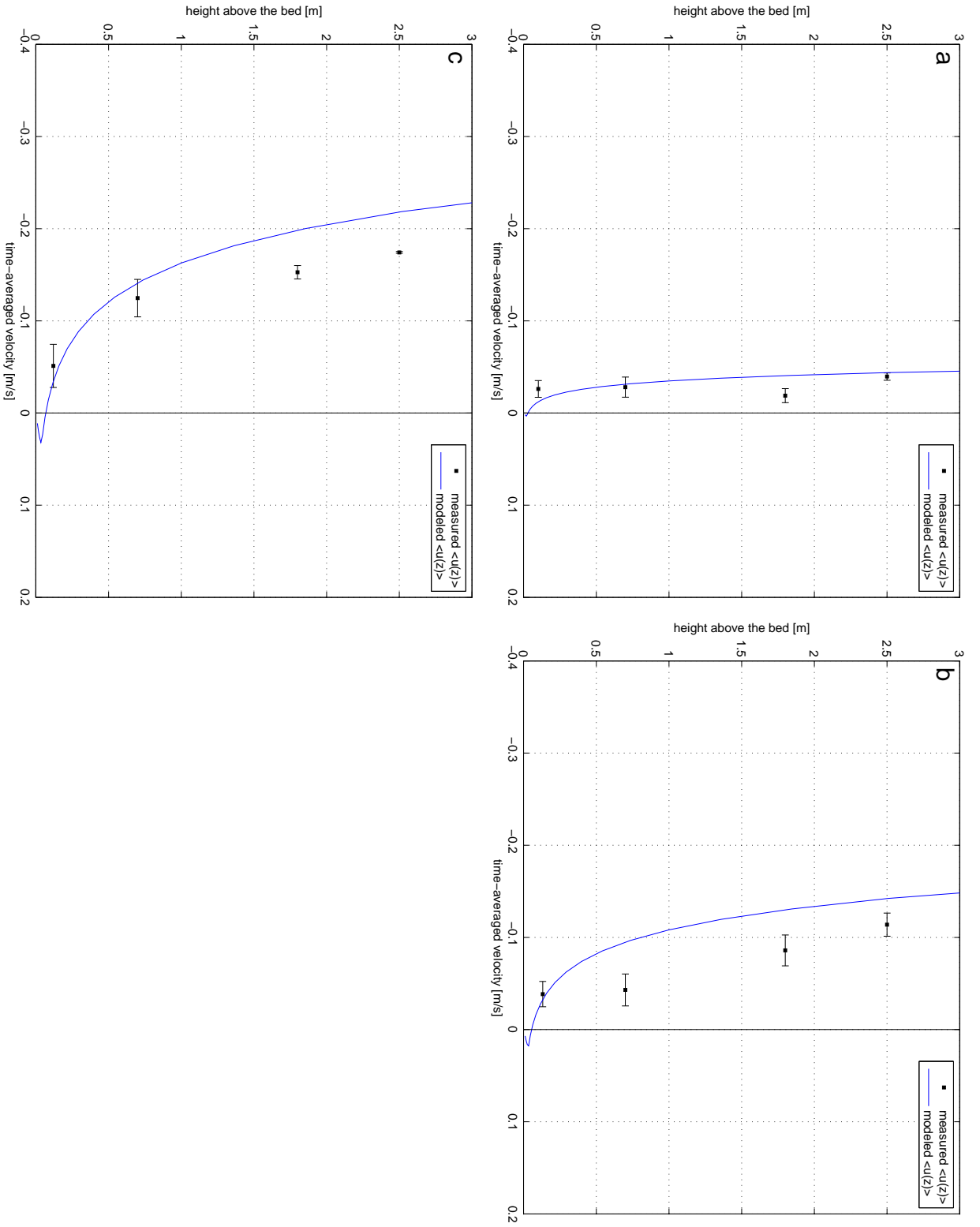
Figure 5.2: Measured and modeled mean current profile: (a) condition H07, (b) condition H12 and (c) condition H15.

using the measured wave height at the measurement frame (at +111 m from the wave paddle). Table 5.3 shows flow velocity characteristics for the modeled near-bed orbital velocity. The same characteristics are determined as shown in Table 2.5 for the measured orbital velocity, with the measured values between the brackets. Besides that, both the modeled and the measured time-dependent orbital velocities are shown in Figure 5.3.

All flow characteristics from Table 5.3 show an increase with increasing wave height. Compared to the measured velocities, the maximum flow velocity $U_{\max}$ of conditions H07 and H15 are similar, whereas condition H12 overestimates the maximum flow velocity. The minimum flow velocity $U_{\min}$ shows the contrary, where Unibest-TC underestimates condition H07 and H15, condition H12 shows a comparable value compared with the measured offshore velocity. The root-mean-square flow velocities U_{rms} are comparable for condition H12 and H15, condition H07 shows an overestimation of U_{rms}. The third-order velocity moment $\langle U^3 \rangle$ is overestimated by all three conditions. The same holds for the degree of orbital flow asymmetry R. This indicates that the model shows more velocity skewness than the measured velocities. The model does not take acceleration skewness into account, all three conditions show a β equal to 0.5.

Table 5.3: Measured and modeled (between brackets) flow velocity characteristics.

Test condition	$U_{\max}$ [m/s]	$U_{\min}$ [m/s]	U_{rms} [m/s]	$\langle U^3 \rangle$ [m³/s³]	R [-]	β [-]
H07	0.65 (0.69)	-0.45 (-0.54)	0.57 (0.42)	0.023 (0.013)	0.59 (0.56)	0.5 (0.47)
H12	1.20 (1.02)	-0.64 (-0.67)	0.64 (0.58)	0.173 (0.070)	0.65 (0.60)	0.5 (0.52)
H15	1.47 (1.39)	-0.69 (-0.84)	0.74 (0.75)	0.327 (0.214)	0.68 (0.62)	0.5 (0.52)

The third-order velocity moment of the modeled near-bed orbital velocity is for all three conditions larger than the measured orbital velocity. It is assumed that a linear relation exists between the third order velocity moment and the net transport rates (Dohmen-Janssen and Hanes, 2002). Later on in this chapter, the same analysis is performed. The modeled transport rates on the lower shoreface are compared with the modeled third-order velocity moments.

5.4 Mean concentration profile

Figure 5.4 shows the measured data and the modeled results of the mean concentration profile. The figures clearly show that the mean concentration profiles do not agree with the measured concentration data. Especially condition H07 and H12 show large deviations from the measured concentration. This is not really emphasized by the RMAE and RMSE. The values found here do not show that the concentration profile of H07 shows the worst prediction compared to the measurements. This is partly because the concentration is presented on a logarithmic scale in Figure 5.4. The mean concentration profile was previously not part of any calibration/validation study with respect to Unibest-TC. Therefore, no statistical parameters were recommended for the mean concentration profile. For future research, it might be useful to use different statistical parameters to compare the concentration profile with experimental data.

Table 5.4: RMAE, RMSE, reference concentration c_0 and concentration decay length r_c of the modeled mean concentration profile.

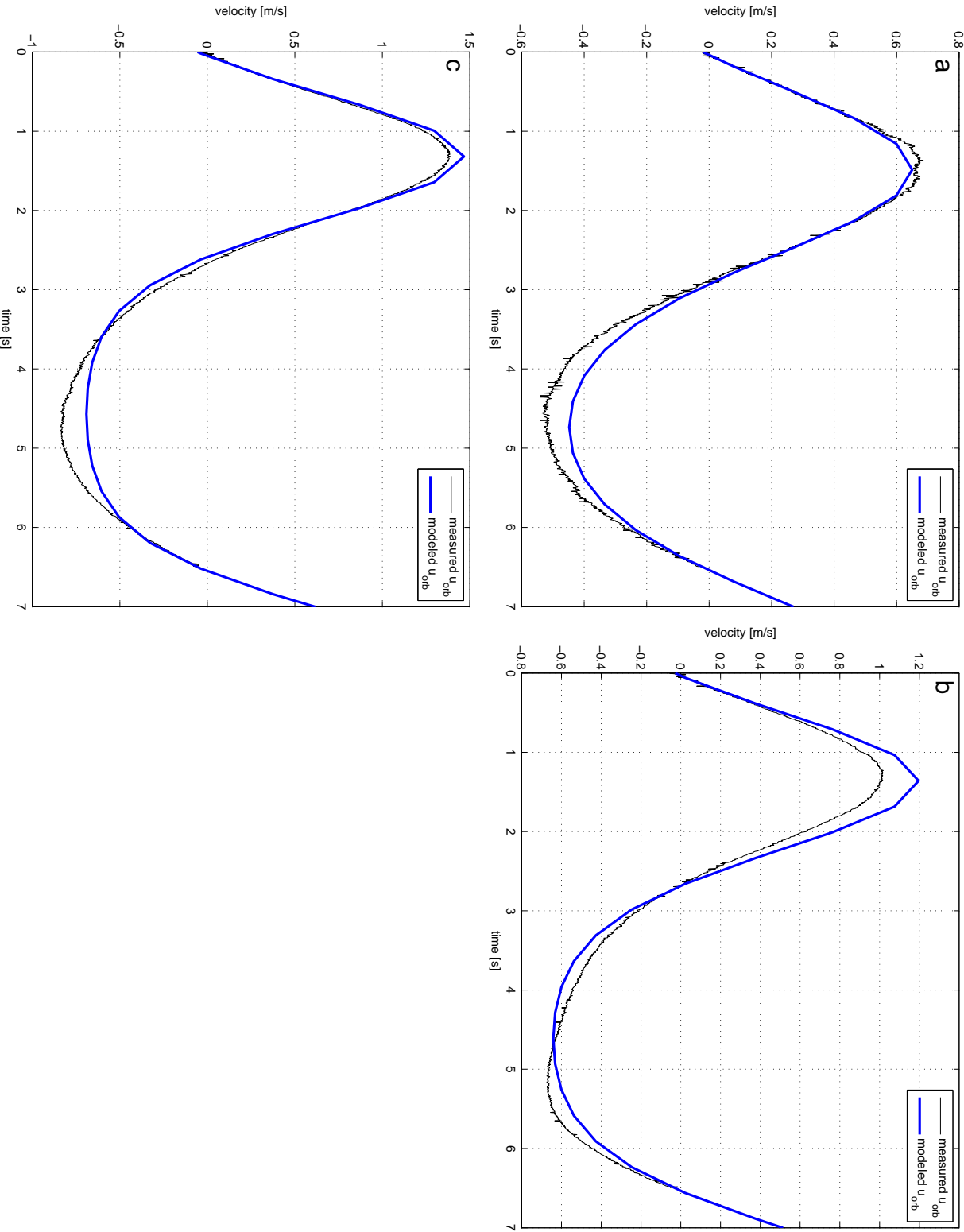| Test condition	RMAE [-]	RMSE [g/l]	c_0 [g/l]	r_c [m]
H07	0.99	1.65	0.09 (6.90)	0.12 (0.13)
H12	0.74	3.61	1.76 (6.04)	0.19 (0.19)
H15	1.29	1.10	3.56 (2.17)	0.23 (0.14)

Figure 5.3: Measured and modeled near-bed orbital velocity: (a) condition H07, (b) condition H12 and (c) condition H15.
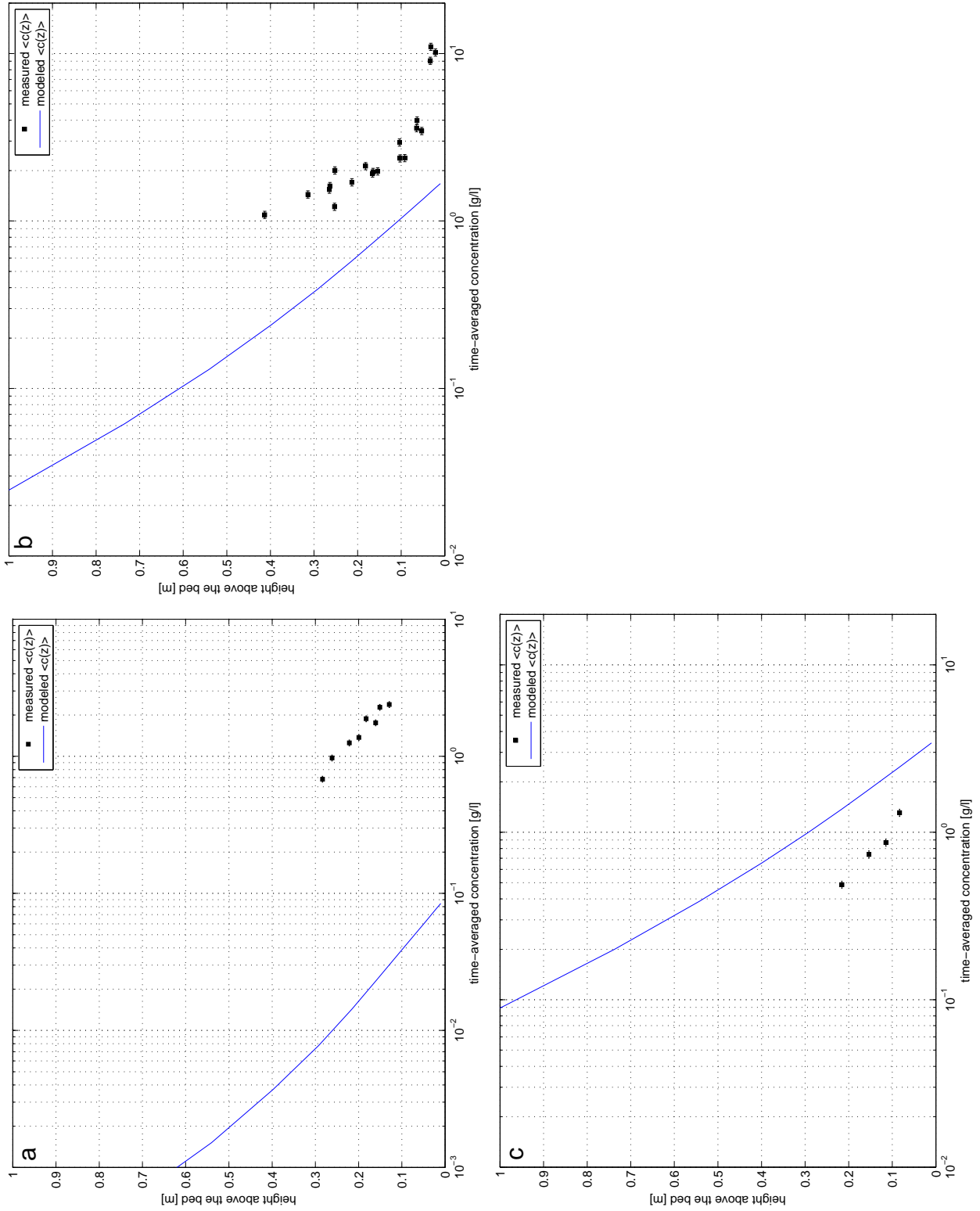
Figure 5.4: Measured and modeled mean concentration profile: (a) condition H07, (b) condition H12 and (c) condition H15.

Table 5.4 shows also the reference concentration c_0 and the concentration decay length r_c. The reference concentration is obtained by extrapolation of the modeled concentration profile to the bed level ($z = 0$ m). The concentration decay length is a measure of the decay over the vertical of the concentration with a factor $\exp(1)$. The values for c_a and r_c obtained from the sediment concentration measurements are also shown in Table 5.4 From both Figure 5.4 and the values of c_0 it appears that the modeled concentration profile is underestimated for condition H07 and H12, and overestimated for condition H15. Especially condition H07 is largely underpredicted, by a factor 75. The concentration decay length r_c shows better agreement with the data, especially for condition H07 and H12. Only condition H15 shows a large difference, remarked that only four concentration measurements were performed during this condition, so the measured r_c is not very reliable. When comparing the r_c of condition H15 with the value found in the measurements of the calibration condition, also with a design wave height of 1.5 m, a comparable value (0.223) is found, see Table 2.7.

5.5   Total sediment transport

Figure 5.5 shows the measured and modeled net transport rates. The modeled transport rates are the average of all modeled transport rates over the duration of the experiments, 4 hours in the case of condition H07 and 2 hours in the case of condition H12 and H15. The figure shows that condition H07 agrees well with the measured transport rates, with approximately the same transport rates both in the lower and upper shoreface. The relative difference between the measured and modeled net transport rates (RBIAS) in the lower shoreface shows a value of 22, see Table 5.5. This is the result of the low value of the measured net transport rate. The absolute averaged difference over the lower shoreface is only 6.38 [10^{-6} m^2/s] (Table 5.6).

For condition H12, the lower shoreface shows also reasonable results, but in the upper shoreface the net transport rates start to increase, up to 4,000 [10^{-6} m^2/s] in the worst case. The same is found for condition H15, where peak transport rates are found of 15,000 [10^{-6} m^2/s]. In the lower shoreface the relative difference is of the order of 8 times the measured transport rates. This corresponds to an absolute overestimation of approximately 230 [10^{-6} m^2/s].

Table 5.5: RBIAS of the modeled total sediment transport.

| Test | RBIAS [-] | | |
condition	lower shoreface	upper shoreface	entire profile
H07	-22.36	0.12	0.46
H12	2.28	-3.95	-0.87
H15	8.13	12.90	-350.93

Table 5.6: BIAS of the modeled total sediment transport.

| Test | BIAS [10^{-6} m^2/s] | | |
condition	lower shoreface	upper shoreface	entire profile
H07	6.38	3.20	4.94
H12	55.64	-137.73	-24.92
H15	229.64	-513.97	-79.62

Figure 5.6 shows the net transport rates in the lower shoreface as a function of the third-order velocity moment. The figure contains also the measured transport rates from the present study and the measured transport rates from Dohmen-Janssen and Hanes (2002), which are both measured in a non-breaker zone. The figure shows that with increasing wave height, the transport
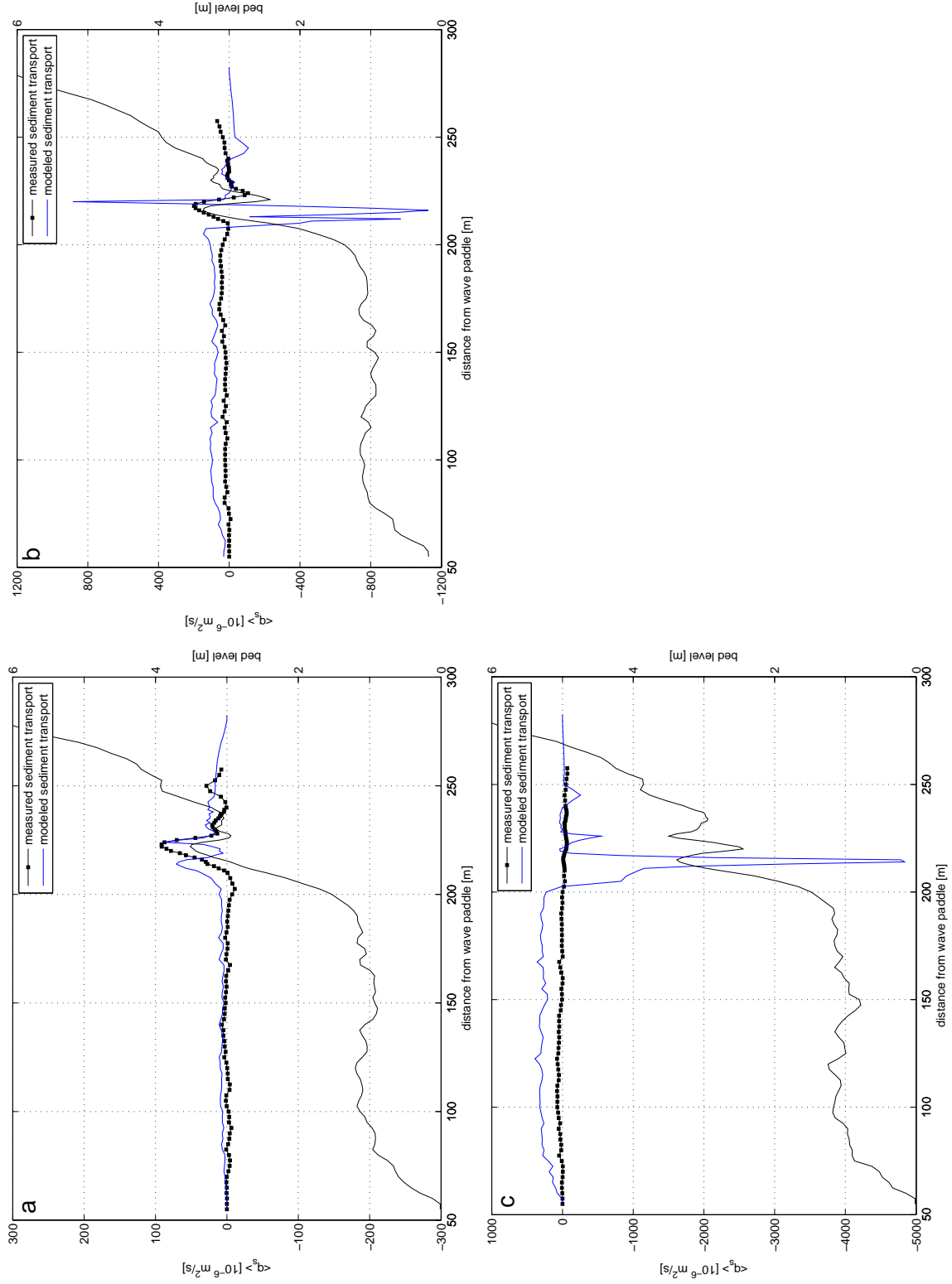
Figure 5.5: Measured and modeled total sediment transport: (a) condition H07, (b) condition H12 and (c) condition H15.

rates tend to deviate more from the proposed linear relationship from Dohmen-Janssen and Hanes (2002). The transport rates found for condition H07 are very low, but fit more or less the linear trendline from Dohmen-Janssen and Hanes (2002). Condition H12 deviates a little more from this line, where condition H15 shows almost a doubling of the net transport rates.
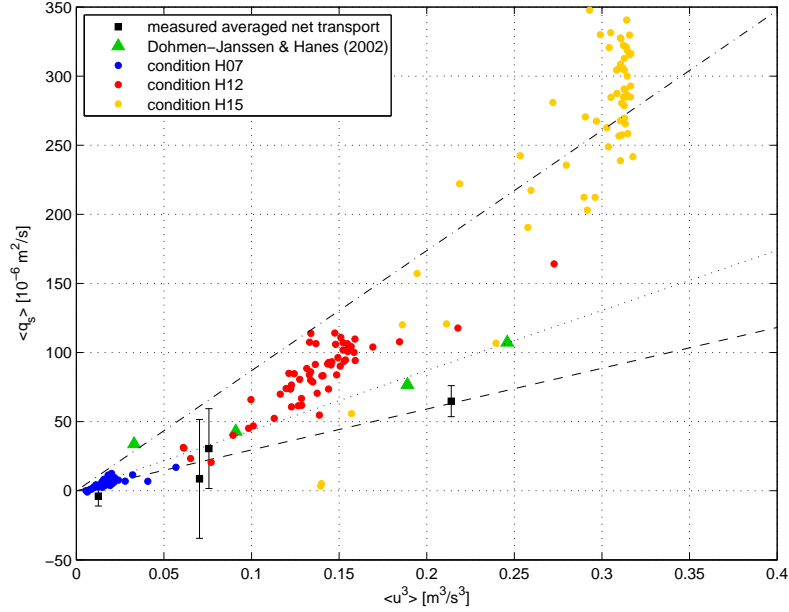

Figure 5.6: Measured and modeled net transport rate as a function of the third-power velocity moment.

Apparently, the net sediment transport might be overpredicted on the lower shoreface, especially with increasing wave heights. Table 5.7 shows the contribution of bedload and suspended sediment transport to the total sediment transport rate at the measurement location, which is on the lower shoreface. With increasing wave height, a larger part of the total sediment transport is contributed by the suspended sediment transport. The underestimation of the mean concentration profile for condition H07 and H12 and the overestimation for condition H15 could be a cause for the differences showed here. Where an underestimation of the mean concentration profile results in less suspended sediment transport, and vice versa.

Table 5.8 shows the contribution of the current- and wave-related suspended sediment transport to the total suspended sediment transport. Current-related suspended sediment transport is for all three conditions offshore directed as a result of the offshore directed undertow from the mean current profile module. The wave-related suspended sediment transport is always onshore directed and larger than the current-related suspended sediment transport. Therefore, the total suspended sediment transport is also onshore directed. In the discussion, more attention is paid to the contribution of the transport components.

Table 5.7: Contribution of bedload and suspended transport to the total sediment transport at the measurement location (+111 m from the wave paddle).

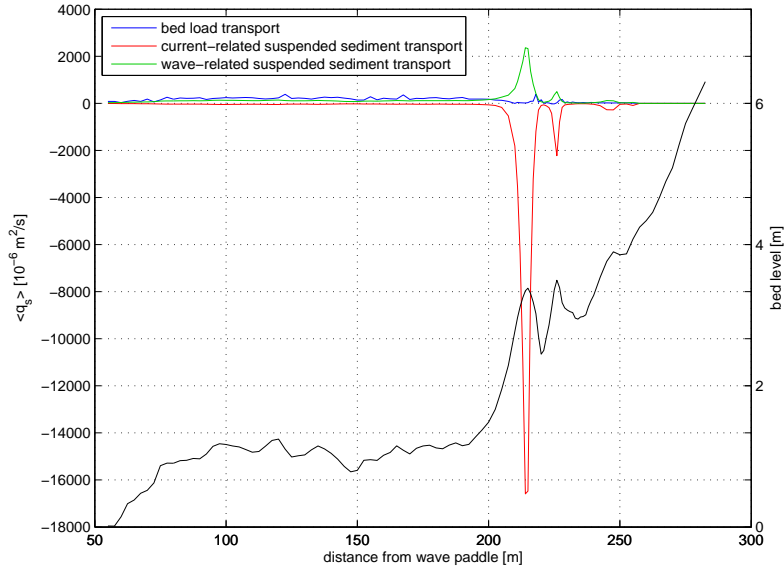| Test condition	q_s $[10^{-6}\ \mathrm{m^2/s}]$	q_{bed} $[10^{-6}\ \mathrm{m^2/s}]$	[%]	q_{sus} $[10^{-6}\ \mathrm{m^2/s}]$	[%]
H07	7.57	7.35	97.2	0.21	2.8
H12	108.74	86.98	80.0	21.76	20.0
H15	312.91	234.57	75.0	78.36	25.0

Figure 5.7: Contribution of bed load, current-related suspended load and wave-related suspended load transport for condition H12.

Table 5.8: Contribution of the current- and wave-related suspended transport to the total suspended sediment transport at the measurement location (+111 m from the wave paddle).

Test condition	q_{sus} $[10^{-6}$ m^2/s]	$q_{\text{sus,c}}$ $[10^{-6}$ m^2/s]	$q_{\text{sus,w}}$ $[10^{-6}$ m^2/s]
H07	0.21	-0.044	0.26
H12	21.76	-6.89	28.65
H15	78.34	-38.36	116.69

When considering the sediment transport over the whole length of the flume, it was already mentioned that Unibest-TC shows large transport peaks near the bar for condition H12 and H15. Figure 5.7 shows the contribution of the bed load, current-related suspended load and wave-related suspended load transport for condition H15, in which the peaks are the most pronounced. From the figure, it becomes clear that the largest part of the negative transport peak near the bar is attributed to the current-related suspended sediment transport. More attention is paid to the causes of these high values of the current-related suspended sediment transport in the discussion.

5.6 Morphological changes

From the previous section, it appeared that the sediment transport near the bar for both condition H12 and H15 shows high peak values near the bar. Figure 5.8 shows the morphological changes of the nearshore bar for all three conditions. Both figure (b) and (c) show large changes of the morphology of the bar system. After 2 hours of modeling, the outer bar in condition H15 is completely disappeared. Condition H12 shows similar results, but not as extreme as condition H15. Figure 5.8 (a) shows the results of condition H07. The figure shows offshore directed bar movement, which is not in line with the measurements, which showed onshore directed bar movement. Apparently, Unibest-TC models negative transport rates on top of the bar, resulting in offshore directed bar movement.
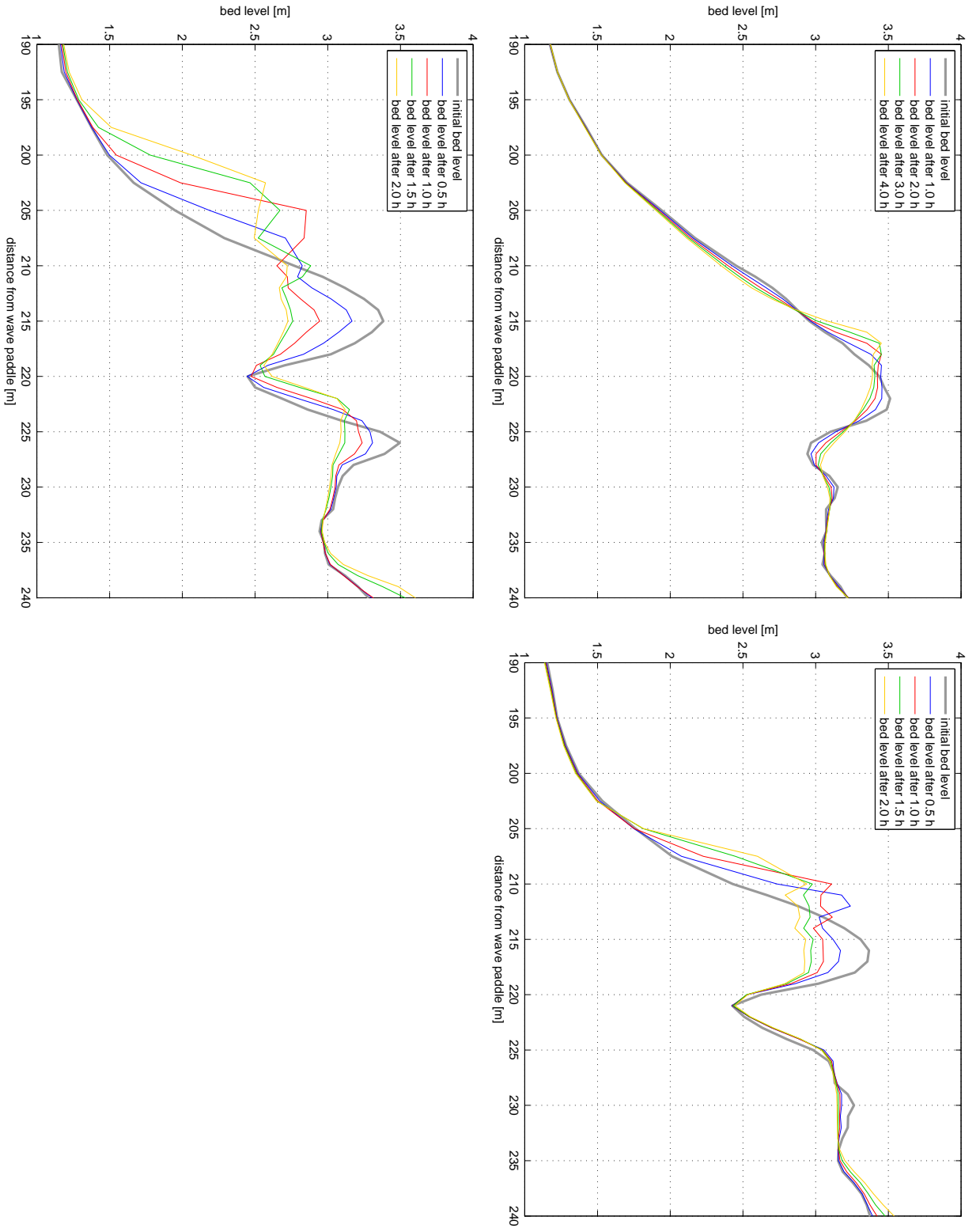
Figure 5.8: Modeled bar migration: (a) condition H07, (b) condition H12 and (c) condition H15.

Chapter 6

Discussion, conclusions and recommendations

6.1 Discussion

6.1.1 Net transport measurements

Both the net transport rates along the profile and the comparison of the net transport rates with the third-order velocity moment show that the transport measurements are uncertain. With the assumption that no sediment leaves the entire profile, the net sediment transport along the profile should begin at 0 and end with 0 net sediment transport. Figure 2.12 shows that this is not the case. Especially conditions H12 and H15 (calibration) show differences at the end of the profile with a maximum of 200 10^6 m^2/s. The comparison between the net transport and the third-order velocity moment shows that at the measurement location the uncertainty is in worst case 5 times the average net transport. From both cases it turns out that the used bed profile measurements are highly unreliable. This makes the comparison of the net transport with the computed transport in Unibest-TC not justified.

The majority of former net sediment transport measurements are performed in oscillatory flow tunnels. From the literature it appears that only once the net sediment transport is measured under full surface waves. Dohmen-Janssen and Hanes (2002) performed experiments under full scale surface waves in the Große Wellenkanal in Hannover, (SISTEX99). The experiments were performed under sheet-flow conditions, where the bed consisted of a test section of approximately 45 m between two concrete structures. Bed level measurements were performed with the use of a Multiple Transducer Array (MTA), which is an array of 32 sonar devices. In contrast with the bed profiler from the present study, the MTA measures the bed level at a height of 0.5 m above the bed, without touching it. Instead of just one bed profile, the MTA measures over a width of approximately 0.45 m. With a vertical resolution of about 2 mm, the bed level measurements are far more reliable than the measurements done with the current bed profiler.

In 2008, new experiments were performed in the Große Wellenkanal in Hannover. During these experiments, a test section with a length of about 70 m was constructed on the flume bottom. Bed level measurements were performed using 4 sonar devices over a large width of the profile. The sonar devices were attached to the movable carriage at a height of about 3.5 m above the bed. The advantage of this method is that variation of the bed over the width of the flume are easily detected. Where the average of the 4 parallel bed levels gives a good representation of the bed level over the whole width of the profile. Net sediment transport calculations of these measurements are not published yet.

Both the in 1999 and in 2008 performed measurements show that it is possible to do bed level measurements much more accurate than the measurements presented here. The only disadvantage of both measurement techniques is that no measurements could be performed outside the water.

Both experiments were performed using a horizontal test section, the profiles did not consisted of a whole shoreface with nearshore bars and a beach. Therefore, the bed level measurements were only performed under the still water level. For future net transport studies with the use of a whole shoreface profile, a method should be developed to deal with changes of the bed level above the still water level.

6.1.2 Model calibration

Mean current profile

The mean current profile module is calibrated using both the roughness height k_s (RKVAL) and the multiplication factor f_δ (FACDEL) from the formulation for the thickness of the wave boundary layer. From the model calibration, it turned out that the roughness height was set to a value of 0.2, which is the upper limit for this free model parameter. From previous studies it appeared that RKVAL is often set to lower values, $k_s < 0.1$ in Reniers et al. (2004) (wave heights $H_{\mathrm{rms}} < 1.2$ m) and $k_s = 0.05$ in Walstra et al. (2001) ($0.6 < H_{\mathrm{rms}} < 1.4$ m). It should be remarked that both studies were performed under irregular wave conditions.

Unibest-TC includes a formulation for the thickness of the wave boundary layer according to Fredsoe and Deigaard (1992). The formulation contains a multiplication factor f_δ, which was previously not a free model parameter in Unibest-TC. Therefore, no comparable studies have been performed in the past using f_δ for calibration purposes. Previously f_δ had a constant value of 20 in Unibest-TC, on the basis of comparison with measurements in irregular wave conditions (Bosboom et al., 2000). Reniers et al. (2004) suggested a value of 3 for irregular waves, but concluded also that proper validation is required with detailed measurements close to the bed. For regular waves f_δ is set to 1 (Fredsoe and Deigaard, 1992). However, from the calibration it appeared that a value lower than 1 (i.e. 0.47) shows better comparison with the velocity measurements.

Although both the roughness height k_s and multiplication factor f_δ are calibrated using extreme values for both parameters, the validation shows that the mean current profile is well modeled by Unibest-TC. Besides, the thickness of the wave boundary layer is of the same order of magnitude as measured in the GWK in 2007 Schretlen et al. (accepted).

Mean concentration profile

The calibration of the mean concentration profile focusses on the current-related roughness $k_{s,c}$ (RC) and the diameter of the suspended sediment D_{ss} (DSS). Previously, the calibration procedure focussed on net transport rates only, where the current-related roughness was one of the main parameters used during the calibration. In the present study, the current-related roughness was used to calibrate the mean concentration profile. Where the current-related roughness $k_{s,c}$ is a free model parameter in the formulation for the reference concentration c_a. A value of 0.015 was obtained during the calibration. Where previous studies show values between 0.03 and 0.08, all obtained during field observations under both storm and mild wave conditions (Reniers et al., 2004; Ruessink, 2005; Ruessink et al., 2007; Van Maanen et al., 2007). The validation showed that with this value, the reference concentration did not agree with the data. Apparently, the reference concentration is very sensitive for varying wave heights.

The diameter of the suspended sediment is also used in the calibration of the mean concentration profile. The concentration profile is affected by the D_{ss} through the particle fall velocity w_s, in which D_{ss} is the only free model parameter. Bosboom et al. (2000) suggests a value of D_{ss} of about 60 to 100% of the median grain size D_{50}. Initially, the diameter of the suspended sediment particles was set to 80% of the median grain size. During the calibration procedure, it appeared that a value equal to the median grain size showed the best agreement with the measured sediment concentrations. Walstra et al. (2001) already showed that DSS can be used to tune the overall transport direction. However, they came up with a value of 3.75 times the median grain size, which is far from reality.

Recently, Van Rijn (2007) suggested a formula for the diameter of the suspended sediment based on the median grain size D_{50} and the mobility parameter Ψ, defined as:

$$D_{ss} = \begin{cases} \left[1 + 0.0006\left(\frac{D_{50}}{D_{10}} - 1\right)(\Psi - 550)\right] D_{50} & \text{for} \quad \Psi < 550 \\ D_{50} & \text{for} \quad \Psi \geq 550 \end{cases} \tag{6.1}$$

where

$$\Psi = \frac{U_{\text{w}}^2 + u_{\text{c}}^2}{(s-1)gD_{50}} \tag{6.2}$$

with U_{w} the peak near-bed orbital velocity, u_{c} the depth average current velocity and $s = \rho_s/\rho_w$ the relative density.

Table 6.1 shows the diameter of the suspended sediment using Equation (6.1), where the peak near-bed orbital velocity U_{w} and the depth average current velocity u_{c} are based on Unibest-TC model runs. The table shows that for both two H15 conditions, the diameter of the suspended sediment is set equal to the median grain size. The other two conditions show smaller grain sizes. It might be interesting to see what happens when this formula is implemented into Unibest-TC, what impact this has on the mean concentration profile and the amount of suspended sediment transport.

Table 6.1: Diameter of suspended sediment based on Equation (6.1).

Test condition	U_{w} [m/s]	u_{c} [m/s]	Ψ [-]	D_{ss} [μm]	D_{ss}/D_{50} [%]
H07	0.62	-0.021	105.7	143	63.2
H12	1.16	-0.074	366.2	192	84.8
H15	1.48	-0.120	599.2	226	100
H15 (calibration)	1.64	-0.155	744.8	226	100

6.1.3 Transport contribution

In Chapter 5 the contribution of the three transport components at the measurement location (+111 m) modeled by Unibest-TC are listed for all three validation conditions. Bedload transport is always positive and accounts for the largest part to the total sediment transport (75-97%). Remarkable enough, the bedload transport contribution decreases with increasing wave height. In the sheet-flow condition (H15) the bedload transport only contributes for 75% to the total sediment transport. Where Dohmen-Janssen and Hanes (2002) showed that under sheet-flow conditions, the contribution of the bedload transport is about 80-90%, where bedload was defined as the sediment transported in the sheet-flow layer. For the ripple condition H07 it appears that the bedload transport contributes for 97% of the total transport. Van der Werf (2006) introduced a suspension parameter, $P = \eta/D_{50}$, with η the ripple height and D_{50} the median grain size. The suspension parameter is derived from tunnel experiments in the rippled bed regime. It is expected that for a large P (corresponding to high ripples and fine sand) suspended sediment transport is dominant, resulting in offshore directed net transport. The ripple profiler data shows, see Figure A.3, ripple heights varying between 0.05 and 0.15 m. With a median grain size of $D_{50} = 226\mu$m, the suspension parameter varies between $220 < P < 664$, which are according to Van der Werf (2006) large values for P. Consequently suspended sediment transport should be dominant here, resulting in offshore directed net transport.

In Unibest-TC the suspended sediment transport is divided into current- and wave-related suspended transport. Where, from the present study, it appeared that the current-related component is always offshore directed and the wave-related component always onshore directed. Both Dohmen-Janssen and Hanes (2002) (full surface wave experiments and sheet-flow conditions) and Van der Werf (2006) (tunnel experiments and rippled bed conditions) showed that the wave-related suspended transport is offshore directed under regular waves. Grasmeijer (2002) measured

net suspended transport rates under irregular wave conditions in a large-scale laboratory flume (Delta-flume), with significant wave heights in the range of 1-1.5 m and two types of sediment beds (160 μm and 330 μm). He concluded that no offshore-directed wave-related suspended sediment transport rates were observed during these tests.

In Unibest-TC, the wave-related component of the suspended transport is always onshore directed, the phase parameter γ is in the default parameter settings set to 0.2. No negative values are obtained with this parameter setting. Van Rijn (2007) introduced a γ-function with inclusion of the phase function proposed by Dohmen-Janssen and Hanes (2002). Where the phase function is defined as:

$$p = (\delta_w) / (T w_s) \tag{6.3}$$

with δ_w the thickness of the wave boundary layer, T the wave period and w_s the particle fall velocity. Van Rijn (2007) modified the phase function so that it can produce negative transport rates in case of a rippled bed. It might be interesting to see what happens with direction of the wave-related suspended sediment concentration if this formula is implemented into Unibest-TC.

6.1.4   Suspended sediment transport

The validation of the total sediment transport showed that high transport rates are found at the nearshore bar for both condition H12 and H15, which do not agree with the measurements. The measured transport rates show a maximum value of approximately 600 10^{-6} m^2/s for all conditions. The high transport rates of 15,000 10^{-6} m^2/s obtained by Unibest-TC with condition H15 are, therefore, far from realistic.

Figure 5.7 shows that the large peak near the bar is for a large part caused by the current-related suspended sediment transport. This contribution to the sediment transport is for a great deal determined by the reference concentration c_a. In the formulation for c_a, the bed-shear stress parameter T consists of both the time-averaged effective current-related and wave-related bed-shear stress, $\tau_{b,c}$ and $\tau_{b,w}$ respectively. Where the first is a function of the depth-averaged velocity and the latter a function of the peak value of the near-bed orbital velocity, which is in the current model formulations based on linear wave theory. The blue line in Figure 6.1 shows the modeled peak value of the near-bed orbital velocity from condition H15, according to the linear wave theory. The figure clearly shows that near the bar, the peak value of the near-bed orbital velocity increases to velocities > 3.0 m/s.

Grasmeijer (2002) (CROSMOR) uses the same expression for the time-averaged effective wave-related bed-shear stress. In CROSMOR the peak value of the near-bed orbital velocity is based on the mean of the on- and offshore near-bed orbital velocity, modeled according to the orbital velocity model of Isobe and Horikawa (1982). The following expression is used in the wave-related bed-shear stress formulation:

$$U_{b,w} = \frac{U_{1/3,on} + U_{1/3,off}}{2} \tag{6.4}$$

where $U_{1/3,on}$ and $U_{1/3,off}$ are the significant on- and offshore peak near-bed orbital velocity respectively.

In Unibest-TC the time-depended near-bed orbital velocity is also determined as a contribution to the bedload transport formulations, based on the non-linear Rienecker and Fenton (1981) model. The peak on- and offshore near-bed orbital velocities are also used in the wave-related suspended sediment transport formulation (U_{on} and U_{off} from Equation (3.61)). With these values, the peak orbital velocity according to Equation (6.4) is easily determined, indicated with the red line in Figure 6.1. The velocities on the lower shoreface show comparable values from both theories. However, the peak orbital velocity near the bar is reduced to approximately 2 m/s. This should result in a reduction of the current-related suspended sediment transport in this region. Implementation of this formula into Unibest-TC could show if this reduction is obtained. During the present study, no velocity measurements were performed near the bar. It might be useful to measure the orbital velocity close to the bed near the bar to verify the suggestion made here.
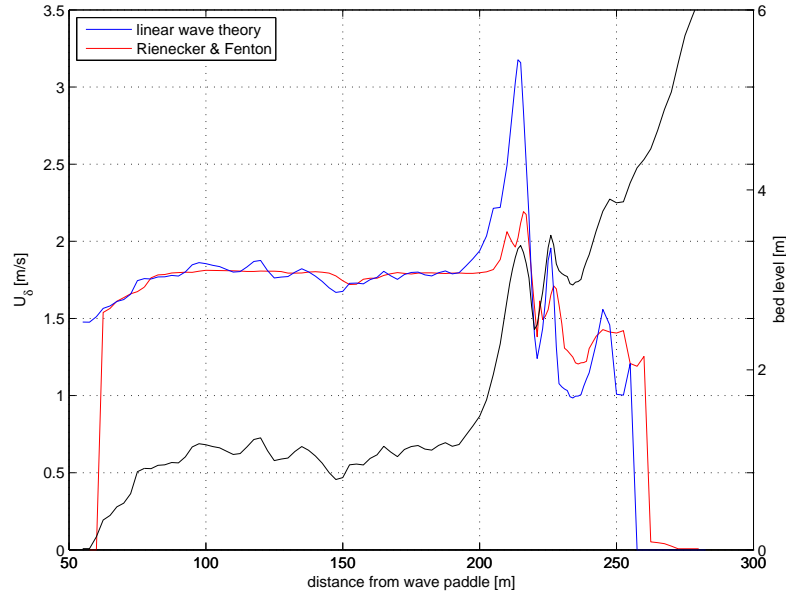
Figure 6.1: Peak orbital velocity based on the linear wave theory and the Rienecker & Fenton theory, for condition H15.

6.2 Conclusions

The aim of the present study was to validate Unibest-TC. The results of the validation are summarized here. Attention is paid to the last two research questions:

What is the behaviour of Unibest-TC compared to the data?

What are the strengths and weaknesses of Unibest-TC?

All hydrodynamic modules show good agreement between Unibest-TC and the experimental data, i.e. the wave propagation module, the mean current profile module and the near-bed orbital velocity module. Adjustments have been made to the wave propagation module. The breaker criterium is changed to account for regular waves. The wave height in the lower shoreface agrees well with the data, for all three conditions. The same holds for the point of shoaling and wave breaking on the upper shoreface, this confirms that the adjustment to the this module are a useful addition to Unibest-TC. The mean current profile and the near-bed orbital velocity are validated locally with the data from the instruments on the measurement frame. Unibest-TC shows a little overestimation of the mean current profile for all conditions, but the shape of the profile agrees well with the data. The third-order velocity moment of the near-bed orbital velocity module is overestimated by Unibest-TC, on the average with a factor 2. This could have consequences for the sediment transport module.

The mean concentration profile is also validated at the measurement location. The reference concentration does not agree with the data, this applies for all three conditions. Condition H07 shows the largest relative deviation from the data, an underestimation of the reference concentration was found of a factor 75. Besides, condition H12 shows also an underestimation, where condition H15 is overestimated by Unibest-TC. Better results are found for the concentration decay length. All conditions show comparable values compared to the data. Nevertheless, the results from the sediment concentration measurements showed that condition H12 and H15 (calibration) are better represented by a power law based formulation for the mean concentration profile. Especially close to the bed the measured sediment concentrations are much higher, this could not be represented by the model.

The validation of the net transport rates show different results for all three conditions. Condition H07 shows the best results, for both the lower and upper shoreface. The net transport on the lower shoreface shows reasonable results for condition H12. The upper shoreface shows very high transport rates near the bar. The same holds for condition H15, where transport rates up to 15,000 10^{-6} m^2/s were found here.

The net transport rates on the lower shoreface are compared with the third-order velocity moment, see Figure 5.6. The modeled results are compared with the measured transport rates from the current study and the transport rates published by Dohmen-Janssen and Hanes (2002). The figure shows that with increasing wave height, the transport rates tend to deviate more from the proposed linear relationship from Dohmen-Janssen and Hanes (2002). The transport rates found for condition H07 are very low, but fit more or less the linear trendline from Dohmen-Janssen and Hanes (2002). Condition H12 deviates a little more from this line, where condition H15 shows almost a doubling of the net transport rates. Verification of the proposed linear relationship between the net sediment transport and the third-order velocity moment with new transport measurements, e.g. the 2008 Hannover measurements, could show if the model really overestimates the net transport on the lower shoreface with increasing wave height.

6.3   Recommendations

The comments from above result in some recommendation for future research. These recommendations are listed below.

- The modeled transport rates deviates from existing relationship between the net transport rates and the third-order velocity moment. The measured transport rates from the present study were far from reliable. Therefore, it is recommended to do the same study using more reliable measured transport rates. This should result in more insight in the relationship between the net transport rates and the third-order velocity moment.

- The calibration procedure and the validation focussed on a measurement location on the lower shoreface. All important hydrodynamic and morphological processes were measured at this location. However, in a morphological sense this region is not very interesting, most of the sediment is transport in the upper shoreface, especially near the bar. Therefore, it is advised to do the same measurements using the same instruments on a measurement frame in the upper shoreface region.

- Above, some ideas are proposed to change some model formulations. I.e. a variable diameter of the suspended sediment, a phase function for the wave-related suspended sediment transport and a formulation of the peak near-bed orbital velocity. It might be interesting to see what effect these changes have on the model performance. Walstra et al. (2001) introduced a testbank of several morphological studies to test Unibest-TC both on field and laboratory data. The proposed formulations could be tested against these data sets. Especially on field data, because those are the conditions the model is made for.

Bibliography

Battjes, J. and Janssen, J. (1978). Energy loss and set-up due to breaking in random waves. In *Proceedings of the 16th International Conference on Coastal Engineering*, pages 569–587. ASCE.

Battjes, J. and Stive, M. (1985). Calibration and verification of a dissipation model for random breaking waves. *Journal of Geophysical Research*, 90(C5):9159–9167.

Bell, P., Thorne, P., and Williams, J. (1998). Acoustic measurements of sand ripple profile evolution under controlled wave conditions. In Alippi, A. and Cannelli, G., editors, *Proceedings of the fourth European Conference on Underwater Acoustics*, pages 353–358. CNR-IDAC.

Bosboom, J., Aarninkhof, S., Reniers, A., Roelvink, J., and Walstra, D. (2000). Unibest-tc 2.0, overview of model formulations. Technical report, WL | Delft Hydraulics.

Bosman, J. and Steetzel, H. (1986). Time- and bed-averaged concentration under waves. In *Proceedings of the 20th ICCE Taipei*, pages 986–1000. ASCE.

Bosman, J., Van der Velden, E., and Hulsbergen, C. (1987). Sediment concentration measurement by transverse suction. *Coastal Engineering*, 11:353–370.

Dette, H., Larson, M., Murphy, J., Newe, J., Reniers, A., and Steetzel, H. (2002). Application of prototype flume tests for beach nourishment assessment. *Coastal Engineering*, 47:137–177.

Dohmen-Janssen, C. and Hanes, D. (2002). Sheet flow dynamics under monochromatic nonbreaking waves. *Journal of Geophysical Research*, 107(C10):13–1–13–21.

Dursthoff, W., Berend, O., and Schmidt-Koppenhagen, R. (1997). Measurement of sand beach profiles in the large wave flume. In *International offshore and polar engineering conference*.

Fredsoe, J. and Deigaard, R. (1992). *Mechanics of Coastal Sediment Transport*. World Scientific, Singapore.

Grant, W. and Madsen, O. (1979). Combined wave and current interaction with a rough bottom. *Journal of Geophysical Research*, 84(C4):1797–1808.

Grasmeijer, B. (2002). *Process-based cross-shore modelling of barred beaches*. PhD thesis, Department of Physical Geography, University of Utrecht.

Hassan, W. and Ribberink, J. (2005). Transport processes of uniform and mixed sands in oscillatory sheet flow. *Coastal Engineering*, 52:745–770.

Hoefel, F. and Elgar, S. (2003). Wave-induced sediment transport and sandbar migration. *Science*, 299(doi:10.1126/science.1081448):1885–1887.

Houwman, K. and Ruessink, B. (1996). Sediment transport in the vicinity of the shoreface nourishment of terschelling. Dep. of Physical Geography, University of Utrecht, The Netherlands.

Isobe, M. and Horikawa, L. (1982). Stody on water particle velocities of shoaling and breaking waves. *Coastal Engineering in Japan*, 25:109–123.

Nairn, R., Roelvink, J., and Southgate, H. (1990). Transition zone width and implications for modelling surfzone hydrodynamics. In *Proceedings of the International Conference on Coastal Engineering*, pages 68–82, Delft, The Netherlands.

Nortek (2004). Vectrino velocimeter, user guide. Technical report, Nortek AS.

O'Donoghue, T., Doucette, J., van der Werf, J., and Ribberink, J. (2006). The dimensions of sand ripples in full-scale oscillatory flows. *Coastal Engineering*, 53:997–1012.

Reniers, A., Thornton, E., Stanton, T., and Roelvink, J. (2004). Vertical flow structure during sandy duck observations and modeling. *Coastal Engineering*, 51:237–260.

Ribberink, J. (1998). Bed-load transport for steady flows and unsteady oscillatory flows. *Coastal Engineering*, 34:59–82.

Ribberink, J. and Al-Salem, A. (1994). Sediment transport in oscillatory boundary layers in case of rippled beds and sheet flow. *Journal of Geophysical Research*, 99(C6):12707–12727.

Rienecker, M. and Fenton, J. (1981). A fourier approximation method for steady water waves. *Journal of Fluid Mechanics*, 104:119–137.

Roelvink, J., Meijer, T., Houwman, K., Bakker, R., and Spanhoff, R. (1995). Field validation and application of a coastal profile model. In *Coastal Dynamics*, pages 818–828.

Roelvink, J. and Reniers, A. (1994). Upgrading of a quasi-3d hydrodynamic model. Technical report, Abstracts-in-depth, MAST G8-M overall workshop.

Roelvink, J. and Stive, M. (1989). Bar-generating cross-shore flow mechanisms on a beach. *Journal of Geophysical Research*, 94(C4):4785–4800.

Roy, P., Cowell, P., Ferland, M., and Thom, B. (1994). *Coastal Evolution: Late Quaternary Shoreline Morphodynamics*, chapter Wave-dominated coasts, pages 121–186. Cambridge Universtity Press, Cambridge.

Ruessink, B. (2005). Predictive uncertainty of a nearshore bed evolution model. *Continental Shelf Research*, 25:1053–1069.

Ruessink, B., Kuriyama, Y., Reniers, A., Roelvink, J., and Walstra, D. (2007). Modeling cross-shore sandbar behavior on the timescale of weeks. *Journal of Geophysical Research*, 112(F3):F03010.

Ruessink, B., Walstra, D., and Southgate, H. (2003). Calibration and verification of a parametric wave model on barred beaches. *Coastal Engineering*, 48:139–149.

Sand, S. (1982). Long wave problems in laboratory models. *Journal of Waterways, Ports, Coastal Oceans Division*, 108:492–503.

Schretlen, J., van der Werf, J., Ribberink, J., Kleinhans, M., Zuijderwijk, W., and O'Donoghue, T. (accepted). New high-resolution measurements of wave boundary layer flow and sand concentrations under full-scale surface waves. In *Proceedings of the 31th ICCE Hamburg*. ASCE.

Smith, J. (1977). *The Sea*, volume Volume 6, chapter Modelling of sediment transport on continental shelves, pages 539–577. Wiley-Interscience, New York.

Soulsby, R. (1994). Manual of marine sands. Technical report, HR Wallingford. Report No. SR 351.

Stive, M. J. F. and Vriend, H. J. D. (1994). Shear stress and mean flow in shoaling and breaking waves. In *Proceedings of the 24th International Conference on Coastal Engineering*, pages 594–608. ASCE, New York.

Swart, D. (1974). Offshore sediment transport and equilibrium beach profiles. Technical report, WL | Delft Hydraulics. Publ. 131.

Van der Werf, J. (2006). *Sand transport over rippled beds in oscillatory flow.* PhD thesis, University of Twente.

Van Maanen, B., de Ruiter, P., Coco, G., Bryan, K., and Ruessink, B. (2007). Onshore sandbar migration at tairua beach (new zealand): Numerical simulations and field measurements. *Marine Geology*, 253:99–106.

Van Rijn, L. (1993). *Principles of sediment transport in rivers, estuaries and coastal seas.* Aqua Publications, Amsterdam.

Van Rijn, L. (2000). General view on sand transport by currents and waves. Technical report, WL | Delft Hydraulics, Delft. Report Z2899.20/Z2099.30/Z2824.30.

Van Rijn, L. (2007). Unified view of sediment transport by currents and waves. ii: Suspended transport. *Journal of Hydraulic Engineering*, 133(6):668–689.

Walstra, D. (2000). Unibest-tc user guide. Technical report, WL | Delft Hydraulics. Report Z2897.

Walstra, D. (2004). *User manual UNIBEST-TC for Windows.* WL | Delft Hydraulics.

Walstra, D. and Steetzel, H. (2003). Description of improvements in the unibest-tc model; upgrade of unibest-tc version 2.04 to 2.10. Technical report, WL | Delft Hydraulics. Report Z3412.

Walstra, D., van Koningsveld, M., Aarninkhof, S., and Ruessink, B. (2001). Methodological approach to model development for unibest-tc. Technical report, WL | Delft Hydraulics. Report Z3147.10.
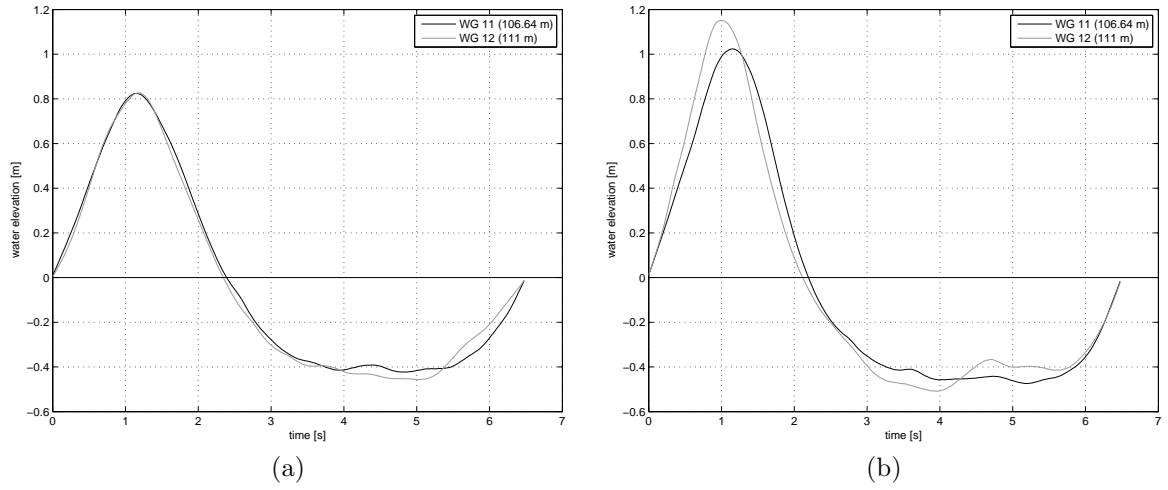
Appendix A

Experimental data

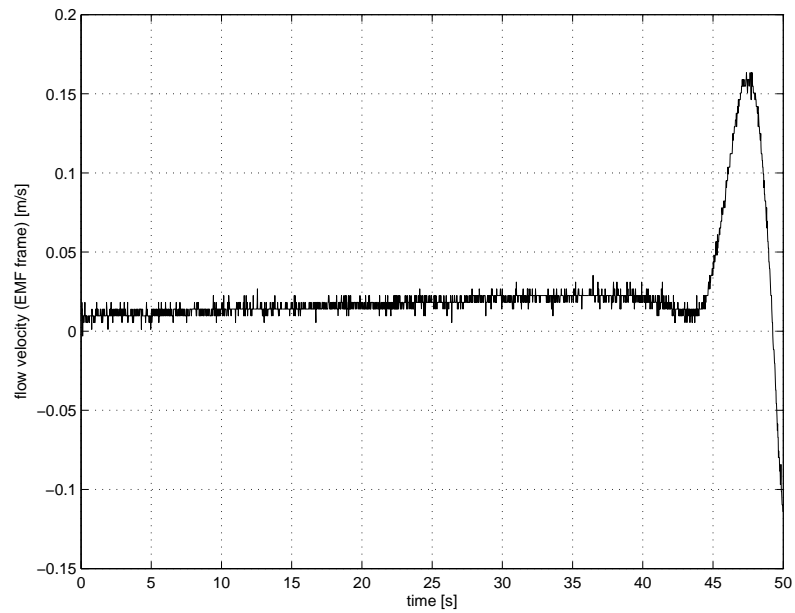**Figure A.1:** Ensemble-averaged water elevation at wave gauge 11 and 12: (a) $H = 1.2$, (b) $H = 1.5$.

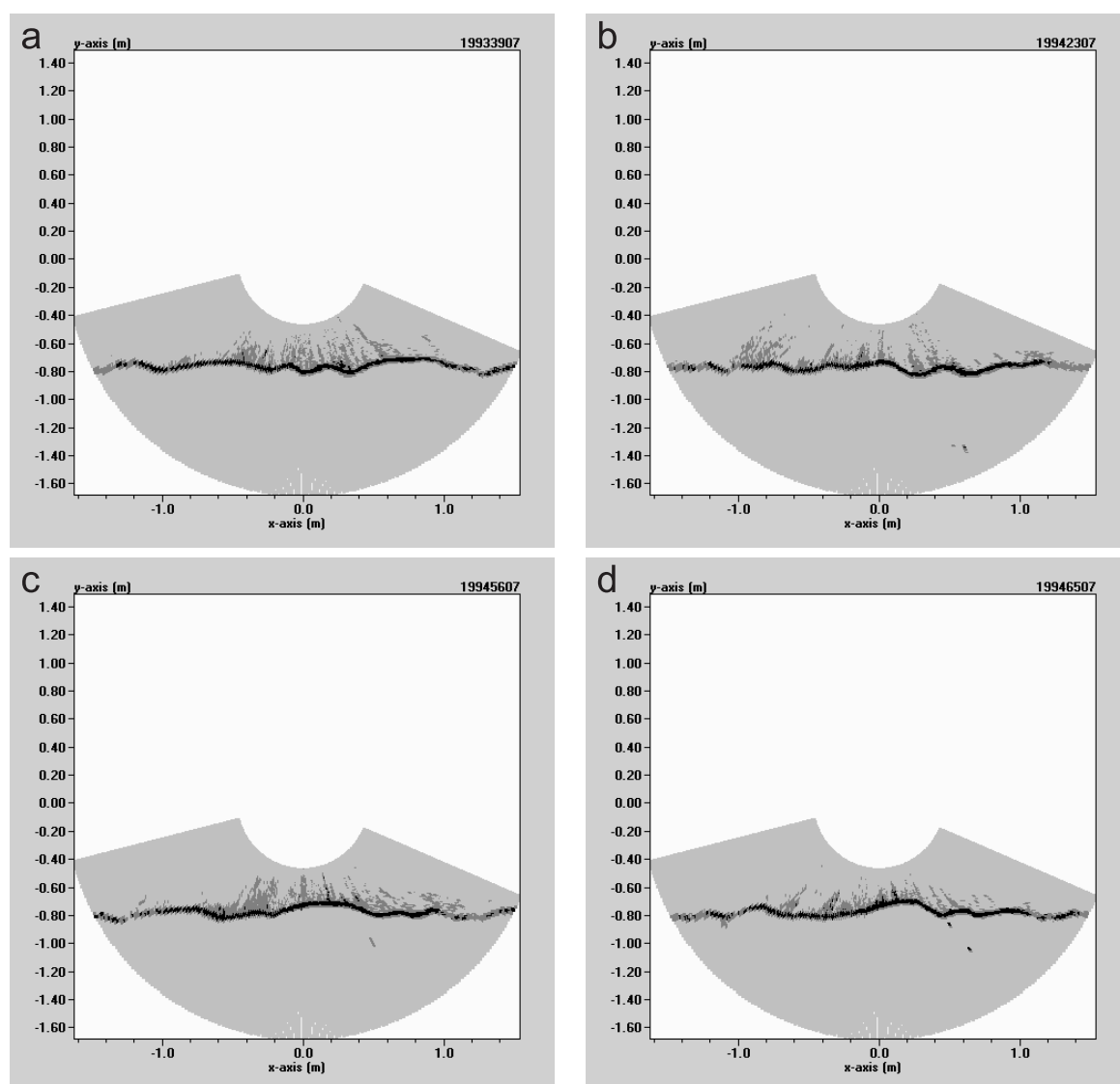**Figure A.2:** Detail of the time-dependent EMF (frame) signal.

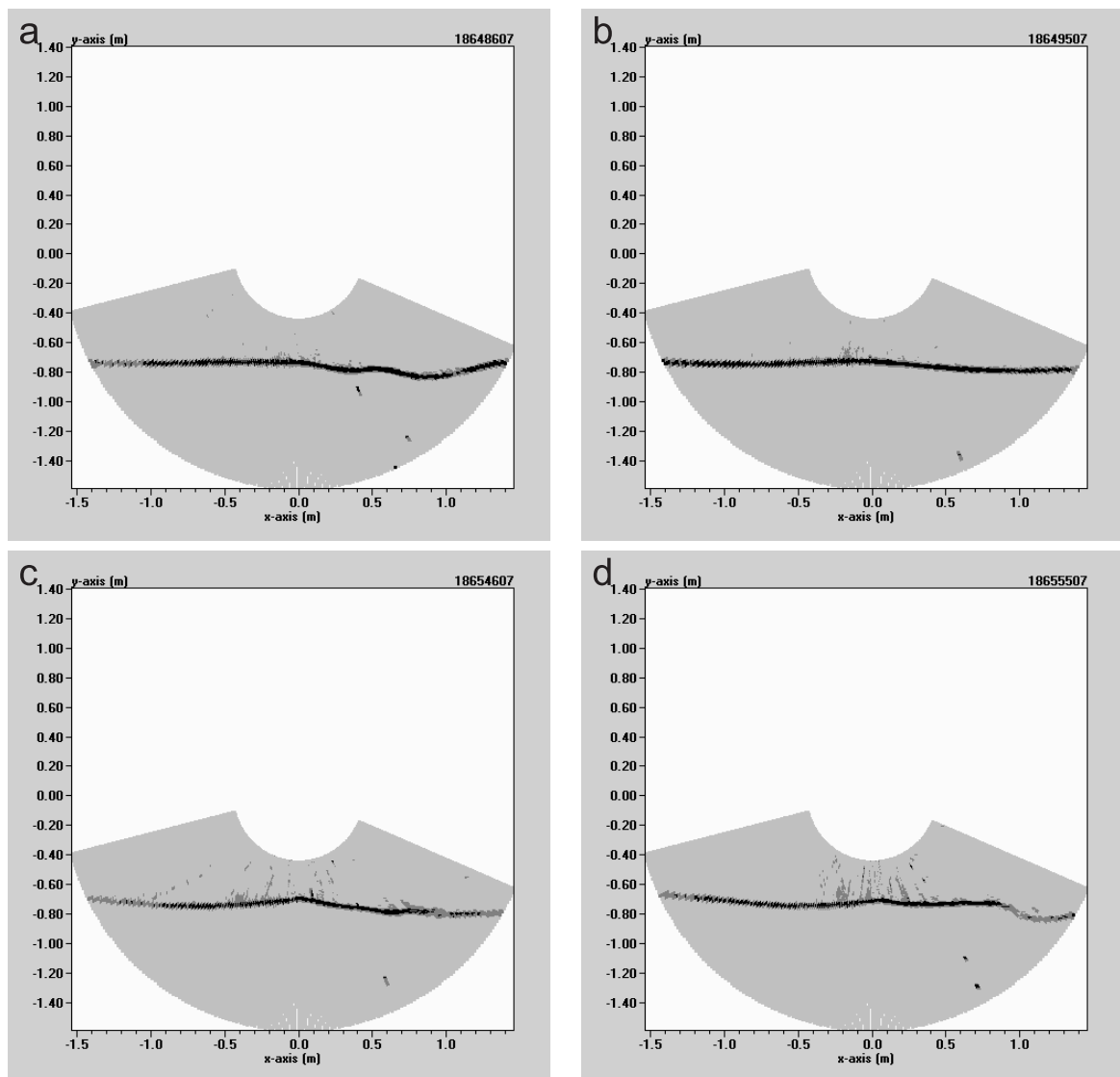**Figure A.3:** Sonar images from the ripple profiler, condition H07.

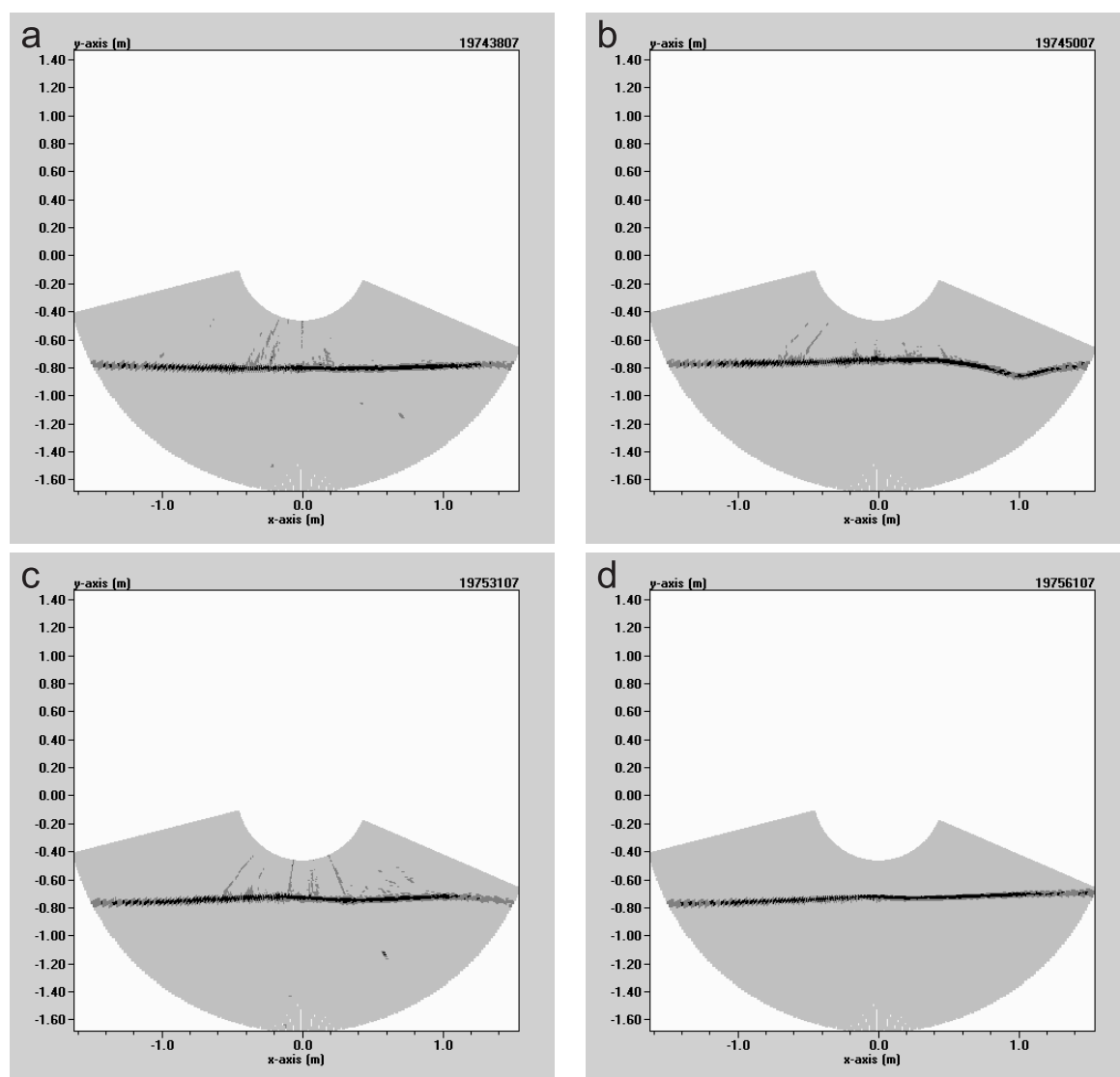**Figure A.4:** Sonar images from the ripple profiler, condition H12.

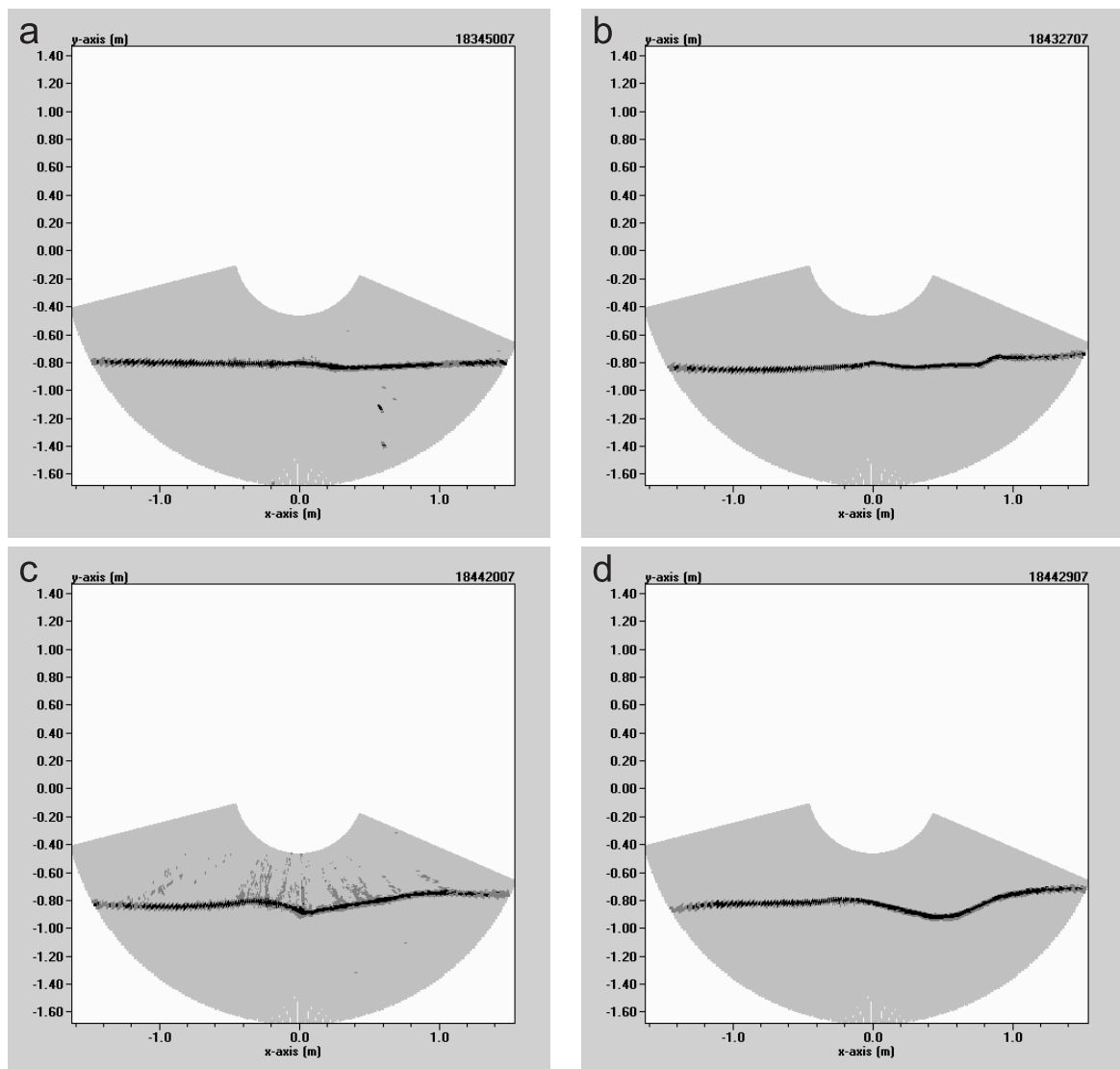**Figure A.5:** Sonar images from the ripple profiler, condition H15.

Figure A.6: Sonar images from the ripple profiler, condition H15 (calibration).

Appendix B

Applied statistics

To evaluate the model's performance, both for parameter optimization and validation, some statistical parameters have been selected. The same 5 parameters are used as proposed in Walstra et al. (2001). These parameters are selected from the statistical analysis tool from the Unibest testbank. In Table B.1 an overview is shown of the applied statistical parameters.

Table B.1: Overview of applied statistical parameters.

Quantity	Description	Statistical parameter
H_{rms}	wave height	RMAE or BSS
$u(z)$	vertical velocity profile	RMAE or RMSE
$c(z)$	vertical concentration profile	RMAE or RMSE
$q_{\text{tot}}(x)$	cross-shore total sediment transport	RBIAS, BIAS or BSS

A summary of these statistical parameters is given below.

BIAS

$$BIAS = \frac{1}{N} \sum_{i=1}^{N} (f_{\text{comp},i} - f_{\text{meas},i}) \tag{B.1}$$

Low values of the BIAS indicate good model performance. Positive values imply overprediction of the model, negative values underprediction of the model. The BIAS is an absolute statistical parameter, the resulting values should always be interpreted by taking the magnitude of the measurements and model results into account. The BIAS can be made relative by dividing by the sum of the measurements:

$$RBIAS = \frac{\sum_{i=1}^{N} (f_{\text{comp},i} - f_{\text{meas},i})}{\sum_{i=1}^{N} f_{\text{meas},i}} \tag{B.2}$$

RMSE

$$RMSE = \sqrt{\frac{1}{N} \sum_{i=1}^{N} (f_{\text{comp},i} - f_{\text{meas},i})^2} \tag{B.3}$$

Similar to the BIAS, low values indicate good model performance. The root-mean-square error (RMSE) is also an absolute statistical parameter. Since the errors are squared before they are averaged, the RMSE gives a relatively high weight to large errors. Because the relative RMSE is also sensitive for outliers, the relative mean absolute error is used, which is comparable to the relative RMSE.

$$RMAE = \frac{\frac{1}{N} \sum_{i=1}^{N} |f_{\text{comp},i} - f_{\text{meas},i}|}{\frac{1}{N} \sum_{i=1}^{N} |f_{\text{meas},i}|} \tag{B.4}$$

BSS   The Brier Skill Score (BSS) is defined in terms of mean-squared differences between measured values, modeled values and a set of baseline predictions, $f_{\mathrm{base},I}$. The baseline prediction is determined using the default settings for the free parameters as described in Walstra (2000). The default parameter settings are also shown in Table 4.4. A value of 1 indicates a perfect score, 0 implies no better score than the baseline prediction, and a negative score is a worse prediction than the baseline prediction.

$$BSS = 1 - \frac{\frac{1}{N}\sum_{i=1}^{N}\left(f_{\mathrm{comp},i} - f_{\mathrm{meas},i}\right)^2}{\frac{1}{N}\sum_{i=1}^{N}\left(f_{\mathrm{meas},i} - f_{\mathrm{base},i}\right)^2} = 1 - \frac{MS_{\mathrm{error}}}{MS_{\mathrm{baseerror}}} \tag{B.5}$$